

NONLINEAR INTERACTION OF STRUCTURED OPTICAL BEAMS

A DISSERTATION
SUBMITTED TO THE DEPARTMENT OF PHYSICS
AND THE DOCTORAL STUDIES COMMITTEE
OF INDIAN INSTITUTE OF TECHNOLOGY GANDHINAGAR
IN PARTIAL FULFILLMENT OF THE REQUIREMENTS
FOR THE DEGREE OF
DOCTOR OF PHILOSOPHY

Apurv Chaitanya N.
Roll number: 11330022
July 2016

© Copyright by Apurv Chaitanya N. 2016
All Rights Reserved

Declaration

I declare that this written submission represents my ideas in my own words and where others ideas or words have been included, I have adequately cited and referenced the original sources. I also declare that I have adhered to all principles of academic honesty and integrity and have not misrepresented or fabricated or falsified any idea/data/fact/source in my submission. I understand that any violation of the above can cause disciplinary action by the Institute and can also evoke penal action from the sources which have thus not been properly cited or from whom proper permission has not been taken when needed.

(Apurv Chaitanya N.) Author

Roll no: 11330022

Certificate

It is certified that the work contained in the thesis titled "Nonlinear Interaction of Structured Optical Beams" by Apurv Chaitanya N.(Roll no: 11330022), has been carried out under my supervision and that this work has not been submitted elsewhere for a degree.

I have read this dissertation and that, in my opinion, it is fully adequate in scope and quality as a dissertation for the degree of Doctor of Philosophy.

(Dr. Goutam Kumar Samanta) Principal Adviser

I certify that I have read this dissertation and that, in my opinion, it is fully adequate in scope and quality as a dissertation for the degree of Doctor of Philosophy.

(Prof. R. P. Singh) DSC Member 1

I certify that I have read this dissertation and that, in my opinion, it is fully adequate in scope and quality as a dissertation for the degree of Doctor of Philosophy.

(Dr. Partha Konar) DSC Member 2

Abstract

The general principles of Maxwell's electromagnetic theory and quantum mechanics were well established much before the invention of lasers. However, after the first report of laser in 1960 and subsequent advancement in the field of laser technology, these theories have been revisited to understand the effects of higher order interactions between intense laser light beams and matter in terms of nonlinear susceptibilities. As such, the study of behavior of light in nonlinear media, in which the dielectric polarization responds nonlinearly to the electric field of the light, has given birth to a new branch of optics called nonlinear optics. Typically nonlinear optical effects are studied using laser beams with Gaussian intensity distribution. However, in recent times, structured coherent optical beams including optical vortices, hollow Gaussian beam, and Airy beam have found wide range of applications in variety of fields in science and technology. All existing techniques used to date to generate such beams suffer from different limitations including lower output power and restricted wavelength range. On the other hand, interactions of such beams with nonlinear media are mostly unexplored.

During my PhD we have studied the nonlinear interaction of optical beams with different spatial structures. We have used second order nonlinear interactions such as second harmonic generation (SHG), where two photons from same laser get annihilated to produce a new photon of double energy, and sum frequency generation (SFG), where two photons of two different lasers get annihilated to produce a new photon of energy equal to the sum of the energies of the annihilated photons. The study also includes the nonlinear generation of structured beams such as Laguerre Gauss beams (optical vortices), a new class of vortex beam known as "perfect" vortex beams, hollow Gaussian beam, and Airy beam in different spectral and temporal domains.

Most of the lasers (but not all) produce electromagnetic radiation in Gaussian intensity profile. However, due to unavailability of suitable laser gain medium, the nonlinear optical effects play pivotal role in generating coherent optical radiation with wavelength inaccessible to lasers. Using an ultrafast femtosecond laser at 1064 nm we have studied the second order nonlinear interactions such as SHG and SFG in different nonlinear crystals to produce ultrafast coherent radiation at 532 nm and 355 nm in Gaussian intensity profiles. Such beams have variety of applications, including spectroscopy, material processing, pumping of optical parametric oscillators and generation of structured optical beams. The efficiency of nonlinear optical processes varies proportional to the square of the length of the nonlinear crystal and the intensity of the laser beam. However, use of longer crystal length and increase of laser intensity through tight focusing do not necessarily increase the overall efficiency of the nonlinear process. There is always an optimum focusing condition for efficient nonlinear interactions, [1] have predicted such optimum condition for SHG of continuous wave (cw) or long-pulse lasers. However, the optimum focusing condition in the presence of temporal walk-off arising from the use of ultrafast lasers can be different from that of the cw and long-pulse lasers [2, 3]. We have also investigated the optimum focusing condition for single-pass SHG and SFG of ultra-short femtosecond pulses for generating the optical beams at 532 and 355 nm in Gaussian intensity distribution respectively. We have also done a comparative SHG performance study of the crystals having different temporal and spatial walk-off parameters. We have further investigated the effect of the ratio of confocal parameters (beam focusing condition) and power ratio of the interacting pump beams in SFG process.

Knowing the effect of Gaussian beam in nonlinear frequency conversion processes, we have studied the interaction of orbital angular momentum (OAM) of the laser beams with nonlinear medium. Unlike Gaussian beams, optical vortex beams, spatially structured beams with helical wave-front [4], carry photons with OAM. These beams have doughnut shaped intensity profile with zero intensity at the point of phase singularity. Optical vortices are characterized by its topological charge (order), or winding number, l and are found to carry OAM of $l\hbar$ per photon. Using second order nonlinear crystals we have studied the frequency doubling characteristics of high-power, ultrafast, optical vortex beams by generating optical vortices of order up to 12 at 532 nm and 266 nm wavelengths. We have

experimentally verified the OAM conservation law, the OAM of the generated photon is equal to the sum of the OAMs of the annihilated photons, in SHG process. We have also demonstrated a new scheme to generate optical vortices of orders $l = 1$ to 6 by using only two spiral phase plates (linear optical elements to generate optical vortices of a fixed order) of phase winding 1 and 2. We further observed that the efficiency of vortex SHG process decreases with the order of the vortex. We attributed such effect to the increase of the area of vortex beam with its order. However, it was not possible to overrule the contribution (if any) of OAM in the SHG process as the area and order of the vortex are not mutually independent parameters.

The decrease of SHG efficiency of optical vortices with order restricts the study of nonlinear interaction of vortices to a certain order. Additionally, the dependence of beam area with its order does not provide clear information about the contribution of vortex order (OAM) in nonlinear frequency conversion process. However, a recent advancement in the field of structured beam has produced a new class of vortex beam, known as “perfect” vortex. These beams have area independent of the vortex order. Using such vortices we have experimentally verified that the vortex SHG efficiency does not depend upon the order (OAM) of the optical vortices. We have also studied the nonlinear frequency conversion of such beams to produce "perfect" vortex beam of order up to 12 with power as high as 1 W for all orders. We verified OAM conservation of "perfect" vortices in SHG process.

Due to the OAM conservation in SHG process, the OAM of the frequency doubled vortex beam is twice that the pump beam. But what will happen to the output beam if the interacting photons in the nonlinear process have opposite OAMs? To study such effect we have studied the SFG (SHG is the special case of SFG process) process of two pump beams having equal vortex orders but opposite in sign (direction of the helical phase variation). As expected, due to OAM conservation law the output beam was found to have no OAM ($l = 0$). However, the output beams have no light (dark) region at the center of the beam similar to the vortex beam. This is a new class of structured beam known as hollow Gaussian beam (HGB) [5] and our method gives a new way of generating HGB through nonlinear processes. The increase of annular ring radius of these beams with the order of the input vortex beams signifies that HGBs also have certain orders. However, there is no

experimental or theoretical means to determine the order of such beams. We have devised a new way to determine the order of hollow Gaussian beams.

To broaden our study and to address other structured beams we have generated Airy beam and characterized its properties. Unlike other structured beams, Airy beam has peculiar properties such as beam shape invariance with propagation (non-divergence), propagation along curved trajectory in free space (self-acceleration), and self-restoration (self-healing) of beam shape even after obstruction by small objects. Using intracavity cubic phase modulation of an ultrafast singly resonant optical parametric oscillator (SRO), we have generated ultrafast beam in 2- D Airy intensity distribution with wavelength tunability across the near-IR wavelength range. In addition to the Airy beam, the SRO produces Gaussian output beam in the near- to mid-IR wavelength range across 1.4 - 1.7 μm with power as much as 1.54 W.

Publications

Journal publications

Publications included in the thesis

1. *Type-I frequency-doubling characteristics of high-power, ultrafast fiber laser in thick BIBO crystal,*
Apurv Chaitanya N., A. Aadhi, R. P. Singh, and G. K. Samanta,
Optics Letters 39, 5419 (2014).
2. *High-power, high-repetition-rate, Yb-fiber laser based femtosecond source at 355 nm,*
Apurv Chaitanya N., A. Aadhi, M. V. Jabir, and G. K. Samanta,
Optics Letters 40, 4269 (2015).
3. *Frequency-doubling characteristics of high-power, ultrafast vortex beams,*
Apurv Chaitanya N., A. Aadhi, M. V. Jabir, and G. K. Samanta,
Optics Letters 40, 2614 (2015).
4. *Efficient nonlinear generation of high power, higher order, ultrafast “perfect” vortices in green,*
Apurv Chaitanya N., M. V. Jabir, and G. K. Samanta,
Optics Letters 41, 1348 (2016).
5. *Ultrafast optical vortex beam generation in the ultraviolet,*
Apurv Chaitanya N., S. Chaitanya Kumar, K. Devi, and G. K. Samanta, M.

- Ebrahim-Zadeh,
Optics Letters 41, 2715 (2016).
6. *Ultrafast Airy beam optical parametric oscillator*,
Apurv Chaitanya N., S. Chaitanya Kumar, A. Aadhi, G. K. Samanta, and M. Ebrahim-Zadeh
Scientific Reports 6, 30701 (2016).
7. *Hollow Gaussian beam generation through nonlinear interaction of photons with orbital-angular-momentum*,
Apurv Chaitanya N., M. V. Jabir, J. Banerji, and G. K. Samanta,
Scientific Reports (Under Revision).

Publications not included in the thesis

1. *High-power, continuous-wave, solid-state, single frequency, tunable source for the ultraviolet*,
A. Aadhi, **Apurv Chaitanya N.**, R. P. Singh, and G. K. Samanta,
Optics Letters 39, 3410 (2014).
2. *All-periodically poled, high-power, continuous-wave, single-frequency tunable UV source*,
A. Aadhi, **Apurv Chaitanya N.**, R. P. Singh, and G. K. Samanta,
Optics Letters 40, 33 (2015).
3. *Generation of “perfect” vortex of variable size and its effect in angular spectrum of the down-converted photons*,
M. V. Jabir, **Apurv Chaitanya N.**, A. Aadhi, and G. K. Samanta,
Scientific Reports, 6, 2187 (2016).
4. *Airy beam optical parametric oscillator*,
A. Aadhi, **Apurv Chaitanya N.**, M.V. Jabir, P. Vaity, R. P. Singh, and G. K. Samanta,
Scientific Reports, 6, 25245 (2016).

Selected Conference papers:

1. *High-power, cw, Airy beam optical parametric oscillator,*
A. Aadhi, Pravin Vaity, **Apurv Chaitanya N.**, M. V. Jabir, R. P. Singh, and G. K. Samanta,
CLEO: 2015 Postdeadline Paper Digest, (Optical Society of America, 2015), paper JTh5A.6.
2. *All Periodically-poled Crystals Based Source of Tunable, Continuous-wave, Single-frequency, Ultraviolet Radiation,*
A. Aadhi, **Apurv Chaitanya N.**, R. P. Singh, and G. K. Samanta,
CLEO: 2015, OSA Technical Digest (online) (Optical Society of America, 2015), paper JTU5A.26.
3. *Single-frequency continuous-wave tunable ultraviolet sources based on BIBO and PPKTP crystals and their comparative studies,*
A. Aadhi, **Apurv Chaitanya N.**, M. V. Jabir, R. P. Singh, and G. K. Samanta,
Proc. SPIE 9654, International Conference on Optics and Photonics 2015, 96541G (June 15, 2015).
4. *Optimization of frequency-doubling of high power, high repetition rate, femtosecond fiber laser in thick nonlinear crystal,*
Apurv Chaitanya N., A. Aadhi, M. V. Jabir, Vinayak Kumar, R. P. Singh, G. K. Samanta
12th International Conference on Fiber Optics and Photonics, OSA Technical Digest (online) (Optical Society of America, 2014), paper M4A.28.
5. *Continuous- wave, high Power, single-frequency, tunable ultraviolet source based on all periodically poled crystals,*
A. Aadhi, **Apurv Chaitanya N.**, R. P. Singh, G. K. Samanta
12th International Conference on Fiber Optics and Photonics, OSA Technical Digest (online) (Optical Society of America, 2014), paper M3A.4.

6. *Fiber Laser Based High Power, Ultrafast Source for 355 nm*,
Apurv Chaitanya N., A. Aadhi, M. V. Jabir, and G. K. Samanta
Advanced Solid State Lasers, OSA Technical Digest (online) (Optical Society of America, 2015), paper AM5A.49.
7. *Generation and Characterization of High Power and Higher Order Ultrafast Optical Vortices*,
Apurv Chaitanya N., A. Aadhi, M. V. Jabir, M. R. Pathak, N. U. Shaikh
Advanced Solid State Lasers, OSA Technical Digest (online) (Optical Society of America, 2015), paper AM5A.48.
8. *High-Power, Continuous-wave, Source Of Coherent Radiation In 2-D Airy Intensity Distribution*,
A. Aadhi, Apurv Chaitanya N., M V. Jabir, P. Vaity, R. P. Singh, and G. Samanta
Frontiers in Optics 2015, OSA Technical Digest (online) (Optical Society of America, 2015), paper LTh1H.3.
9. *Optical Vortex Beam Generation in the Deep-Ultraviolet*,
Apurv Chaitanya N., S. Chaitanya Kumar, G. K. Samanta and M. Ebrahim-Zadeh
CLEO: 2016, OSA Technical Digest (online) (Optical Society of America, 2015), paper JW2A.71.

Acknowledgement

It's been 4 years since I joined PRL. But I realized it only now because my work and stay at the PRL was full of happy moments with my friend, family, Professors and staffs of the PRL. My days here were some of the most memorable ones. There are many persons that have contributed to the realisation of my thesis, and I am very grateful to all those who contributed.

First of all, I express my deep gratitude to my supervisor Dr. G. K. Samanta, whose guidance and teaching was crucial for my research. His patience and in depth knowledge helped me and inspired me beyond I can express. His supportive nature is second to nothing. Be it academic or non-academic purpose, he was there to support me. My gratitude towards him knows no limits. Prof. J. Banerji and Prof. R. P. Singh from optics group were always approachable for any sorts of problems. I take this opportunity to acknowledge their support and motivating words which has immensely influenced me. Constructive criticism and guidance from my doctoral committee members Prof. R. P. Singh, Dr. Partha Konar and Dr. Jithesh Bhatt was very much instrumental in making this work possible, I reserve my gratitude for them. I also wish to convey my sincere regards to Dr Navinder Singh and Dr Ramitendranath Bhattacharyya for their guidance, continuous support, suggestions and help throughout my first and second semester projects.

I would like to extend my sincere gratitude to Prof. Utpal Sarkar, Director PRL for supporting all the outreach activities and for being generous in providing opportunities for arranging students conference which has definitely helped me in increasing my confidence in interacting with people from different spheres of life and to muster managerial skills.

I would also like to take this opportunity to thank Academic services, Administrative services, workshop, computer center and all the other members of PRL family for all the help, love and care they have given to me and made my four years feel short in PRL.

A world without friends is a world without colors. My best friends in PRL, namely Ashimananda Modak, Bivin Geo George, and Lalit Shukla were with me throughout for any help. They gave me some of the most memorable moments in my life. Hot discussions in optics and politics with Dr. Sashi Prabhakar, Dr. S. G. Reddy and Mr. Chithrabhanu P., whom I shared office space, kept me posted on developments around the world and kept me out of boredom in my off time. I am really thankful to them. In my initial days with my group my lab-mate Dr. A. Aadhi walked me around the lab, familiarized me with the equipments and saved me from the burden of starting from the scratch. I would like to thank him for everything he has done for me. Jabir M. V., my junior has been very friendly. We shared lab space, played football and badminton together, went for eating non veg, bought new gadgets together. Going for conferences, like the one in Darjeeling, was always fun with him. Weekends with colleagues in hostel were also the most enjoyable time of the non-academic part of my life at PRL. They will be always be in my heart.

At ICFO, the one man who inspired me to do things differently and efficiently was Dr. S. Chaitanya Kumar. Working with him made me forget everything and to focus on once work. He taught me a lot of things through his actions. I am really thankful to him for that. I would also like to thank Prof. Dr. Majid Ebrahim-Zadeh for inviting me to his lab and giving me the opportunity to spend almost 2 months there.

Dr. Ganesh Sundaram, who has been my professor at Amrita Vishwa Vidyapeetham has been my real inspiration to pursue my higher studies after graduation. The numerous hours he spent for me cannot be repaid by anything. I am greatly indebted to him for everything he has done for me. Dr. Rajmohan Kombiyil the then HOD of Physics department always set us very high goals, which made us dream high. Even after my college days, through mails and talks he always used to motivate me and blessed me with his presence in my marriage. I am always indebted to him for his kind gestures. Not only him, but Dr. Krishnakumar V., Dr. Rajan Sundaravaradan, Dr. Sreelatha K. and Dr. Sreeja V. K. have been supportive and caring. I would like to thank all of them who influenced my life tremendously.

My college mates Krishnakumar and Rajesh has been there with me for everything during and after my college days at Amrita Vishwa Vidyapeetham. Varun Jaiswal, Abhijeet Mishra, Jijo Mohan and Abhijeet Singh, from NDA, was really supportive and caring. Dr. Usha, Mrs. Sujatha and Mrs. Suja from ARR Public School and Mrs. Chitra and Mrs. Vijayalekshmi from Bharatiya Vidya Bhavan, was really caring and supportive of my work and tolerant towards my mischiefs. They always encouraged me to be myself. I would like to thank them all for their extensive care and help for me.

None of this would have been possible without the help and support from my mother, father, brother and wife. Their unconditional love and support made me totally free of all responsibilities. I am greatly thankful towards them for letting me pursue my dreams and relieving me of my duties as a family man and taking care of my daughter in my absence without any conditions. No words can describe how much I'm thankful to them. I would like to thank my daughter for making me smile every time I call her over phone, no matter how much sad I am.

Preface

The thesis will be divided into 7 chapters. In Chapter 1 we will be revisiting the basics of nonlinear optics which were extensively used throughout my Ph. D. work. Most of the results involve second order nonlinear processes like second harmonic generation and sum frequency generation. Hence the first chapter covers mostly the basics of second order nonlinear processes. We will also include a brief introduction to the structured beams in this chapter.

Temporal and spatial walk-off parameters of nonlinear crystals have detrimental effects in overall efficiency of nonlinear wave mixing of short pulse lasers in thick nonlinear crystals. Therefore, optimum beam focusing condition is crucial for maximum nonlinear gain and conversion efficiency for each crystal length. Moreover, the correct selection of nonlinear crystal with minimal spatial and temporal walk-off parameters, high nonlinear gain, and elevated damage threshold is required for the success of such projects. Therefore, a comparative study of all available crystals for generating ultrafast green beam will be addressed in the first section of Chapter 2. In case of UV generation using SFG process, the crystals transparency window and phase match-ability at the required wavelength are the most important parameters to consider for the selection of proper crystal. In SFG process, two photons from two different pump lasers annihilate to generate a high energy photon through the energy conservation law. Therefore, efficiency of the SFG process depends on the power ratio of the interacting lasers and the ratio of their confocal parameters. Experimental finding of such parameters and their effect in the SFG process will be discussed in later part of Chapter 2.

Chapter 3 will address the nonlinear interaction of photons with orbital angular momentum. In this chapter we will discuss about the experimental results on nonlinear generation

of vortex beams at 532 nm and 266 nm. Like Gaussian beams, vortex beams also have focusing dependent conversion efficiency. At the same time, the conversion efficiency of vortices vary with the order of pump vortices. The experimental results and theoretical prediction on the decrease of vortex SHG efficiency with order and all other important results including angular acceptance bandwidth, temporal and spectral width with order of the input vortex beam will be discussed at length.

As the size of the vortex beam increases with order or OAM it is difficult to ascertain the contribution of OAM in the wave mixing processes. Therefore, to find the exact contribution of OAM and size of vortex beam in the efficiency of the nonlinear frequency conversion processes we have studied the SHG of a new class of vortex beam known as "perfect" vortex (whose beam size is independent to its order) and experimentally observed that the OAM of the vortex beam does not influence the efficiency of the nonlinear processes. The decrease of nonlinear gain with the order of the vortices is solely influenced by the variation in size of the vortices with its order. All these findings will be presented in Chapter 4 along with the results on nonlinear generation of "perfect" vortex in green.

According to OAM conservation in the SFG process, the OAM of the generated photon should be equal to the sum of the OAM of the interacting photons. We have experimentally observed OAM conservation in SHG, a special case of SFG process, that will be presented in Chapter 3 and Chapter 4. But what will happen if the interacting pump photons in SFG process have OAMs of equal magnitude but opposite in sign? Solving the coupled wave equations for such process, it can be shown that the output electric field have the form of a hollow Gaussian beam with zero OAM. Chapter 5 will carry the description of this processes and related experimental results on nonlinear interaction of oppositely charged equal order vortex beams generating hollow Gaussian beam. In this chapter we will also present a novel technique to determine the order of hollow Gaussian beams.

In Chapter 6 we will address a special kind of beam known as Airy beam. Unlike other structured beams, Airy beams have peculiar properties such as non-diffraction, self-acceleration and self-healing. We have experimentally demonstrated a new scheme to generate ultrafast structured optical beam in 2 D Airy intensity profile from an optical parametric oscillator (OPO). Using intra-cavity cubic phase modulation of the resonating beam of an OPO and subsequent Fourier transformation we have generated wavelength tunable

Airy beam. Investigation on different characteristics of the Airy beam will be presented in Chapter 6.

Finally, Chapter 7 will conclude my thesis work along with future outlook.

Contents

Abstract	vii
Publications	xi
Acknowledgement	xv
Preface	xix
1 Introduction to nonlinear optics and structured beams	1
1.1 Nonlinear optics	2
1.1.1 Second order nonlinear effects	3
1.1.2 Energy and momentum conservation	9
1.2 Structured beams	10
1.2.1 Gaussian beam	11
1.2.2 Vortex beam	11
1.2.3 Hollow Gaussian beam	12
1.2.4 "Perfect" vortex beam	13
1.2.5 Airy beam	13
2 Nonlinear interaction of coherent radiation in Gaussian	15
2.1 Frequency-doubling of femtosecond pulses in "thick" nonlinear crystals with different temporal and spatial walk-off parameters	16
2.1.1 Introduction	16
2.1.2 Experiment	18

2.1.3	Results and discussion	19
2.2	High-power, high-repetition-rate, Yb-fiber laser based femtosecond source at 355 nm	34
2.2.1	Introduction	34
2.2.2	Experiment	35
2.2.3	Results and discussion	37
3	Nonlinear interaction of high power ultrafast vortex beams	45
3.1	Frequency-doubling characteristics of high-power, ultrafast vortex beams at 532 nm	45
3.1.1	Introduction	45
3.1.2	Experiment	47
3.1.3	Results and discussion	48
3.2	Generation of optical vortices at 266 nm	56
3.2.1	Introduction	56
3.2.2	Experiment	57
3.2.3	Results and discussion	58
4	Nonlinear generation of high power ‘perfect’ vortex beam	67
4.1	Efficient nonlinear generation of high power, higher order, ultrafast “per- fect” vortices in green	67
4.1.1	Introduction	67
4.1.2	Experiment	69
4.1.3	Results and discussion	70
5	Hollow Gaussian beam generation through nonlinear interaction of photons with orbital-angular-momentum	79
5.1	Nonlinear generation of hollow Gaussian beam	79
5.2	Methods	87
6	Generation of ultrafast tunable Airy beam	89
6.1	Ultrafast Airy beam optical parametric oscillator	89

6.1.1	Introduction	89
6.1.2	Theory	90
6.1.3	Experiment	91
6.1.4	Results and discussion	92
7	Conclusion and scope for future work	101
7.1	Conclusion	101
7.2	Scope for future work	103
	Bibliography	105

Chapter 1

Introduction to nonlinear optics and structured beams

In this work we have extended the application of higher order light matter interaction (non-linear optics) into a relatively unexplored field- ‘generation of coherent structured beams’. We have generated optical beams in various spatial profiles including Gaussian beam, Laguerre Gauss beams, "perfect" vortex beams, Airy beam and hollow Gaussian beam in demanding spectral and temporal domain which otherwise cannot be accessed through the principles of linear optics. The efficient generation of such beams is highly demanding in terms of the experimental difficulties. The inherent low parametric gain of non-Gaussian beam for nonlinear optical processes is the fundamental stumbling block which one needs to address with keen details. Hence correct choice of nonlinear medium and pump beam parameters are crucial for the success of such projects apart from the optimum design of the experimental set up. The theoretical understanding of the beam dynamics of these special beams also was a prerequisite for predicting the behavior of the interaction as well as understanding the beam propagation inside the medium and in free space. A lot of emphasis was imparted not only in carrying out the experiments but there after for processing the data for interpreting the results, hence understanding basic data manipulation and image processing was also of great use throughout the projects. In this chapter the basics of nonlinear optics is discussed and the later sections carry description of different kinds of structured beam on which the thesis is based upon.

1.1 Nonlinear optics

Right after the invention in 1960, the laser was described as the remarkable tool in search of an application. However, nonlinear optics is the immediate application for the lasers. With the invention of lasers, nonlinear optics has been a rapidly growing field in recent decades. It is based on the study that deals mainly with various new optical effects and novel phenomena arising from the interactions of intense coherent optical radiation with matter. With the invention of laser it was possible to have high intensity of monochromatic coherent source. Such high intensities (electric field) while interacting with some of the dielectric optical mediums produce higher order nonlinear optical effects. In general, the coefficients of such higher order effects are very small. As a result, such effects are not visible in our daily life.

Starting from Ohm's Law, which relates applied electric field, \mathbf{E} to the current density \mathbf{J} , considered only first order responses as

$$\mathbf{J} = \sigma \mathbf{E}$$

where σ is the conductivity. In the presence of high electric field, higher order terms start gaining significance,

$$\mathbf{J} = \sigma^{(1)} \mathbf{E}^1 + \sigma^{(2)} \mathbf{E}^2 + \sigma^{(3)} \mathbf{E}^3 + \dots$$

These higher order terms result in new phenomena which were not observed before the invention of laser. In 1961, Franken [6] observed that a Ruby laser at 694 nm while passed through a quartz crystal, produces a faint spot at 347 nm. The generation of new wavelength at 374 nm was possible due to the second harmonic generation (SHG) of the Ruby laser in quartz crystal. This effect is considered as the beginning of nonlinear optics. Even after 50 years of first observed nonlinear effect, the field is still open for new developments to come.

To understand the origin of nonlinear effects, let us consider a simple atom where the electron is revolving around the heavy nucleus in a circular orbit. In absence of any external field, the electron will continue its motion in the circular path without any net dipole moment and hence polarization. However, if an electric field (like the electromagnetic field)

is applied to the atom, the field will drive the electron away from the nucleus resulting in a net dipole moment and polarization. If the driving electric field is oscillatory in nature, the atomic dipole will oscillate with the electric field and emit radiation. For lower electric field strength, the dipole oscillation will be harmonic and the emitted radiation will have same frequency as that of the driving field. The linear polarization (dipole moment per unit volume) can be written as [7],

$$\mathbf{P} = \epsilon_0 \chi_e \mathbf{E}$$

where \mathbf{E} is the applied electric field, χ_e is the electrical susceptibility of the material and ϵ_0 is the vacuum permittivity. \mathbf{P} is the dipole moment per unit volume (polarization), and \mathbf{E} is the electric field. Examples of such linear optical effects include reflection, refraction, transmission etc.

However, at higher electric field strength, the dipole oscillation will no longer be harmonic. The unharmonic oscillation of the oscillating dipole is the origin of nonlinear optical effects. The nonlinear polarization can be represented as [8],

$$\mathbf{P} = \epsilon_0 \left[\chi_e^{(1)} \mathbf{E}^1 + \chi_e^{(2)} \mathbf{E}^2 + \chi_e^{(3)} \mathbf{E}^3 \dots \right] \quad (1.1.1)$$

where, $\chi_e^{(2)}$ and $\chi_e^{(3)}$ are second order and third order nonlinear coefficients respectively, here for simplicity we have considered an isotropic medium, in general $\chi_e^{(n)}$ will be an $(n+1)^{th}$ ranked tensor. Typically, the values of $\chi_e^{(1)}$, $\chi_e^{(2)}$ and $\chi_e^{(3)}$ are of the order of 10^{-4} [7], 10^{-12} , 10^{-24} [8] respectively. As a result, the higher order terms become significant with higher values of the applied \mathbf{E} . Since the electric field strength of the lights in our daily life is small, we do not observe any higher order nonlinear optical effects. Given the high electric field strength of the laser beams, nonlinear optical effects were only observed after the invention of laser.

1.1.1 Second order nonlinear effects

The coefficient of the second term in Eq. (1.1.1) is known as the second order nonlinear coefficient. This coefficient results in many second order nonlinear optical effects including SHG, sum frequency generation (SFG), difference frequency generation, optical parametric

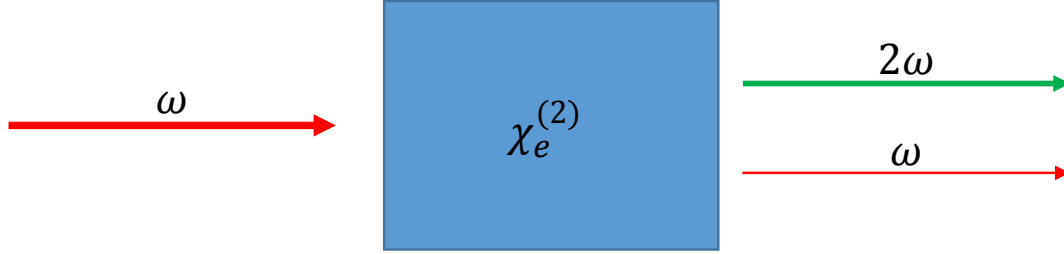


Figure 1.1.1: Block diagram of SHG

generation. My research is related to these second order nonlinear processes. Therefore, I will explain briefly on some of the second order nonlinear processes which I have come across during my PhD.

Second harmonic generation (SHG)

For considerable high value of E , P also have contribution from second order term of Eq. (1.1.1). Suppose we are applying a time varying electric field of the form $\mathbf{E} = \mathbf{E}_0 (e^{-i\omega t} + e^{+i\omega t})$. Using this in Eq. (1.1.1) it is straight forward to show that

$$\mathbf{P} = \epsilon_0 \left[\chi_e^{(1)} \mathbf{E}_0 (e^{-i\omega t} + e^{+i\omega t}) \right] + \epsilon_0 \left[\chi_e^{(2)} \mathbf{E}_0^2 (2 + e^{-i2\omega t} + e^{+i2\omega t}) \right] + \dots \quad (1.1.2)$$

The second term is called the second order nonlinear polarization [8]. ‘Nonlinear’ because it’s response is quadratic rather than linear to the applied electric field. Although our incident EM wave is time varying with a single frequency ω (though frequency, $\nu = \omega/2\pi$ through out the this chapter we refer ω as the frequency), the second term in Eq. (1.1.2) shows that \mathbf{P} has 2ω term too and shown in Fig. (1.1.1). This physically means that in the localized atoms, the charge cloud is oscillating with respect to its equilibrium position with a frequency of 2ω also. Even though the applied electric field has only one frequency, the charged cloud will oscillate with frequency 2ω along with ω . As a result of this, the oscillating charges emit EM waves which have frequencies ω and 2ω both. This process of emission of frequency doubled EM waves are called SHG. The energy level diagram for the SHG process is shown in Fig. (1.1.2) where two photons of frequency ω are absorbed

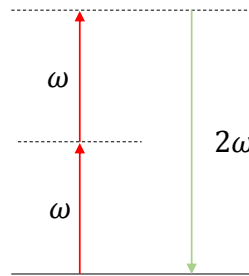


Figure 1.1.2: Energy level description of SHG

and generates a photon with energy of 2ω . This energy diagram is shown just to understand SHG from the perspective of lasers. However, it is to be noted that the nonlinear optical processes are parametric in nature. No actual energy levels of the materials are involved in such processes.

Sum frequency generation (SFG)

Suppose, we have two time varying electric fields with two different frequencies

$$\mathbf{E}_1 = \mathbf{E}_n (e^{-i\omega_n t} + e^{i\omega_n t})$$

and

$$\mathbf{E}_2 = \mathbf{E}_m (e^{-i\omega_m t} + e^{i\omega_m t}).$$

The total electric field is given by

$$\mathbf{E} = \mathbf{E}_n (e^{-i\omega_n t} + e^{i\omega_n t}) + \mathbf{E}_m (e^{-i\omega_m t} + e^{i\omega_m t}).$$

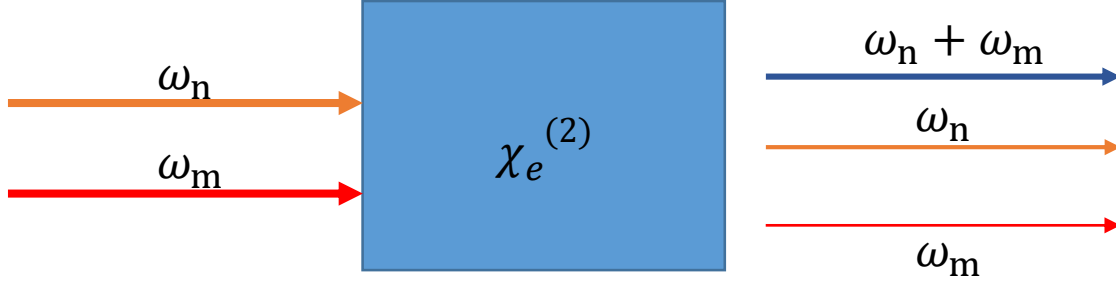


Figure 1.1.3: Block diagram of SFG

If a nonlinear material is exposed to this field with sufficiently high intensity, Eq. (1.1.2) can be written as

$$\mathbf{P} = \epsilon_0 \chi_e^{(1)} \mathbf{E} + 2\epsilon_0 \chi_e^{(2)} [\mathbf{E}_n^2 + \mathbf{E}_m^2] + \epsilon_0 \chi_e^{(2)} \left[\mathbf{E}_n^2 e^{-i2\omega_n t} + \mathbf{E}_m^2 e^{-i2\omega_m t} + 2\mathbf{E}_n \mathbf{E}_m e^{-i(\omega_n + \omega_m)t} + 2\mathbf{E}_n \mathbf{E}_m e^{-i(\omega_n - \omega_m)t} + c.c. \right]. \quad (1.1.3)$$

The term $2\epsilon_0 \chi_e^{(2)} \mathbf{E}_n \mathbf{E}_m e^{-i(\omega_n + \omega_m)t}$ in the above equation corresponds to the emission of the EM wave whose frequency is given by the sum of the individual frequencies. This process is known as SFG. The schematic diagram of such a process is shown in Fig. (1.1.3). Here, two photons of frequency ω_n and ω_m annihilate and one photon of frequency $\omega_m + \omega_n$ is formed

The energy level representation can be visualized as in Fig. (1.1.4).

Difference frequency generation (DFG)

In Eq. (1.1.3), there are terms with frequency $\omega_n - \omega_m$ along with other terms. Due to this, the charge cloud will emit the EM waves with frequency $\omega_n - \omega_m$. So through the second order nonlinear process, it is also possible to generate the difference of incoming frequencies (Fig. (1.1.5)), depending on the phase matching condition. The energy level description for difference frequency generation process is shown in Fig. 1.1.6

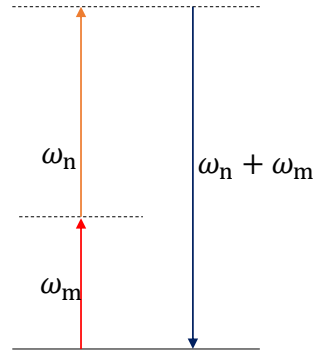


Figure 1.1.4: Energy level description of SFG

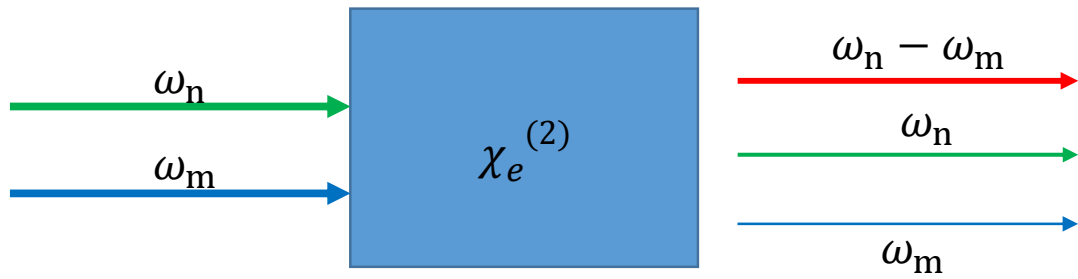


Figure 1.1.5: Block diagram of difference frequency generation

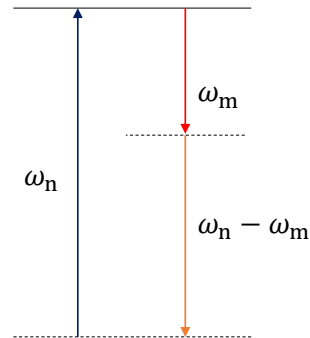


Figure 1.1.6: Energy level description of difference frequency generation

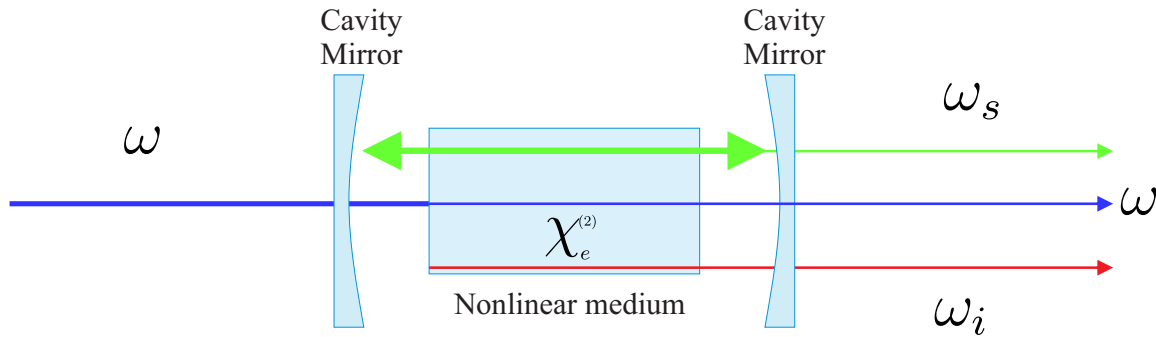


Figure 1.1.7: Schematic diagram of the optical parametric oscillator

The Eq. 1.1.2 is a special case of Eq. 1.1.3 with the condition $\omega_n = \omega_m$. So, SHG is a special case of the more general SFG process where both the incoming frequencies are same.

Optical parametric generation

Optical parametric generation (OPG) is also a second order nonlinear optical process where a pump photon of frequency ω while interacting with a non-centrosymmetric (whose second order nonlinear coefficient is nonzero) crystal splits into two photons of different frequencies ω_i and ω_s , namely idler and signal respectively. This process is the reverse process of the difference frequency generation. However, the gain of such process is very low. To increase the gain, typically, the OPG crystal is placed inside an optical cavity. Such device is known as optical parametric oscillator (OPO).

Optical parametric oscillator

Since the development of the first laser, nonlinear optics has evolved as a powerful technique to generate tunable optical radiation inaccessible by the ordinary lasers. Based on second order nonlinear effect, the optical parametric oscillators (OPOs) have become a standard device to convert a fixed laser wavelength to wide band of coherent radiations ranging from visible to far-IR. The schematic of the OPOs are shown in Fig. 1.1.7.

Like lasers, OPOs also consist of a strong pump, second order nonlinear crystal and a resonator. A strong pump photon while interacting with the nonlinear crystal splits into

two daughter photons commonly known as signal and idler. Since the nonlinear gain is very small, an optical cavity is used to give positive feedback to the generated photons and amplify in the presence of pump. Depending on the number of waves resonating inside the cavity, the OPOs are termed as singly-resonant OPO (SRO) where one of the generated waves, doubly-resonant OPO (DRO) where both the generated waves are resonant, triply-resonant OPO (TRO) where all three waves are resonant. The threshold of the OPOs reduce with the increase in the number of resonating waves, however, with increasing difficulties. The simplest OPOs are SROs. However, its threshold is very high as compared to other configurations.

1.1.2 Energy and momentum conservation

All the processes mentioned in previous sections should maintain two conservation laws; energy and momentum conservation. Typically in the field of optics, the momentum conservation is known as phase-matching. To illustrate energy conservation and momentum conservation let us consider the SFG process. In SFG, two photons of different frequencies ω_1 and ω_2 annihilate to generate a photon of frequency ω_3 . Here, the initial energy of the two photons $\hbar\omega_1 + \hbar\omega_2$ has to be equal to the final energy of the photon $\hbar\omega_3$. This leads to a condition

$$\omega_1 + \omega_2 = \omega_3 \quad (1.1.4)$$

Similarly, from the momentum ($\hbar k$) conservation, one can obtain

$$k_1 + k_2 = k_3. \quad (1.1.5)$$

This is known as phase matching condition which needs to be achieved in order to maximize the output intensity in any nonlinear optical process [8]. Now, for phase matching condition Δk should be zero which leads to

$$n_1 \omega_1 + n_2 \omega_2 = n_3 \omega_3.$$

where the relation $k_i = n_i \omega_i$ is used, here n_i and ω_i are respectively the refractive index and the angular frequency of the i^{th} wave.

$$\omega_1 = \frac{n_3 \omega_3 - n_2 \omega_2}{n_1}. \quad (1.1.6)$$

Substituting Eq. (1.1.6) in Eq. (1.1.4) we obtain

$$(n_3 - n_1) \omega_3 = (n_2 - n_1) \omega_2. \quad (1.1.7)$$

From the normal dispersion of the materials, it is known that the materials have higher refractive index at higher frequency i.e., $n_3 > n_2 > n_1$ for $\omega_3 > \omega_2 > \omega_1$. So it is not possible to achieve the condition of Eq. (1.1.7) in normal crystals. Therefore, one need additional handle to satisfy this condition. Birefringent phase matching and quasi phase matching are the two popular techniques to satisfy this phase matching requirements. In either of them we manipulate the refractive index of the interacting beams such that the refractive index satisfies the required relations for phase matching. In birefringent phase matching the wave is oriented such that the required ray is either made an *e-ray* or an *o-ray* depending on the type of phase matching we are trying to obtain. In quasi phase matching periodically domain reversal of the crystal results in partial fulfillment of this refractive index condition, hence the name 'quasi'.

1.2 Structured beams

Conventional laser sources emit in the fundamental mode which is the Gaussian mode. Through phase modulation of these fundamental mode of the laser beam it is possible to create transverse spatial structure which can be achieved by different phase modulation techniques. It is also possible to control the phase of a generated beam through nonlinear interaction which will be elaborately discussed in the upcoming section. Before going to that it is worth while to discuss the different spatial structures which are covered in this thesis.

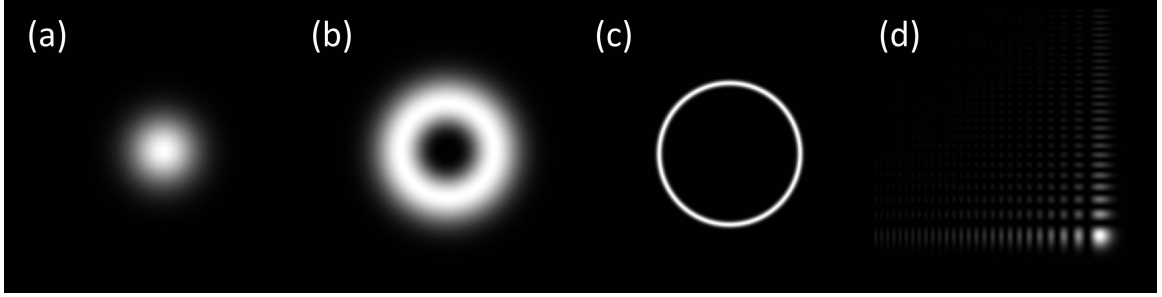


Figure 1.2.1: Transverse intensity distribution of different beams. (a) Gaussian, (b) vortex, (c) perfect vortex and (d) Airy beam.

1.2.1 Gaussian beam

Gaussian beams have intensity distribution which can be expressed in terms of a Gaussian function. For a Gaussian beam the majority of the intensity is in the center and decreases exponentially away from the center (see Fig. 1.2.1 (a) and 1.2.2 (a)). The intensity distribution of such beams can be described in terms of rectangular symmetric Hermite- Gaussian modes of amplitude given by [9]

$$\begin{aligned}
 u_{nm}^{HG}(x, y, z) = & \left(\frac{2}{\pi n! m!} \right)^{1/2} 2^{-N/2} (1/w) \exp \left[-ik(x^2 + y^2) / 2R \right] \\
 & \times \exp \left[- (x^2 + y^2) / w^2 \right] \exp \left[-i(n + m + 1) \psi \right] \\
 & \times H_n \left(x\sqrt{2}/w \right) \times H_m \left(y\sqrt{2}/w \right)
 \end{aligned}$$

where $H_n(x)$ is the Hermite polynomial of order n . The Gaussian mode is given by $m = n = 0$. This is the fundamental TEM_{00} transverse mode which most of the lasers intend to produce due to its high gain inside a cavity and is the lowest order solution of the paraxial wave equation.

1.2.2 Vortex beam

Optical vortex beams are spatially structured beams with a helical wave front. They have azimuthally varying phase distribution and has a phase singularity at the center of the beam. They have a doughnut shaped intensity profile with zero intensity at the singular point illustrated in Fig. 1.2.1 (b) and 1.2.2 (b). These beams are characterized by its topological

charge (order), or winding number, and is found to carry orbital angular momentum (OAM) of $l\hbar$ per photon [4]. Due to doughnut spatial structure and also the association of OAM, the optical vortices find variety of scientific, industrial, and medical applications [10, 11]. Such vortex beams is a special case of the Laguerre- Gaussian (LG) mode. The Laguerre-Gaussian modes can be represented as

$$\begin{aligned} u_{nm}^{LG}(r, \phi, z) = & \left(\frac{2}{\pi n! m!}\right)^{1/2} \min(n, m)! (1/w) \exp[-ik(r^2)/2R] \\ & \times \exp[-(r^2)/w^2] \exp[-i(n+m+1)\psi] \\ & \times \exp[-il\phi] (-1)^{\min(n, m)} L_{\min(n, m)}^{n-m} (2r^2/w^2)^{\min(n, m)} \end{aligned}$$

here $L_p^l(x)$ is a generalized Laguerre polynomial with radial index p and azimuthal index l . Vortex beam of order l can be represented as LG modes with zero radial index ($p = 0$) and azimuthal index l . The OAM unlike the spin angular momentum arises due to the azimuthal component of the pointing vector which can be attributed to the the helical wave front of such beams. These beams can be generated from Hermite Gaussian modes using astigmatic mode converters and using spiral phase plates (SPPs). They can also be generated through spatial light modulators (SLMs) using Holographic technique.

1.2.3 Hollow Gaussian beam

Hollow Gaussian beams are dark hollow beams (doughnut shaped intensity profile) with intensity profile same as that of the optical vortex beam apart from the azimuthally varying phase term. Hence they can, in principle, be generated by removing the azimuthal phase term from the normal vortex beam. The electric field of such a dark hollow beam can be represented as [5]

$$u_n(r, z = 0) = U_0 \left(\frac{r^2}{w_0^2}\right)^n \exp\left(-\frac{r^2}{w_0^2}\right).$$

When $n = 0$ the above equation reduces to Gaussian beam. Hollow Gaussian beam is not a solution of paraxial wave equation. Hollow Gaussian beam have found applications in optical cloaking, trapping, lithography etc. We have demonstrated the first nonlinear generation of hollow Gaussian beam and have also proposed the only way of finding the order of hollow Gaussian beam using simple experimental technique.

1.2.4 "Perfect" vortex beam

Recent developments in the field of structured beams provided a new class of optical vortex beam known as "perfect" vortex [12]. Unlike vortices and HGBs, the "perfect" vortices have their size/area independent of its orders. The typical intensity profile of such beam is as shown in Fig. 1.2.1 (c) they have a ring shaped intensity profile. As the nonlinear gain of HGBs and vortex beams generation processes predominantly is a function of intensity, the increase in size/ area of the beam with order acts as a bottle neck in generating higher order LG beams and hollow Gaussian beams. Moreover, as the size and order are coupled for such beams the individual contribution of OAM and size in nonlinear conversion processes can not be separately studied. "Perfect" vortices are the best candidates for studying the individual contribution of size and OAM in nonlinear conversion processes.

Typically, Fourier transformation of the Bessel-Gauss (BG) beam of different orders is used to generate "perfect" vortices [12]. The complex field amplitude of the experimentally realizable "perfect" vortex of order n , at the back focal plane ($z = 0$) of the Fourier transforming lens may be represented in polar coordinates as [12]

$$\tilde{u}_n(\tilde{r}, \tilde{\phi}) = i^{n-1} \frac{w_g}{w_0} \exp\left(-\frac{(\tilde{r} - \rho_r)^2}{w_0^2}\right) \exp(in\tilde{\phi}).$$

As evident from the above expression for "perfect" vortex, the beam size/area remains constant with order. Hence "perfect" vortices generation efficiency should be order invariant, so it is a very good candidate in generating doughnut shaped beams with high topological charges.

1.2.5 Airy beam

M. V. Berry and Nándor L. Balázs demonstrated a non spreading Airy wave packet solution to the Schrödinger equation in 1979. The analogy of paraxial wave equation to Shrodinger equation has led to the quest for such solutions in the optical domain which was realized in the form of finite energy Airy beam in later years [13]. Unlike all the other beams discussed till now which had a azimuthal symmetry, Airy beam intensity profile lacks circular symmetry and looks like an array (see Fig. 1.2.1 (d) and 1.2.2 (c)). The electric field amplitude

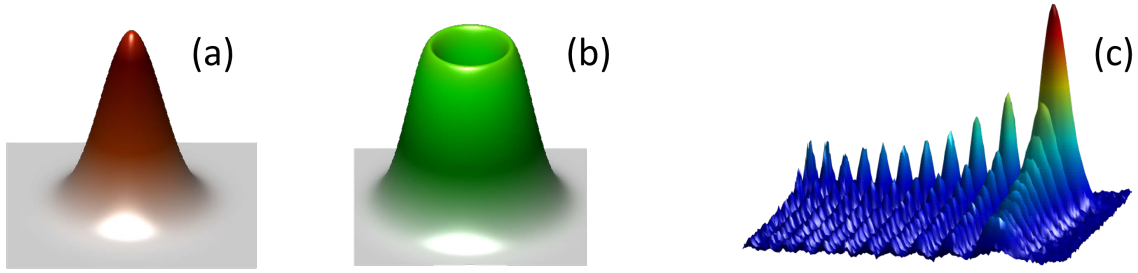


Figure 1.2.2: 3D illustration of intensity distribution of (a) Gaussian, (b) Vortex and (c) Airy beam.

of finite energy Airy beam which can be experimentally realized can be represented in the form

$$\tilde{u}(\tilde{x}, \tilde{y}) = Ai(\tilde{x}) \exp(a_{\tilde{x}}\tilde{x}) Ai(\tilde{y}) \exp(a_{\tilde{y}}\tilde{y}).$$

where Ai is the Airy function and the exponential term determines the finite extent of the beam. Airy beams have many peculiar characteristics such as beam shape invariance with propagation, propagation along curved trajectory in free space, and self-restoration of beam shape even after obstruction by small objects. Due to these unique properties like self healing, self acceleration and non diffraction they find application in particle acceleration, self imaging and light-sheet microscopy. Airy beam can be generated from the Fourier transformation of a cubic phase imposed Gaussian beam.

Although, most of these beams have been well understood and widely used in different fields of science and technology, their nonlinear interaction properties is a field which is not explored exhaustively. Nonlinear optics has shown its potential in accessing high power coherent radiation in otherwise inaccessible spectral regions covered by conventional laser sources although mostly in Gaussian intensity profile. With the correct understanding of the nonlinear interaction properties of these structured beams they could be generated with high power/energy in desired time and spectral domains. It is even possible to manipulate the phase distribution of the output beam by simply choosing the correct choice of the interacting beams (see Chap. 5).

Chapter 2

Nonlinear interaction of coherent radiation in Gaussian

This chapter constitutes the following journal publications:

1. *Type-I frequency-doubling characteristics of high-power, ultrafast fiber laser in thick BIBO crystal,*
Apurv Chaitanya N, A. Aadhi, R. P. Singh, and G. K. Samanta,
Optics Letters 39, 5419 (2014)
2. *High-power, high-repetition-rate, Yb-fiber laser based femtosecond source at 355 nm,*
Apurv Chaitanya N, A. Aadhi, M. V. Jabir, and G. K. Samanta,
Optics Letters 40, 4269 (2015)

2.1 Frequency-doubling of femtosecond pulses in “thick” nonlinear crystals with different temporal and spatial walk-off parameters

2.1.1 Introduction

The development of ultrafast femtosecond laser sources in different spectral regions is of great interest for a variety of applications, including spectroscopy [14, 15], material processing [16, 17], and pumping of optical parametric oscillators [18, 19]. The limited fluorescence bandwidth of solid-state and fiber gain media confines the wavelength coverage of mode-locked ultrafast lasers to restricted regions in the near and mid-infrared. Nonlinear frequency conversion techniques provide a highly effective approach to circumvent this limitation, providing access to new wavelength regions unavailable to conventional ultrafast lasers [20]. Among different nonlinear processes, SHG is typically used to reach the shorter wavelengths, including the visible [21, 22] and ultraviolet regions [19]. In particular, single-pass SHG offers the simplest configuration, which can be realized in a most compact and cost-effective system design [23, 24]. Typically, the single-pass SHG processes have low nonlinear gain. However improvement in the nonlinear gain requires crystals with high optical nonlinearity, long interaction length, as well as high intensity of pump laser. For example, quasi-phase-matched nonlinear crystals such as PPKTP and MgO:sPPLT with long interaction length (30 mm) in single-crystal [25] and cascaded multi-crystal schemes [26], the single-pass SHG technique has been shown to be highly effective in achieving overall conversion efficiency of >50% into the green in the continuous-wave (cw) regime. Similarly, in the picosecond time-scale, use of long birefringent crystals such as BiB_3O_6 (BIBO) [22] and LiB_3O_5 (LBO) [27], has enabled high power single-pass SHG into the green. In the ultrafast femtosecond regime, however, the use of increasingly long crystals does not necessarily lead to higher gain in the SHG process, as other crystal parameters including temporal walk-off can play an increasingly significant role in the overall conversion efficiency, even in the presence of noncritical phase matching (NCPM). In the absence of NCPM, as is commonly the case in birefringent crystals, spatial walk-off becomes an

important additional factor that limits SH efficiency. Hence there is a trade off between how tightly we can focus the beam to achieve high intensity of the pump beam and how big the crystal length can be where effective interaction takes place before the walk off effects come into play [1]. Therefore in the ultrafast femtosecond time-scales, the attainment of the highest conversion efficiency in SHG, as well as other nonlinear frequency conversion processes, requires careful optimization of focusing to account for both spatial and temporal walk-off. For a given nonlinear crystal of a certain physical length and a given input fundamental laser of certain pulse duration and intensity, the optimization of focusing is the most critical factor in attaining highest conversion efficiency and output power. Here we present a comparative study on the optimum focusing condition for SHG of femtosecond pulses in two different nonlinear crystals with different temporal and spatial walk-off parameters. The optimum focusing conditions for efficient SH conversion of cw or long-pulse lasers have been theoretically predicted in the seminal work of Boyd and Kleinman (BK) [1], and subsequently verified experimentally [25]. However, the optimum focusing condition in the presence of temporal walk-off arising from the use of ultrafast lasers can be different from that of the cw and long-pulse lasers. Previously, efforts have been made to model and determine the optimum focusing condition for SHG of ultrafast lasers [3, 2]. However, these efforts require experimental verification. Here, we present a systematic experimental study on the optimum focusing condition for single-pass SHG of ultrashort femtosecond pulses in two nonlinear crystals having different spatial and temporal walk-off parameters and their comparison with the existing theoretical models [3, 2]. For our study, we deploy an ultrafast Yb-fiber laser at 1060 nm as the input fundamental, together with birefringent nonlinear crystals of $\beta \cdot BaB_2O_4$ (BBO) and BIBO under critical phase-matching, for SHG into the green. It is found that for each crystal with comparable values of temporal and spatial walk-off the optimum focusing condition for SHG is more strongly influenced by the spatial walk-off than temporal walk-off. It is also observed that for comparable values of temporal and spatial walk-off the BK theory is also valid for SHG of femtosecond pulses.

2.1.2 Experiment

The schematic of the experimental set up is shown in Fig. 2.1.1, similar to that in [28]. The pump source is an ultrafast Yb-fiber laser (Fianium, FP1060-5-fs) delivering 5 W of average power in pulses of 260 fs duration at 78 MHz repetition rate. When operated at maximum power, the laser provides a linearly polarized output beam in TEM₀₀ spatial profile with $M^2 < 1.3$. The laser wavelength is centered at 1060 nm and the spectrum has full-width at half-maximum (FWHM) bandwidth of 15 nm. For SHG experiments, we use two crystals, BBO and BIBO, to study the performance of the frequency-doubling process with regard to all important output parameters as a function of focusing under different spatial and temporal walk-off conditions. Both crystals are 5-mm-long and 4×8 mm² in aperture. In each case, the input power to the crystal is controlled using a motorized attenuator, consisting of two polarizers and a half-wave plate (HWP). Another HWP is used to obtain the desired polarization for optimum phase-matching in the crystal. A set of six lenses, L , of focal length, $f = 25, 50, 100, 150, 200$ and 300 mm, are used for focusing the fundamental beam into the nonlinear crystal in each case, and a separation mirror, M , filters out the fundamental from the SH output. The BBO crystal is cut at an internal angle $\theta = 22.9^\circ$ for type I ($o + o \rightarrow e$) SHG at a fundamental wavelength of 1064 nm at normal incidence. The BIBO crystal is cut at $\theta = 168.5^\circ$ ($\phi = 90^\circ$) in the optical yz -plane for type I ($e + e \rightarrow o$) phase-matching at normal incidence. Both crystals are antireflection (AR)-coated on both faces at 1064 and 532 nm. For these phase-matching geometries, the spatial walk-off angle in BIBO and BBO are $\rho = 26.1$ mrad and $\rho = 55.85$ mrad, respectively. The corresponding values of group velocity mismatch (GVM) are $\beta = 173$ fs/mm in BIBO and $\beta = 84.8$ fs/mm in BBO. The spatial walk-off length (L_S) and temporal walk-off length (L_T) are defined as $L_S = 2w_p / \tan(\rho)$ and $L_T = \tau_p / \beta$, respectively, where w_p is the pump beam waist radius inside the crystal and τ_p is the pump pulse width. For a pump pulse width, $\tau_p = 260$ fs, the temporal walk-off length is thus calculated to be $L_T = 1.5$ mm in BIBO and $L_T = 2.95$ mm in BBO.

On the other hand, measuring the pump beam waist radius in the BBO and BIBO crystals for lenses of different focal lengths, $f = 25 - 300$ mm, we can estimate the spatial walk-off length, L_S , to vary over 0.48-5.25 mm in BBO, and 1.02-11.39 mm in BIBO.

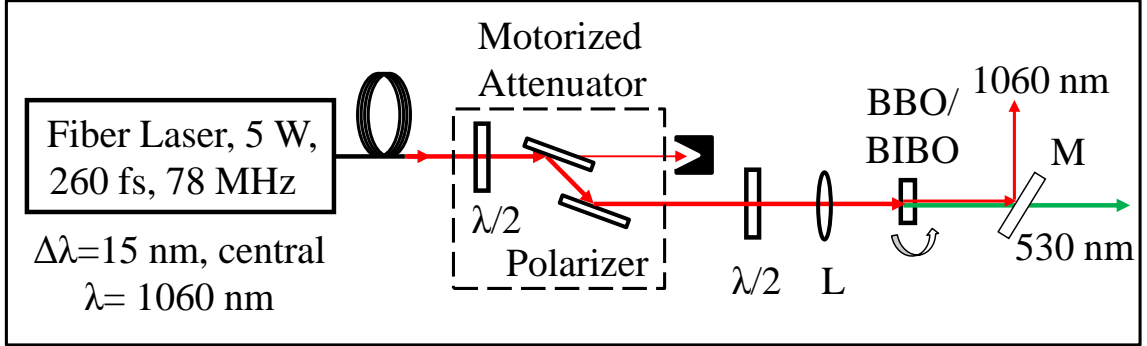


Figure 2.1.1: Experimental design of the single-pass SHG of the femtosecond Yb-fiber laser [28]. $\lambda/2$: half-wave plate; BBO and BIBO: nonlinear crystals, L : lens; M : mirror.

While BBO has twice larger spatial walk-off angle than BIBO under the same focusing condition, the GVM for BBO is almost half that of BIBO. Such differences in spatial and temporal walk-off in the two crystals enable us to study the dependence of optimum focusing for SHG on the two parameters. The relevant characteristics of the BIBO and BBO crystals used in the present study are listed in Table. 2.1

2.1.3 Results and discussion

Optimum focusing condition

To study the effects of temporal and spatial walk-off parameters on focusing dependence of SHG efficiency, we pumped both BBO and BIBO crystals at maximum available fundamental power and measured the SH efficiency under different focusing conditions. We define the focusing parameter, $\xi = L/b$ [1], where L is the crystal length, b is the confocal parameter of the pump beam given by $b = 2n\pi w_p^2/\lambda_p$, n is the refractive index of the crystal, w_p the beam waist radius, and λ_p is the fundamental wavelength. To vary ξ , we focused the pump beam to different waist radii using various focusing lenses. By measuring the beam waist diameter of the pump beam using a scanning beam profiler for six lenses, $f = 25, 50, 100, 150, 200$ and 300 mm, we calculated ξ for both crystals under different focusing conditions. The results, together with the corresponding spatial walk-off lengths, L_S , are listed in Table.2.2.

Parameters	Crystal	
	BIBO	BBO
Crystal length, L (mm)	5	5
Phase-matching type	Type I($e + e \rightarrow o$)	Type I($e + e \rightarrow o$)
Phase-matching angle	$\theta = 168.5^\circ$ ($\phi = 90^\circ$)	$\theta = 22.9^\circ$
Effective nonlinear coefficient, d_{eff} (pm/V)	2.96	55.85
Spatial walk-off, ρ (mrad)	26.1	55.85
Spatial walk-off length, L_S (mm)	0.48-5.25	1.02-11.39
Temporal walk-off, β (fs/mm)	173	84.8
Temporal walk-off length, L_T (mm)	1.5	2.95

Table 2.1: Crystal parameters of BIBO and BBO.

Lens focal length, f (mm)	BIBO			BBO		
	w_p	ξ	L_S	w_p	ξ	L_S
25	13.37	2.63	1.02	14.91	2.86	0.48
50	20.12	1.16	1.54	17.11	1.75	0.61
100	40.21	0.29	3.08	27.88	0.47	1.18
150	62.95	0.12	4.82	33.07	0.16	1.99
200	89.16	0.06	6.83	55.81	0.07	3.05
300	148.75	0.02	11.39	85.37	0.02	5.25

Table 2.2: Beam waist, confocal parameter and spatial walkoff length for BIBO and BBO for different focusing conditions.

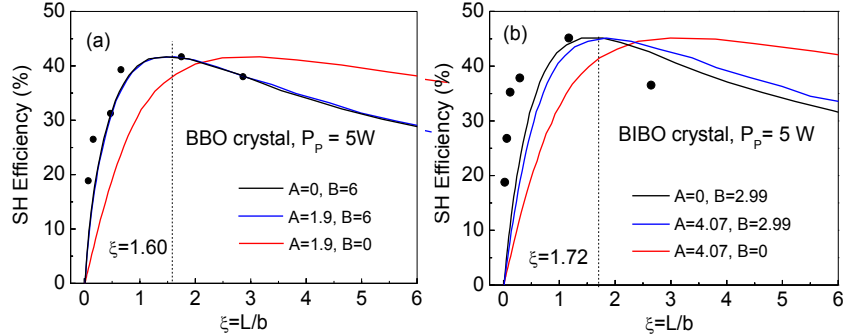


Figure 2.1.2: Variation of SH efficiency as a function of confocal parameter, ξ , for (a) BBO, and (b) BIBO at the maximum input fundamental power of 5 W. The solid curves are theoretical calculations for three different cases involving spatial and temporal walk-off. Blue curve: includes both spatial and temporal walk-off. Black curve: includes only spatial walk-off. Red curve: includes only temporal walk-off. Dotted lines at $\xi = 1.60$ and $\xi = 1.72$ represent theoretical optimum focusing [1] for BBO and BIBO crystals

Figure 2.1.2 shows the variation of the SH efficiency in BBO and BIBO crystals as a function of the focusing parameter, ξ . For completeness of the study, we present here the relevant results obtained in our earlier work on the BIBO crystal [28] in Fig. 2.1.3(b). The filled circles correspond to the experimental efficiency values obtained under the six different focusing conditions. The solid curves are calculations for different conditions of temporal walk-off (A) and spatial walk-off (B) based on our theoretical model described below. As evident from Fig. 2.1.2(a), the SH conversion efficiency obtained with the BBO crystal increases with tighter focusing, reaching a maximum values of 41.65% at $\xi = 1.75$, and decreases with further increase in ξ . Similarly, as shown in Fig. 2.1.2(b), for the BIBO crystal the maximum SH efficiency of 46.5% is reached for $\xi = 1.16$, beyond which there is once again a decline. Under similar experimental conditions, BIBO provides higher SH efficiency than BBO, mainly due to its superior nonlinear coefficient.

To calculate the optimal value of ξ for the highest SH efficiency under our experimental conditions, we used three theoretical models, which are represented by the different color curves in Fig. 2.1.2. The theoretical models correspond to three different cases involving temporal walk-off (A) and spatial walk-off (B): **Case 1:** Blue curve represents the theoretical model that includes the effects of both temporal and spatial walk-off ($A \neq 0, B \neq 0$) in

optimum focusing [2]. **Case 2:** Black curve represents the theoretical model that considers only spatial walk-off ($A = 0, B \neq 0$) [1]. **Case 3:** Red curve represents the model that considers only temporal walk-off ($A \neq 0, B = 0$) [3]. The parameters representing the effect of temporal walk-off (A) and spatial walk-off (B) are given by [2],

$$A = \sqrt{\frac{(\alpha^2 + 16) \ln(2)}{8}} \frac{\beta L}{\tau_p} \quad (2.1.1)$$

$$B = \frac{\rho \sqrt{k_i L}}{2} \quad (2.1.2)$$

$$\sigma = \sqrt{A^2 + 4B^2 \xi} \quad (2.1.3)$$

Here, α represents the amount of chirp in the fundamental pulse, β is the group velocity mismatch between the fundamental and SH pulse, ρ is the spatial walk-off angle in the crystal, τ_p is the fundamental pulse width, k_i is the wave-vector of the fundamental radiation, and L is the crystal length. Substituting the parameter values for BBO ($\beta = 84.75$ fs/mm, $\rho = 55.85$ mrad) and BIBO ($\beta = 173$ fs/mm, $\rho = 26.1$ mrad) crystals, and the pulse duration of the fundamental, $\tau_p = 260$ fs, into Eqn. 2.1.1 and 2.1.2, we calculated the temporal and spatial walk-off parameters for the 5-mm-long BBO and BIBO crystals to be $A = 1.9, B = 6$ and $A = 4.07, B = 2.9$, respectively. For simplicity, we consider that our fiber laser has negligible chirp ($\alpha = 0$). In order to calculate the dependence of SH efficiency on ξ for the three different cases, we use the dimensionless function, $h_m(A, B, \xi)$ [1],

$$h_m(A, B, \xi) = \frac{1}{4\xi} \int_{-\xi}^{\xi} \int_{-\xi}^{\xi} \frac{e^{-\sigma^2(\tau_{x1} - \tau_{x2})^2/4\xi^2}}{(1 - i\tau_{x1})(1 - i\tau_{x2})} \quad (2.1.4)$$

where $\tau_{x1} = 2z/b_{x1}$ and $\tau_{x2} = 2z/b_{x2}$, with b_{x1} and b_{x2} being the confocal parameters of the Gaussian fundamental beam in the horizontal and vertical directions, respectively, and σ as defined by Eqn. 2.1.3. Using the values of A and B , we can then derive the SH efficiency as a function of ξ under the three conditions. For $A \neq 0$ and $B \neq 0$, we derive the blue curves in Fig. 2.1.2, which account for the effect of both temporal and spatial walk-off in optimum focusing (case 1), as in [2]. For no temporal walk-off ($A = 0$), the same function is represented by the black curves, which include only the effect of spatial

walk-off (case 2), as in [1]. With no special walk-off ($B = 0$), the calculation results in the red curves, which include only the effect of temporal walk-off (case 3), as in [3]. As evident from Fig. 2.1.2(a) and Fig. 2.1.2(b), there is a relatively strong discrepancy between the red curve and our experimental data for each crystal, whereas the blue and black curves are in good agreement with both sets of measurements. This confirms that the finite spatial walk-off plays a vital role in the variation of conversion efficiency with the focusing strength in both crystals, as expected. On the other hand, the nearly identical behavior of the blue and black curves in Fig. 2.1.2(a) suggests that the temporal walk-off has negligible or no effect on optimum focusing condition in the BBO crystal, which is due to its small temporal walk-off parameter ($A = 1.9$) arising from a lower GVM ($\beta = 84.75$ fs/mm). Our experimental findings also agree with the earlier theoretical predictions in [2] and [29]. In case of BIBO, shown in Fig. 2.1.2(b), we again find close correlation between the blue and the black curves. This implies that although the BIBO crystal has a larger temporal walk-off parameter ($A = 4.07$), almost twice that of BBO ($A = 1.9$), its role in the optimization of SH conversion efficiency with focusing still remains small. The experimental data in Fig. 2.1.2(b) are most closely in agreement with the black curve predicted by BK theory [1]. This suggests that even if temporal walk-off is more significant in BIBO, spatial walk-off still remains the dominant factor dictating the optimum focusing condition. On the other hand, for large values of GVM in the nonlinear crystal and/or shorter fundamental pulses, temporal walk-off can play an increasingly significant role in the optimization of focusing for SHG [2, 3]. By fitting our experimental data to BK theory [1], represented by the black curves in Fig. 2.1.2(a) and 2(b), we find the optimum values of $\xi = 1.72$ for BBO and $\xi = 1.6$ for BIBO. The shift in the optimum ξ value towards tighter focusing in BIBO as compared to BBO is due to the higher spatial walk-off parameter in BBO ($B = 6$) relative to BIBO ($B = 2.99$), consistent with BK theory [1]. It is also to be noted from Fig. 2.1.2(a) that although the blue and black curves closely fit the experimental data for BBO, one can clearly observe a more significant deviation between the blue and black curves in the case of BIBO in Fig. 2.1.2(b). This deviation can be attributed to the saturation effect and back-conversion at higher fundamental powers arising from the higher nonlinear gain in BIBO. To verify this, we measured the conversion efficiency in both crystals as a function of focusing at lower fundamental powers of 3 W in BBO and 0.5 W in BIBO, with

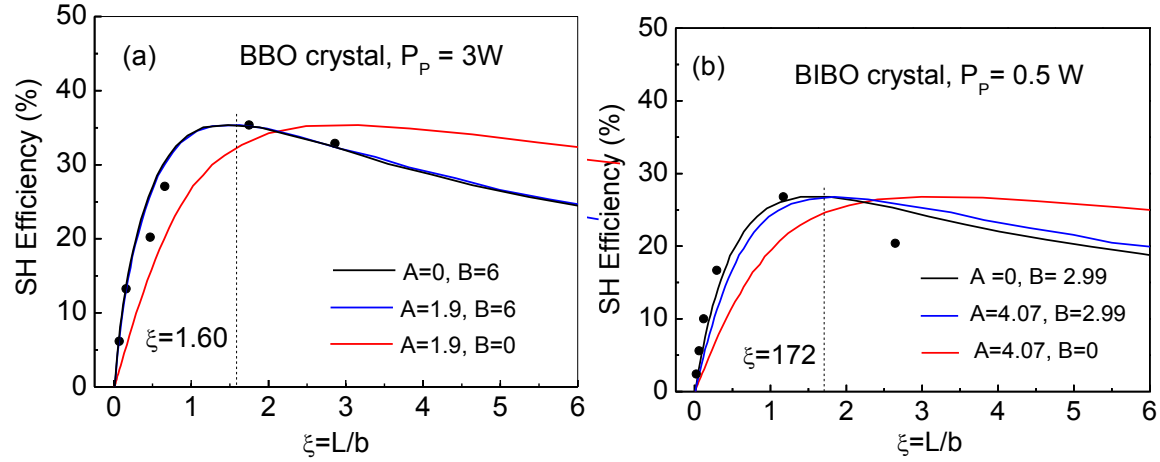


Figure 2.1.3: Variation of SH efficiency as a function of confocal parameter, ξ , for (a) BBO, and (b) BIBO at lower fundamental average powers of 3 W and 0.5 W, respectively.

the results shown in Fig. 2.1.3. As evident from Fig. 2.1.3(a), for BBO the experimental data is again in good agreement with the theoretical fits (blue and black lines), as in Fig. 2.1.2(a). At the same time, as can be seen in Fig. 2.1.3(b), the experimental data for the BIBO crystal at lower fundamental powers are now also in very close agreement with the theoretical fits unlike in Fig. 2.1.2(b), in the absence of saturation and back-conversion. It is to be noted that BK theory [1] is valid under the approximation of low fundamental depletion, hence small conversion efficiency.

From the above study, we thus find that in the presence of both double-refraction and GVM, the optimum focusing condition for SHG of femtosecond pulses in both BBO and BIBO is much more strongly influenced by spatial walk-off than temporal walk-off. Although the behavior might be different for very high values of GVM [3], we can conclude that for moderate temporal and spatial walk-off, the BK theory [1] relevant to frequency-doubling of cw and long-pulse lasers, is also valid for SHG of ultrafast lasers.

Power scaling and saturation effects

To study saturation effects at high conversion efficiency, we investigated the power scaling properties of BBO and BIBO crystals under two different focusing conditions. First, we

focused the pump beam using a lens of focal length $f = 50$ mm to achieve optimum focusing condition of $\xi = 1.75$ in BBO and $\xi = 1.16$ in BIBO, for maximum SH efficiency, and measured the output power as a function of the input fundamental power. The results are shown in Fig. 2.1.4(a). As evident from figure, under optimum focusing conditions, the SH power from the BIBO crystal increases almost linearly with input power, resulting in an output power of 2.25 W for 5 W of fundamental power. While one should expect a quadratic dependence of SH power on the pump power, the linear behavior of the SH power with pump power can be attributed to the saturation effect. This is also evident from the SH efficiency which remains almost constant at $\sim 46.5\%$ for fundamental powers above ~ 2.5 W. On the other hand, for the BBO crystal, we observe slight quadratic dependence of the SH power on pump power, resulting single-pass output power of 2.07 W for 5 W of input power. However, in this case, the SH efficiency exhibits small or no saturation effect. The maximum SH efficiency in the BBO crystal is measured to be $\sim 41.65\%$ at 5 W of fundamental power. To gain more insight into the saturation effects in the two crystals, we repeated the same set of measurements, but now by loosely focusing the pump beam using a lens of focal length $f = 300$ mm, providing the same focusing factor of $\xi = 0.02$ in both the crystals. The results are shown in Fig. 2.1.4(b). As evident from the plots, both crystals now show clear quadratic variation of SH power with input pump power, resulting in 0.46 W (0.95 W) of green power at 9.4% (18.6%) conversion efficiency in BBO (BIBO). The conversion efficiency is almost linear with respect to pump power for both crystals, indicating the absence of saturation effect under the loose focusing.

To understand the saturation effect in both crystals under similar experimental conditions, we consider the SHG conversion efficiency in the plane-wave approximation, with no depletion of the fundamental wave, as given by [30],

$$\eta = \frac{P_{2\omega(L)}}{P_{\omega(0)}} = \eta a_{norm} \left[\frac{P_{\omega} L^2}{A} \right] \text{sinc}^2 \sin \left(\frac{\Delta k L}{2} \right) \quad (2.1.5)$$

$$\eta a_{norm} = \frac{8\pi^2 d_{eff}^2}{n_{\omega}^2 n_{2\omega} c \epsilon_0 \lambda_{\omega}^2}$$

where η_{norm} is the normalized SHG conversion efficiency, P_{ω} is the input fundamental power, A is the fundamental beam area, d_{eff} is the effective nonlinear coefficient, n_{ω} and $n_{2\omega}$ are refractive indices of the crystal at fundamental and SH wavelengths, respectively, ϵ_0

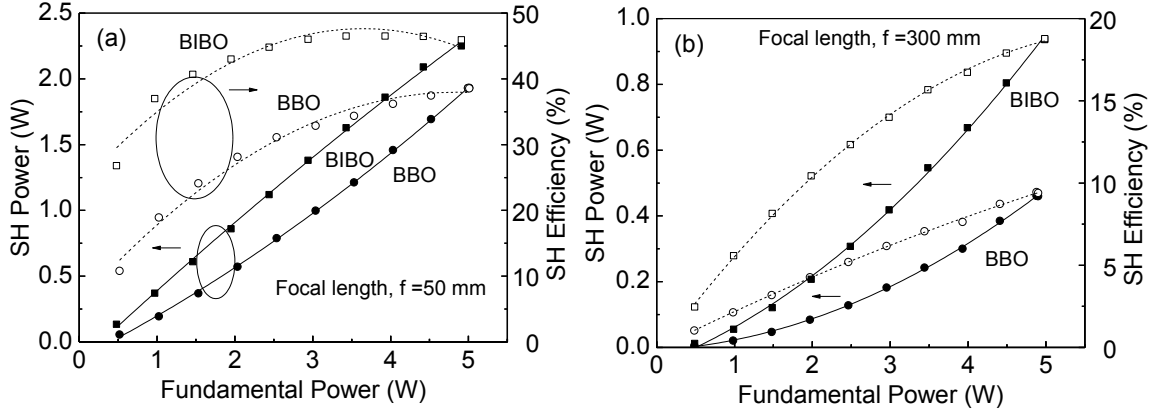


Figure 2.1.4: SH power and efficiency scaling results for BBO and BIBO crystals at different focusing conditions of (a) $\xi = 1.75$ (BBO), $\xi = 1.16$ (BIBO) (b) $\xi = 0.02$ for both the crystals

is the permittivity of free space, c is the velocity of light, λ_ω is the fundamental wavelength, Δk is the phase mismatch, and L is the crystal length. Under perfect phase-matching ($\Delta k = 0$) and similar experimental conditions (same pump power and beam area), the normalized SH efficiency of BIBO (η_{norm}^{BIBO}) is ~ 2.2 times that of BBO (η_{norm}^{BBO}). This is due to the higher nonlinear coefficient of BIBO ($d_{eff} = 2.96$ pm/V) compared to BBO ($d_{eff} = 2.01$ pm/V). Now, we can take the ratio of the SH efficiency of BIBO and BBO crystals shown in Fig. 2.1.5(a) and 2.1.3(b), and plot the ratios as a function of the input fundamental power. The result is shown in Fig. 2.1.5, where we see that for optimum focusing in both crystals (using $f = 50$ mm lens), a value of $\eta_{norm}^{BIBO} / \eta_{norm}^{BBO} \sim 2.4 - 2$ is maintained at lower powers up to ~ 1 W, but drops to 1.09 at the higher pump powers up to 5 W. On the other hand, under loose focusing (using $f = 300$ mm lens), the ratio of the SH efficiency remains almost constant at $\eta_{norm}^{BIBO} / \eta_{norm}^{BBO} \sim 2.6 - 2.02$ for all fundamental powers. This observation clearly indicates that for higher values of focusing parameter, ξ , corresponding to tighter focusing, the SH efficiency in BIBO is increasingly saturated. The result also accounts for the slight deviation of the experimental data in Fig. 2.1.2 (b) from the black curve based on the BK theory [1].

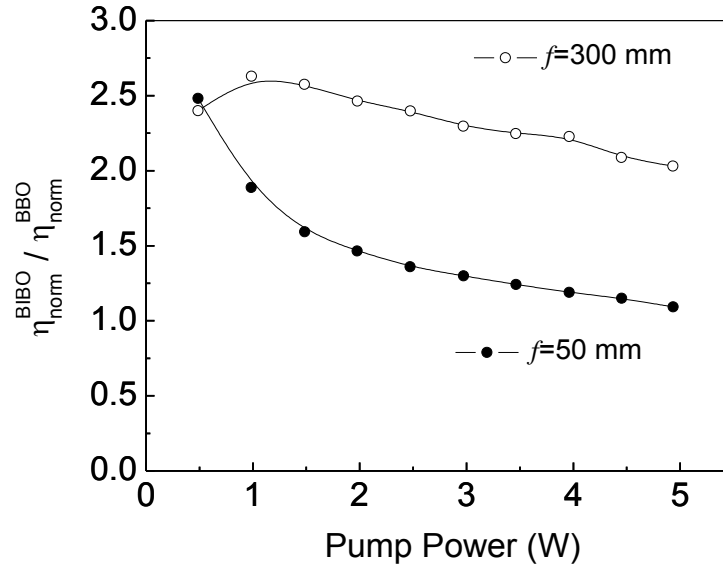


Figure 2.1.5: Variation in the ratio of SH efficiency of BIBO and BBO crystals as a function of input pump power focused using two lenses of focal length, $f = 50$ mm and $f = 300$ mm.

Temporal and spectral characterization of SH pulses

We also characterized the output pulse duration and spectral bandwidth of the green radiation generated by the BBO and BIBO crystals, with the results shown in Fig. 2.1.6. The measurements were performed under optimum focusing condition for both crystals (using a $f = 50$ mm lens), while generating maximum green power when pumping at ~ 5 W of fundamental power. The intensity autocorrelation traces of the SH pulses generated by the two crystals are shown in Fig. 2.1.6(a) and Fig. 2.1.6(b). As can be seen, the autocorrelation profiles conform to Lorentzian pulse shape with measured FWHM duration of ~ 383 fs in BBO and ~ 352 fs in BIBO. Taking account of the deconvolution factor (0.5) for Lorentzian pulse shape, we estimate a SH pulse width of 191 fs for BBO and 176 fs for BIBO. We also measured the spectrum of the generated green radiation for both crystals using a CCD-based spectrometer. The results are shown in the insets of Fig. 2.1.6(a) and Fig. 2.1.6(b). The measurements result in a FWHM spectral bandwidth of 2.35 nm for BBO and 2.45 nm in BIBO, both centered at 532 nm. The time-bandwidth product ($\Delta\tau\Delta\nu$) of the green radiation generated by the two crystals is thus calculated to be ~ 0.54 for BBO and

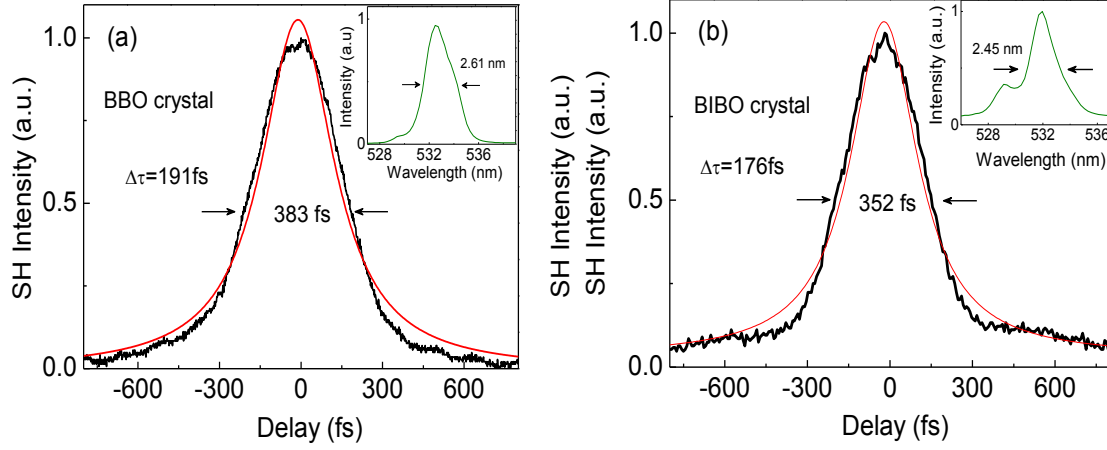


Figure 2.1.6: Typical intensity autocorrelation traces of the green pulses generated from (a) BBO, and (b) BIBO at the maximum output power. Inset: Corresponding SH spectra centered at 532 nm.

~ 0.46 for BIBO, both close to the transform limit. The deviation of the SH pulses from the transform limit is mainly attributed to the non-transform-limited fundamental pulses ($\Delta\tau\Delta\nu = 1.04$). Pulse broadening of the fundamental due to the group velocity dispersion (GVD) is calculated to be only a few femtosecond and thus has negligible effect on the SHG process and output temporal duration.

Effect of focusing on temporal and spectral characteristics

We also studied the variation in pulse duration and spectral bandwidth of the generated green radiation as a function of the focusing parameter, ξ , for both crystals. We pumped the crystals at the maximum available fundamental power of ~ 5 W and measured the pulse duration and spectral bandwidth of the SH output pulses in each case. We then plotted the ratio of the SH pulse duration and spectral bandwidth to that of the input fundamental as a function of ξ . The results are shown in Fig. 2.1.7, where the pulse duration and spectral bandwidth of the pump are ~ 260 fs and ~ 15 nm, respectively. As evident from Fig. 2.1.7(a), the ratio of the SH pulse duration (solid circles) to the pump pulse duration in the BBO crystal has a small variation from 1.1 to 0.51 as the focusing parameter increases from $\xi = 0.02$ to 2.86. The corresponding ratio of the SH spectral bandwidth (open circles)

relative to that of the pump varies from 0.51 to 0.42 with increasing ξ , with a maximum of 0.7 at $\xi = 1.75$. On the contrary, the BIBO crystal shows significant variation in the SH pulse duration and spectral bandwidth with focusing. As can be seen from Fig. 2.1.7(b), the ratio of the SH pulse duration to that of the pump (solid circles) decrease rapidly from 1.75 to 0.83 for an increase in the focusing parameter from $\xi = 0.02$ to 0.29, beyond which the ratio remains almost constant up to $\xi = 2.86$. At the same time, the ratio of the SH spectral bandwidth to that of the pump (open circles) shows inverse behavior to the temporal pulse duration. With the increase in ξ , the spectral bandwidth ratio shows a sharp increase from 0.44, but in the tighter focusing regime ($\xi > 0.29$) it shows a slower variation with focusing. The time-bandwidth product of the generated SH pulses is calculated to vary over $\Delta\tau_{sh}\Delta\nu_{sh} \sim 0.58 - 0.22$ for BBO and $\Delta\tau_{sh}\Delta\nu_{sh} \sim 0.8 - 0.46$ for the BIBO crystal with the increase in the focusing parameter from $\xi = 0.02$ to 2.86, hence with tighter focusing. The dependence of temporal pulse duration and spectral bandwidth on focusing for different values of temporal and spatial walk-off in the two crystals can be explained as follows. The confocal parameter, b , determines the effective length of the nonlinear crystal over which efficient nonlinear interaction takes place. For a fixed physical length of the crystal (L), the value of b reduces with tighter focusing. However, in the presence of spatial walk-off, the effective interaction length of the crystal is further reduced. As a result, an increase in the spectral acceptance bandwidth of the crystal is expected. Therefore, for a given spectral bandwidth of the fundamental ($\Delta\nu_{fund}$) that is larger than the spectral acceptance bandwidth of the physical crystal, more pump bandwidth can be exploited in the SHG process with tighter focusing and stronger spatial walk-off, hence increasing the bandwidth of the SH radiation. As evident from the open circles in both Fig. 2.1.7(a) and Fig. 2.1.7(b), we also observe this experimentally. The bandwidth of the generated SH radiation is large under tight focusing and decreases with loose focusing, becoming almost constant for $\xi < 1$. Another important factor influencing the temporal duration and spectral bandwidth of the SH pulses is the temporal walk-off length of the crystal. Under our experimental conditions, the BBO and BIBO crystals have temporal walk-off length of $L_T = 2.95$ mm and 1.5 mm, resulting in a ratio of physical length to temporal walk-off length (L/L_T) of 1.69 and 3.3, respectively. As theoretically predicted earlier [3], we

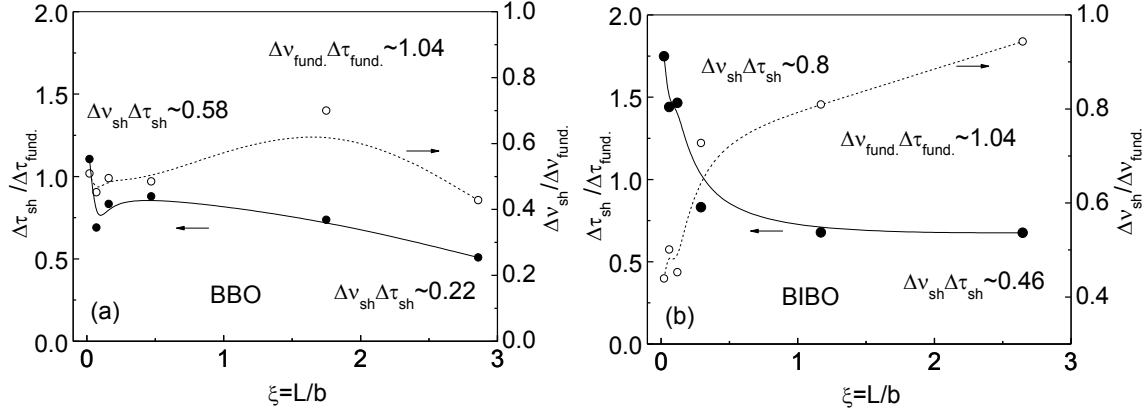


Figure 2.1.7: Variation of the ratio of SH pulse duration and FWHM spectral bandwidth with respect to that of the input fundamental as a function of the focusing parameter, ξ , in (a) BBO, and (b) BIBO.

experimentally observe that in the case of BBO, which has a low L/L_T as compared to BIBO, there is a small variation in the SH pulse duration with focusing.

Effect of focusing on angular acceptance bandwidth

We also investigated the effect focusing on angular phase-matching acceptance bandwidth for frequency doubling of femtosecond pulses under different temporal and spatial walk-off conditions in the two crystals, with the results shown in Fig. 2.1.8. We used a lens of $f = 25$ mm to focus the fundamental beam into the two crystals, resulting in a focusing parameter of $\xi = 2.86$ in BBO and $\xi = 2.63$ in BIBO. We then measured the angular acceptance bandwidth of 5-mm-long BBO and BIBO crystals. The result is shown in Fig. 2.1.8(a), where it is evident that BIBO exhibits a wider angular acceptance bandwidth ($\Delta\theta_{BIBO} = 15.93$ mrad) than BBO ($\Delta\theta_{BBO} = 11.69$ mrad). These experimentally measured values are significantly larger than the theoretical angular acceptance bandwidth for 5-mm BIBO ($\Delta\theta_{BIBO} = 4.62$ mrad) and 5-mm BBO ($\Delta\theta_{BBO} = 2.30$ mrad). Such deviation is expected, and is attributed to tight focusing ($\xi > 2$), and also the wide spectral bandwidth ($\Delta\lambda \sim 15$ nm) of the fundamental beam. However, with increasingly loose focusing, the angular acceptance bandwidths are expected to approach the theoretical values. This is confirmed in Fig. 2.1.8(b), where the variation of experimentally measured angular acceptance

bandwidths of the BBO and BIBO crystal, obtained using lenses of decreasing focal length, is plotted as a function of focusing parameter. Such variation of angular acceptance bandwidth with focusing factor can be understood as follows. As we know, the effective length of the nonlinear crystal changes with focusing. Under very tight focusing, the effective interaction length is significantly reduced compared to the physical length of the crystal, resulting in broadening of the acceptance bandwidth and its deviation from the value under perfect phase matching. Under loose focusing, the effective interaction length of the crystal is increased and, restricting the angular acceptance for phase-matching toward the perfect phase-matching condition. However, when the effective interaction length becomes equal to the physical length, further loosening of focusing has no further impact, resulting in a constant angular acceptance bandwidth. This is evident in Fig. 2.1.8(b), where the angular acceptance bandwidth of both BBO and BIBO crystals is very large under tight focusing (low value of $1/\xi$), gradually decreasing with looser focusing, and finally under very loose focusing (high value of $1/\xi$), becoming almost constant and close to the theoretical value. The angular acceptance bandwidth in case of 5-mm-long BBO crystal varies from 11.69 mrad to 1.33 mrad with increasingly looser focusing from $1/\xi = 0.35$ to 50. Similarly, for BIBO, we observe angular acceptance bandwidth variation from 15.9 mrad to ~ 4.28 mrad for looser focusing from $1/\xi = 0.38$ to 8.3. However, it is to be noted that at any given focusing the angular acceptance bandwidth of BIBO crystal is wider than that of BBO crystal, which is expected due to the lower spatial walk-off in BIBO.

Power stability and spatial beam profile

We further investigated the output power stability and spatial quality of the generated SH output beam in both crystals under optimum focusing condition for maximum SH power and efficiency, using a lens of focal length, $f = 50$ mm, and at the full pump power of ~ 5 W. The results are shown in Fig. 2.1.9. As can be seen, both BBO and BIBO crystals exhibit very similar SH power stability with a peak-to-peak fluctuation as low as $\sim 3.3\%$ for BBO and $\sim 4\%$ for BIBO. Such observation indicates that temporal and spatial walk-off parameters do not play any role in the instability in SH output power, as expected. However, spatial walk-off parameter is expected to make a definite contribution in the spatial profile of the SH output beam. To verify the effect of spatial walk-off, we loosely focused ($\xi \sim$

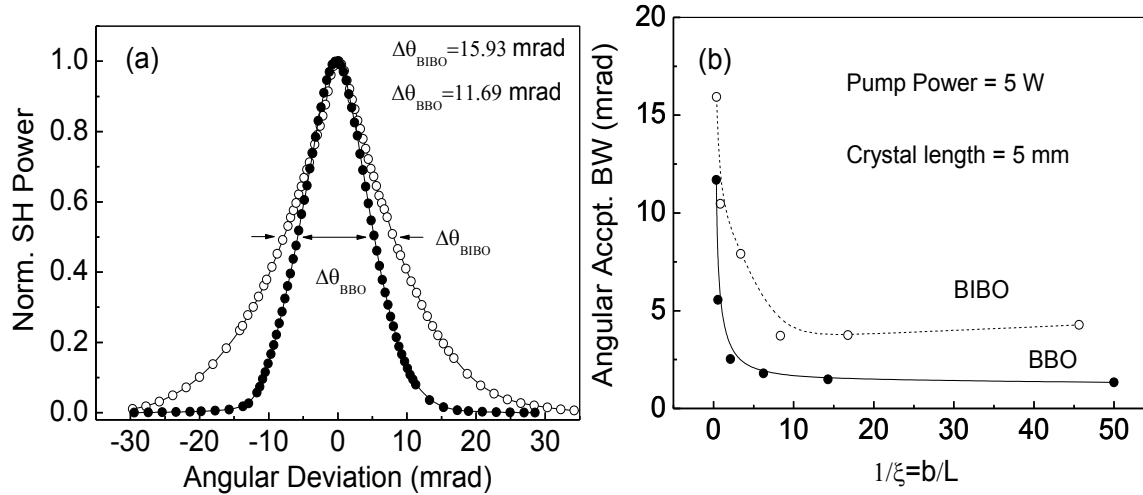


Figure 2.1.8: Variation of the normalized SH power as a function of the internal angular deviation measure at the maximum SH power for both BBO and BIBO. (b) Variation of the SH angular acceptance bandwidth as function of the focusing parameter for both BBO and BIBO crystals.

0.02) the pump beam using a lens of focal length, $f = 300$ mm, at maximum pump power and measured the far-field energy distribution of the SH beam at a distance >2 m from the crystal in each case using a CCD-based beam profiler. The results are shown in the inset of Fig. 2.1.9(a) for BBO and Fig. 2.1.9(b) for BIBO. As evident, the SH beam from both crystals has excellent TEM_{00} spatial profile with circularity $>90\%$ for BBO and $>98\%$ for BIBO. The higher beam circularity in BIBO under same focusing condition is clearly due to the lower spatial walk-off in BIBO ($B = 2.99$) compared to BBO ($B = 6$). However, with the increase in the focusing factor, ξ , under tighter focusing, the circularity of the SH output beam was observed to degrade, but more severely and rapidly in the case of BBO than BIBO. When using a focusing lens of focal length, $f = 100$ mm, the circularity of the SH output beam was reduced to $>34\%$ for BBO ($\xi = 0.47$) and $>74\%$ for BIBO ($\xi = 0.29$). The results are shown in the inset of Fig. 2.1.9(a) for BBO and Fig. 2.1.9(b) for BIBO. For the strongest focusing, using a lens of focal length, $f = 25$ mm, resulting in the highest value of $\xi = 2.86$ in BBO and $\xi = 2.63$ for BIBO, the SH beam circularity was reduced to as low as a few percent in both cases due to the onset of high spatial walk-off. We measured the M2-value of the SH beam generated by the BIBO crystal under optimum

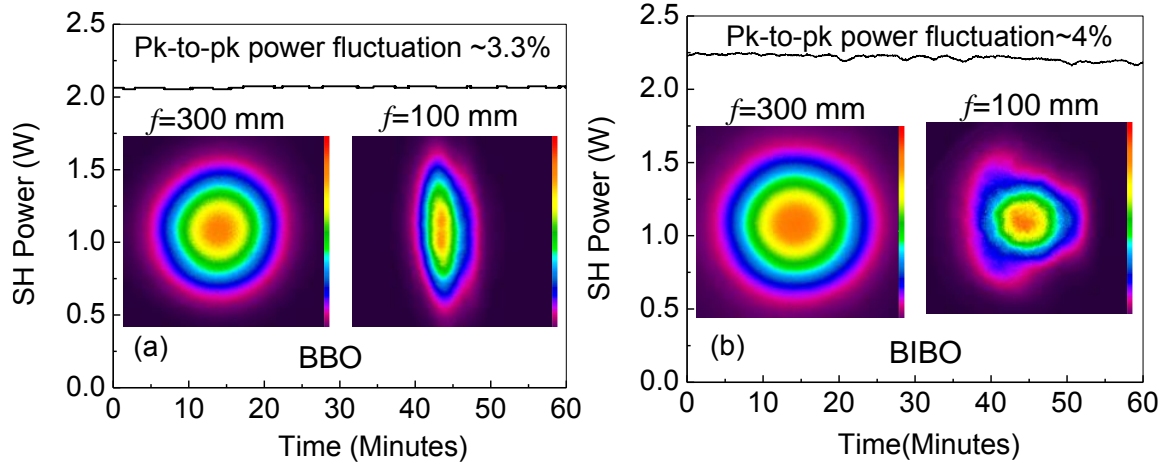


Figure 2.1.9: Long-term power stability over 1 hour and spatial beam profile of the SH beam generated from (a) BBO and (b) BIBO nonlinear crystals. The SH spatial profiles are recorded for lenses of focal length, $f = 300$ and 100 mm for both the crystals.

focusing condition ($\xi = 1.16$) to be $M_X^2 \sim 4.02$ and $M_Y^2 \sim 1.78$, clearly confirming the deterioration of SH beam from a perfect TEM_{00} distribution. In the case of BBO, however, under optimum focusing condition ($\xi = 1.75$), we could not measure its M^2 -value due to high ellipticity of the SH beam. From these measurements, we can conclude that while the higher SH conversion efficiency and output power can be realized under tighter focusing conditions, this will result in a reduction in beam circularity and a deviation from TEM_{00} profile. The circularity of the SH output beams can, however, be readily improved using cylindrical beam shaping optics.

In conclusion, we have experimentally studied frequency-doubling of high-average-power femtosecond pulses from an ultrafast Yb-fiber laser at 1064 nm into the green using thick nonlinear crystals with different temporal and spatial walk-off parameters. Using single-pass SHG in BBO and BIBO, we have investigated the effect of focusing on the SH efficiency and found the optimum focusing conditions for the 5 -mm-long BBO and BIBO, respectively, in the presence of spatial and temporal walk-off. These results are in good agreement with the theoretical calculations performed using the practical values. Under optimum focusing conditions, we were able to generate up to 2.25 and 2.05 W of green output in single-pass configuration for a maximum available fundamental power of ~ 5 W

at 78 MHz pulse repetition rate. We also investigated the effect of focusing on the SH power and efficiency saturation. Spectral and temporal characterization of the generated SH pulses have been performed and the variation of output spectral bandwidth and pulse duration as function of the focusing parameter, ξ , has been studied. Moreover, the angular acceptance bandwidth of both the crystals for SHG into the green has been measured under various focusing conditions and their dependence on the effective interaction length resulting from the spatial and temporal walk-off has been analyzed. This comparative study provides a systematic analysis for the attainment of optimum SH performance with regard to output power, spectrum, pulse duration, and beam quality of the generated green beam in the presence of limiting factors of spatial and temporal walk-off in thick BBO and BIBO crystals for single-pass SHG of the state-of-the art femtosecond Yb-fiber lasers. An important overall conclusion of the present study is that the performance of the SHG process is far more strongly dictated by spatial walk-off than temporal walk-off.

2.2 High-power, high-repetition-rate, Yb-fiber laser based femtosecond source at 355 nm

2.2.1 Introduction

High-power, ultrafast ultraviolet (UV) radiation at high repetition rate is of great interest because of its variety of applications including ultrafast spectroscopy [31], microscopy [32], quantum optics [33], and pumping of optical parametric oscillators [34]. Traditionally, such wavelengths are accessed through nonlinear frequency conversion of solid-state lasers working in the near infrared (IR) wavelength range [35, 36]. The most common drawbacks of such solid-state lasers lay with their bulky and complicated system design, water cooling requirement, and high cost. Although nonlinear frequency-conversion processes, including second-harmonic generation (SHG) and sum-frequency generation (SFG), normally do not require complicated system architecture, the inherent limitations of the solid-state lasers make the overall UV source complicated and costly. Therefore, further advancements of UV sources require alternative lasers in the near-IR wavelength range with a more simplified system architecture and lower cost.

However, in recent times, there has been enormous progress in fiber laser technology providing high-power near-IR coherent radiation in good spatial and spectral qualities. Because of compact, air-cooled, and low-cost systems, fiber laser technology is considered one of the alternatives to their solid-state counterparts. Therefore, nonlinear frequency conversion of such fiber lasers in a single-pass configuration to preserve all the merits of the fiber laser technology can be an interesting route for simple, compact, and low-cost UV sources. In recent times, there has been significant progress with continuous-wave (CW) and mode-locked picosecond ytterbium (Yb)-fiber lasers to access green [25, 22] and UV [37] wavelengths. Lately, the inclusion of high-repetition-rate and high-power ultrafast Yb-fiber lasers in femtosecond time scales has paved access to the green [28] and provided the opportunity to explore UV radiation in femtosecond time scales. However, the attainment of high-power, femtosecond radiation, especially in the UV wavelength range with high conversion efficiency, requires proper selection of a nonlinear crystal with superior crystal parameters including high nonlinearity and damage threshold, low temporal and spatial walk-off, ready availability, and low cost. As such, a comparative study [27] of different crystals of the borate family clearly indicates bismuth triborate (BIBO) as one of the most promising crystals for SFG of ultrafast lasers at 1 μm into the UV wavelength range. At the same time, for given crystal and pump parameters, it is also imperative to study the characteristic parameters, including optimum focusing and power ratio of the interacting beams influencing SFG conversion efficiency. Using two BIBO crystals for SHG and SFG of a Yb-fiber laser in succession, we present the generation of ultrafast UV radiation of average output power as high as 1.06 W at 355 nm in 576 fs pulses with a repetition rate of 78 MHz. Here we present the first experimental work on a Yb-fiber-laser-based femtosecond UV source at 355 nm providing output power >1 W. We also experimentally verified that the efficient SFG process requires interacting pumps to have the same confocal parameters.

2.2.2 Experiment

The schematic of the experimental setup is shown in Fig. 2.2.1. A Yb-fiber laser (Fianium, FP1060-5-fs) of average power 5 W producing output pulses of width ~ 260 fs in sech shape at a repetition rate of 78 MHz is used as the fundamental pump source. It has a

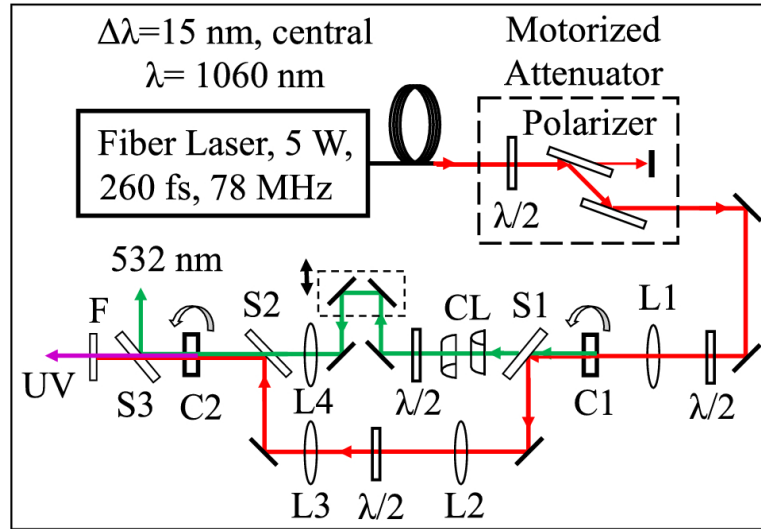


Figure 2.2.1: Experimental schematics for femtosecond UV source. S1– S3, wavelength separating mirrors; L1–L4, lenses; C1, 1.2 mm BIBO crystal for SHG; C2, 5 mm BIBO crystal for SFG; CL, cylindrical lenses; $\lambda/2$, half-wave plate; F, filter.

spectral width of 15 nm centered at 1060 nm. The input power to the nonlinear crystals is controlled using a motorized attenuator similar to the one used in our earlier work [28]. A half-wave plate $\lambda/2$ is used to adjust the polarization of the pump beam. The pump beam is focused at the center of the nonlinear crystal using a lens, L1, of focal length $f = 50$ mm. A 1.2 mm long and 4×5 mm aperture BIBO BiB3O6 crystal (C1) cut at $\theta = 168.5^\circ$ ($\phi = 90^\circ$) in the optical yz plane is used for type-I ($e + e \rightarrow o$) SHG of the pump beam into the green at 532 nm. Another BIBO crystal (C2), which is 5 mm long and 4×5 mm in aperture, cut at $\theta = 142^\circ$ ($\phi = 90^\circ$) in the optical yz plane, is used for type-I ($e + e \rightarrow o$) interaction for SFG of the green beam and the unconverted pump into UV radiation at 355 nm. The effective nonlinear coefficients of the BIBO crystals for SHG and SFG can be calculated to be 2.9 and 3.9 pm/V, respectively. Due to dispersion, the pump and green laser pulses interacting in the SFG crystal travel with different group velocities resulting in poor or no temporal overlapping and reduced SFG efficiency. To control the temporal overlap between the pump and green beams, we have separated the unconverted pump and green beams after the SHG stage using a dichroic mirror (S1). The green beam travels through a phase compensation scheme before recombining with the unconverted

pump by another dichroic mirror, S2, for collinear interaction in the SFG crystal (C2). The ellipticity of the green beam arising from the spatial walk-off (angle $\rho = 26.1$ mrad) effect in the SHG crystal (C1) is partially compensated by circularizing (83%) the green beam with the use of two cylindrical lenses (CL) of focal lengths $f = 75$ and 100 mm. On the other hand, the unconverted pump beam is collimated using lens L2 ($f = 100$ mm). The polarization of both the green and the unconverted pump beams is controlled separately using two different half-wave plates ($\lambda/2$). We have also focused both the beams at the center of the SFG crystal using two different lenses, L3 and L4, and varied their focal lengths to access the optimum beam size of the interacting beams for maximum conversion efficiency. The UV radiation was separated from the residual green beam and pump using a dichroic mirror, S3, and a filter, F (BG40), respectively. The 3 mm thick BG40 (Newport) filter has transmission of 65% at 355 nm.

2.2.3 Results and discussion

We have characterized the performance of the SHG stage for maximum green output power. Based on our recent work on SHG of an ultrafast laser [28], to access higher secondharmonic (SH) power and efficiency, we have focused the fundamental beam at the center of a 1.2 mm long BIBO crystal using a lens of focal length $f = 50$ mm resulting in a beam waist diameter of ~ 30 μm . The corresponding focusing parameter, $\xi = L/b$ [1], can be estimated to be ~ 0.5 . Under such focusing conditions, we measured the variation of the single-pass SH power and corresponding SH efficiency of the BIBO crystal as a function of the pump power, P_p , with the results shown in Fig. 2.2.2. Unlike the quadratic dependence of SH power with pump power, in our case, the SH power increases almost linearly with the pump power, producing SH power as high as 1.72 W at 4.6 W of pump power, clearly indicating the saturation effect. Similarly, the SH efficiency increases linearly at lower pump powers; however, at pump power beyond 2.5 W, the SH efficiency varies from 35% to 37.4% with a maximum single-pass conversion efficiency as high as 39% at 4 W of pump power due to the saturation and roll-off effect (back conversion). The saturation effect, which has also been observed in [28], can be attributed to the high intensity of the ultrafast laser and the

high figure-of-merit of the BIBO crystal. We also measured the pulse and spectral widths of the green beam to be 300 fs and 3.2 nm, respectively.

To study the performance of the SFG stage, we operated the green source at a pump power, $P_P = 4.6$ W, producing green SH power of 1.72 W with a single-pass conversion efficiency as high as $\sim 37.4\%$. The SH and unconverted pump beams were separated at S1 and recombined at S2 after passing through different optical components in respective arms (Fig. 2.2.1). Due to losses in different optical components, the SH and unconverted pump powers before the 5 mm long BIBO crystal are measured to be $P_{SH} = 1.47$ W and $P_{UP} = 2.47$ W, respectively. Initially, we focused both the beams at the center of the SFG crystal using a single lens (not shown in the Fig. 2.2.1). Using two different values of focal lengths $f = 25$ mm and $f = 50$ mm, we recorded single-pass UV conversion efficiency of $\sim 7.7\%$ and 13.0% , respectively. To identify the possible reasons for such low conversion efficiency, we measured the beam waist diameter of both the beams separately and observed that the high beam divergence while focused using a small focal length lens ($f = 25$ mm) reduces spatial overlapping between the interacting beams. In addition, the longitudinal offset in the focus position of the interacting beams arising from the chromatic aberration of the lens also reduces beam overlap and, hence, conversion efficiency. At loose focusing ($f = 50$ mm) the interacting beams have more spatial overlap resulting in higher conversion efficiency. One can, in principle, improve the beam overlapping by loosely focusing the interacting beams; however, the dependence of conversion efficiency on the intensity of the interacting beams does not always warrant higher conversion efficiency with increased beam overlapping. Therefore, for fixed crystal length and beam powers, the maximum conversion efficiency can be realized as a trade-off between the beam overlap and the spot size of the interacting beams. However, such a trade-off cannot be experimentally realized while focusing both the interacting beams using a single lens.

To verify the focusing conditions of the interacting beams required for optimum SFG efficiency, we focused the unconverted pump and green beams at the center of the C2 crystal separately using lenses L3 and L4, respectively. We fixed the powers of the unconverted fundamental and the green beams at 2.47 and 1.47 W, respectively, and measured the UV power for different ratios of the confocal parameters of the green beam b_{SH} and unconverted pump b_{UP} with the results shown in Fig. 2.2.3. To change the ratio of the confocal

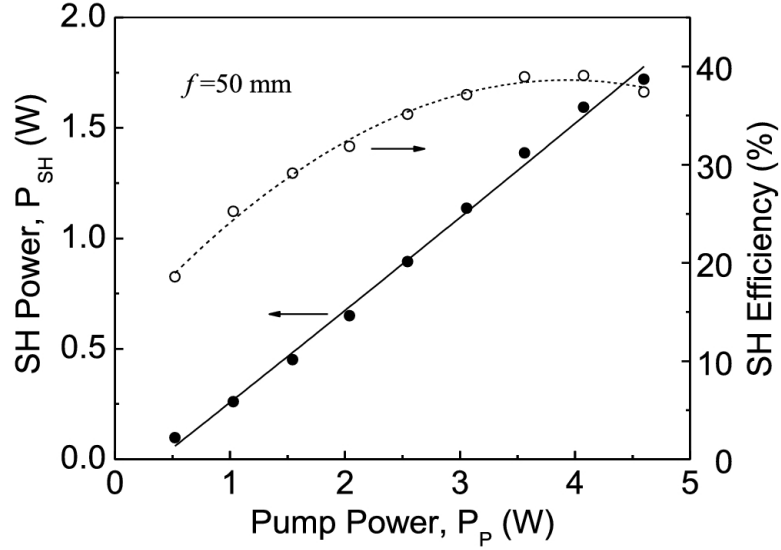


Figure 2.2.2: Variation of SH power and efficiency with pump power. Lines are guides to eyes.

parameters, we have used different combinations of the focal lengths of lenses L3 and L4. As is evident from Fig. 2.2.3, the UV power, P_{UV} , and efficiency, $\eta = P_{UV}/P_{UP} \times P_{SH}$, of the 5 mm long BIBO crystal vary from 0.68 W and 18.7%/W to 0.81 W and 22.5%/W, respectively, for the increase of b_{UP}/b_{SH} from 0.11 to 3.4 with a clear indication of maximum UV power (efficiency) of 1.07 W (29.5%/W) at $b_{UP}/b_{SH} = 1$. Such observation proves that, for efficient nonlinear frequency conversion, one needs to match the confocal parameters of the interacting beams. It is to be noted that, for each measurement, we have optimized the focusing position of the interacting beams by moving the lenses L3 and L4 and observed that the higher conversion takes place when both the beams are focused at the same point. Similar to Ref. [38], we have also observed that a small angle ($< 3^\circ$) between the green and unconverted pump beams is required to compensate the relative spatial walkoff ($\Delta\rho = 3.2$ mrad) between the green and unconverted pump beams for the best temporal and spatial overlap.

The UV power and conversion efficiency, as shown Fig. 2.2.3, vary slowly in the range $1 < b_{UP}/b_{SH} < 3.5$. Such an effect can be understood as follows. In the case of SFG, one photon from each of the green and unconverted pump beams annihilates to generate a UV photon. Therefore, ideally the power ratio of the interacting pump beams, P_{UP}/P_{SH} , should

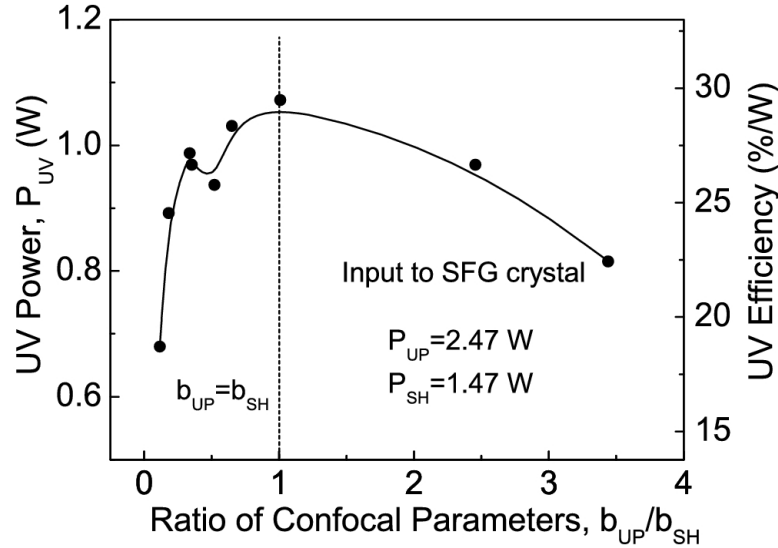


Figure 2.2.3: Variation of UV power and conversion efficiency as a function of the ratio of confocal parameters of the interacting pump beams. Lines are guides to eyes.

be one half to get the highest conversion efficiency. In practice, the nonlinear conversion processes are low efficiency processes. Most of the photons of the two pump beams do not interact with each other to generate a new photon. However, the interaction (conversion) efficiency increases with the intensity of both of the pumps. In our experimental condition, the ratio of the pump powers is $P_{UP}/P_{SH} = 1.7$. As a result, a higher value of $b_{UP}/b_{SH} > 1$ realized through loose focusing of the unconverted pump beam does not reduce the intensity of the unconverted pump for substantial reduction in UV conversion efficiency. At further loose focusing, as well as lower values of P_{UP}/P_{SH} , one can expect rapid reduction in UV efficiency. For different values of P_{UP}/P_{SH} , we expect to have a similar curve as in Fig. 2.2.3; however, the maximum UV power and efficiency will be reached when the confocal parameters of both the pump beams are equal, $b_{UP}/b_{SH} = 1$.

For further understanding of the effect of the pump power ratio, P_{UP}/P_{SH} , on UV power, P_{UV} , we have focused pump beams at the optimum focusing condition, b_{UP}/b_{SH} , and measured the UV power with the increase of unconverted pump power, P_{UP} , for different values of green power, P_{SH} , with the results shown in Fig. 2.2.4. Ideally, the UV power should increase with P_{UP}/P_{SH} resulting in a maximum UV power and efficiency at $P_{UP}/P_{SH} = 1/2$ and remain constant or roll off due to back-conversion with further increase of P_{UP}/P_{SH} .

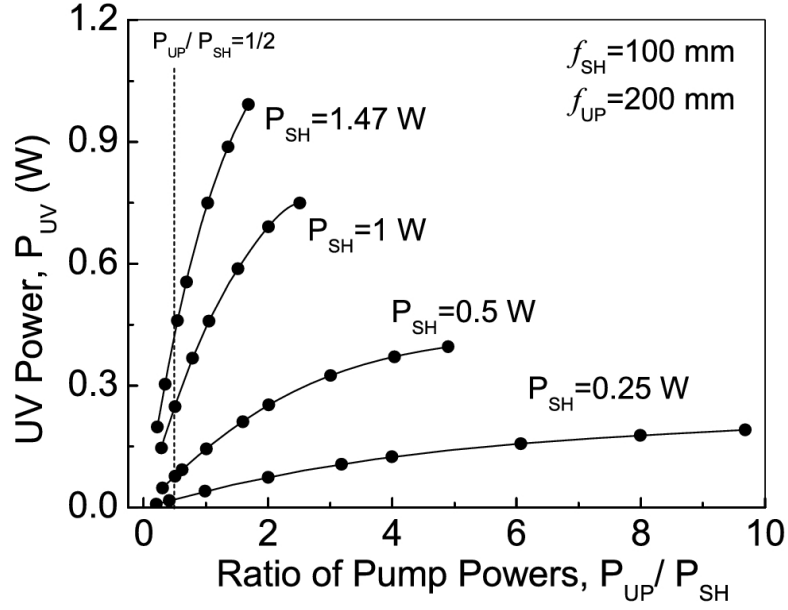


Figure 2.2.4: Dependence of UV power with the power ratio of the interacting pumps focused under equal confocal parameters in SFG crystal. Lines are guides to eyes.

However, in practice, we observe a completely different picture. As is evident from Fig. 2.2.4, for all green powers, $P_{SH} = 0.25, 0.5, 1,$ and 1.47 W, the UV power increases with P_{UP}/P_{SH} even after the ratio has crossed $P_{UP}/P_{SH} = 1/2$. Such an effect can be attributed to the fact that the SFG power is proportional to the product of the intensities of the two pump beams. As a result, the increase of P_{UP} for a fixed value of P_{SH} or vice versa increases the resultant driving intensity and generated output power. From Fig. 2.2.4, we also observe saturation in UV power with the increase of P_{UP}/P_{SH} ; however, at lower (higher) values of P_{SH} , the saturation effect appears at higher (lower) values of P_{UP}/P_{SH} . Therefore, generation of higher-power UV radiation in the SFG process requires an increase in the product of driving intensities and then maintaining the optimum power ratio of P_{UP}/P_{SH} . As such, generation of UV power will intrinsically maintain the power annihilation ratio of the interacting pumps as $P_{UP}/P_{SH} = 1/2$.

We also studied the power scaling characteristics of the UV source. We focused the unconverted fundamental and green beams at the center of the SFG crystal using lenses L3 and L4 of focal lengths 200 and 100 mm, respectively, satisfying the optimum focusing condition, b_{UP}/b_{SH} , and measured the UV power while varying the pump power, P_p , to the

SHG crystal with the results shown in Fig. 2.2.5. The UV power and the UV efficiency increase with the increase of the pump power P_P , resulting in a maximum UV power of 1.06 W, corresponding to a single-pass near-IR-to-UV conversion efficiency as high as 22%. It is to be noted that we have not done any correction for the losses arising because of different optical elements in the path of the green and unconverted beams while calculating the efficiency. As is evident from Fig. 2.2.5, the UV power varies quadratic to the fundamental pump power, which is also evident from the linear dependence of UV power with the square of the pump power (inset of Fig. 2.2.5). The quadratic dependence of the UV power with the pump power can be understood as follows. In the current experiment, we have used two-step processes (SHG and SFG) to reach from near-IR to UV. For small signal approximation, the SHG power, P_{SH} , and SFG power, P_{UV} , are proportional to P_P^2 and P_P^3 , respectively [39]. However, as is also evident from Fig. 2.2.2, due to the saturation effect in the SHG process resulting from high peak power, tight focusing, and high figure-of-merit of the BIBO crystal [27], the SHG power is proportional to the pump power. As a result, the SFG power, P_{UV} , which is proportional to the product of P_{SH} and the unconverted pump P_{UP} , can be approximated to be proportional to the square of the pump power P_P . However, at higher pump powers, the UV power is almost linear to the pump power, indicating the saturation effect.

We measured the angular acceptance bandwidth of the BIBO crystal for SHG and SFG of an ultrafast laser with the results shown in Fig. 2.2.6. For SHG, we focused the pump beam of power, $P_P = 4.6$ W, at the center of the 1.2 mm long BIBO crystal using lens L1 of focal length $f = 100$ mm and measured the SH power while varying the angle of the BIBO crystal. Similarly, for SFG, we focused both green and unconverted pumps of powers 1.47 and 2.47 W, respectively, at the center of the 5 mm long BIBO crystal under the optimum focusing condition, b_{UP}/b_{SH} , and measured the UV power while varying the crystal angle. As is evident from Fig. 2.2.6, the angular acceptance bandwidths of the SHG (open circle and dotted sinc^2 fit) and SFG (solid circle and solid sinc^2 fit) processes of the ultrafast laser in the BIBO crystal can be measured to be 8.7 mrad (1.044 mrad · cm) and 4 mrad (~2 mrad · cm), respectively. The theoretical acceptance bandwidths of the BIBO crystal for type-I SHG and SFG processes are given as ~1.16 mrad · cm and 0.29 mrad·cm [40], respectively. While the angular acceptance bandwidth of the 1.2 mm

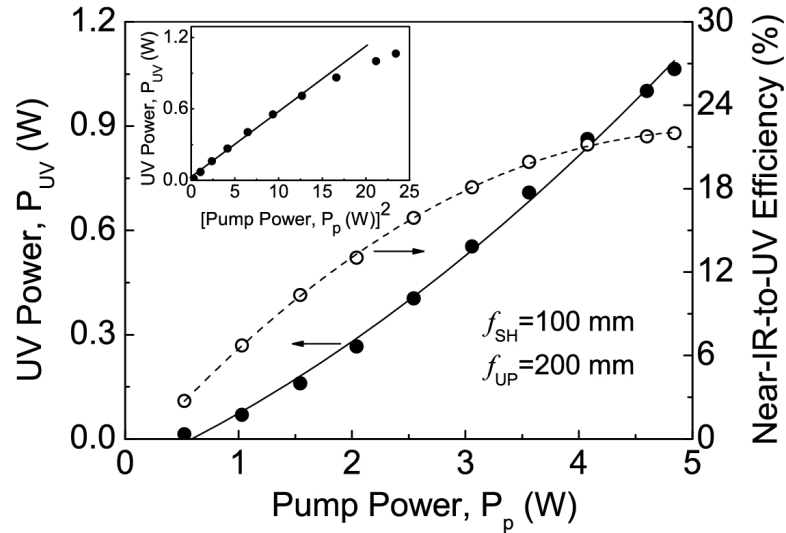


Figure 2.2.5: Variation of UV power and near-IR-to-UV conversion efficiency with fundamental pump power. (Inset): dependence of UV power with the square of the pump power. Lines are guides to eyes.

long BIBO crystal matches the theoretical values, we can observe a significant broadening in the angular acceptance bandwidth of the SFG process in the 5 mm long BIBO crystal. Such discrepancy can be attributed to the decrease of effective crystal length resulting from a high spatial walk-off angle [27] of the BIBO crystal for the SFG process. A similar broadening effect was also observed previously [28] for SHG of an ultrafast laser in a 5 mm long BIBO crystal at tighter focusing.

We also measured the long-term passive power stability of the UV source with a natural peak-to-peak power fluctuation $<2.2\%$ in short term (2 h), however, there is a clear drift in UV power at a rate of 0.76. Such power drift can be attributed to the different thermal effects in the BIBO crystal [27]. The UV beam has TEM_{00} spatial mode $M^2 < 2.45$ in elliptical beam shape (ellipticity 52%) due to the walk-off effect in the BIBO crystal. We also measured the spectral and temporal width of the UV source as ~ 1.6 nm and ~ 576 fs, respectively, with time-bandwidth product ~ 2.19 .

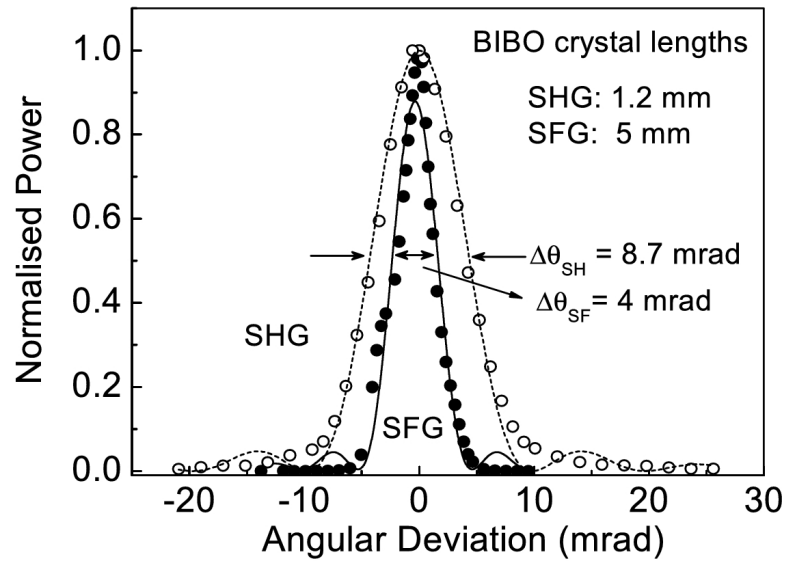


Figure 2.2.6: Angular acceptance bandwidth of 1.2 mm long and 5 mm long BIBO crystals for SHG and SFG processes, respectively. Lines (solid and dotted) are sinc² fits to the experimental data.

Chapter 3

Nonlinear interaction of high power ultrafast vortex beams

This chapter constitutes the following journal publications:

1. *Frequency-doubling characteristics of high-power, ultrafast vortex beams*,
Apurv Chaitanya N, A. Aadhi, M. V. Jabir, and G. K. Samanta,
Optics Letters 40, 2614 (2015)
2. *Ultrafast optical vortex beam generation at 266 nm*,
Apurv Chaitanya N, S. Chaitanya Kumar, K. Devi, and G. K. Samanta, M.
Ebrahim-Zadeh,
Optics Letters 41, 2715 (2016).

3.1 Frequency-doubling characteristics of high-power, ultrafast vortex beams at 532 nm

3.1.1 Introduction

Singularities are the places where physical quantities change abruptly or become infinite. In optics, the presence of such singularities (phase dislocations) in the wavefront of the light beams modifies the phase and intensity structure of the beams. As the phase of the

beam is indeterminate at the singularity, the beam has vanishing intensity at the center. If a beam has a screw-like (helical) phase structure around the point of singularity, the angular momentum associated to the azimuthal component of the Poynting vector orbits around the singular point. Such beams are called optical vortices. The characteristic phase distribution of optical vortices is represented as $\exp(il\theta)$, where θ is the azimuthal angle. The integer l , known as vortex order or topological charge, indicates the OAM carried by each photon of the beam.

Since the discovery of OAM associated with such structures [4], optical vortices have found applications in many fields, including quantum information [11], high resolution microscopy [41], particle micro manipulation and lithography [10], and material processing [42]. However, some of the applications [43] require high-power, ultrafast optical vortices at lower wavelengths. Conventionally, the optical vortices are realized through the phase modulation of Gaussian beams using SLMs [44] or SPPs [45]. Despite the flexibility of SLMs in terms of wide wavelength coverage and dynamic phase modulation, the high damage threshold has made SPPs inevitable for high-power optical vortices. However, due to high wavelength sensitivity of SPPs, a single SPP cannot be used to generate high-quality vortices over broad wavelength range. Additionally, due to the practical limitations of current technology, fabrication of SPPs for lower wavelengths and a higher-order optical vortex ($l > 4$) is the main challenge to overcome. Therefore, it is imperative to devise alternative techniques to access high-power, higher-order optical vortices especially at lower wavelengths. As such, lower wavelengths are routinely accessed through the nonlinear frequency conversion processes [46, 23], e.g., frequency doubling, tripling, or SFG. Therefore, nonlinear frequency conversion of the optical vortices produced through readily available SPPs at longer wavelengths (near-IR) can in principle be the most straightforward route to generate higher-order optical vortices at lower wavelengths. However, success of such approaches especially to generate high-power vortices requires proper understanding about the characteristic parameters influencing the vortex interaction with a nonlinear medium. Here, we present a systematic study of characteristic parameters influencing the frequency-doubling efficiency of optical vortices in generating high-power, high efficiency, and higher-order optical vortices at lower wavelengths. Although our study is restricted only to SHG of 1064 nm generating ultrafast vortices at 532 nm with power as much as

900 mW and order as high as 12, one can expect similar results for frequency doubling at other wavelengths. Using linear optical elements we have also devised a novel scheme to double the order of the vortices without changing their wavelength.

3.1.2 Experiment

The schematic of the experimental setup is shown in Fig. 3.1.1. A 5 W Yb-fiber laser (Fianium, FP1060-5-fs) with spectral line width of 15 nm at 1060 nm providing sech^2 shaped femtosecond pulses of width ~ 260 fs at 78 MHz repetition rate is used as the fundamental laser source. The input power to the SHG crystal is varied using a polarization-based attenuator [28]. Two spiral phase plates (Holo/Or, Israel), SPP1 and SPP2 of high damage threshold (~ 3 J/cm² at 7 ns pulsed at 1064 nm) are used to convert a high-power Gaussian beam into optical vortices of orders $l_p = 1$ and $l_p = 2$, respectively, at conversion efficiency $>95\%$. Due to limited availability of SPPs producing vortices of order $l_p > 2$, we have used a vortex-doubler setup comprised of a polarizing beam splitter cube (PBS), quarter-wave plate ($\lambda/4$), and dielectric coated mirror, M1, with high reflectivity at 1064 nm. The working principle of the vortex-doubler can be understood as follows: the horizontally polarized Gaussian beam after the attenuator passes through the PBS. In forward pass through the SPP1, the Gaussian beam acquires spiral phase corresponding to an optical vortex of order $l_p = 1$ (say). The polarization (horizontal) of the beam converts into circular polarization (left circular) after passing through the $\lambda/4$ plate having its axes at 45° to its polarization axis. However, the handedness of the beam gets reversed (right circular) on reflection from the mirror, M1, at normal incidence. In the return pass through the $\lambda/4$ plate, the right circularly polarized beam converts into vertically polarized and gets reflected from the PBS. The input and output beams of the vortex doubler have orthogonal polarization. On the other hand, reflection from the mirror, M1, reverses the sign of the vortex charge from $l = +1$ into $l = -1$ and vice versa. The return beam ($l_p = -1$) sees the direction of phase variation of the SPP1 opposite to that of the forward pass. Therefore, while passing through the SPP1, the return beam acquires additional spiral phase (-1). As a result, the output beam of the vortex-doubler has vorticity twice that of the phase winding of the SPP placed inside. Using different combinations of SPP1 and SPP2, only two

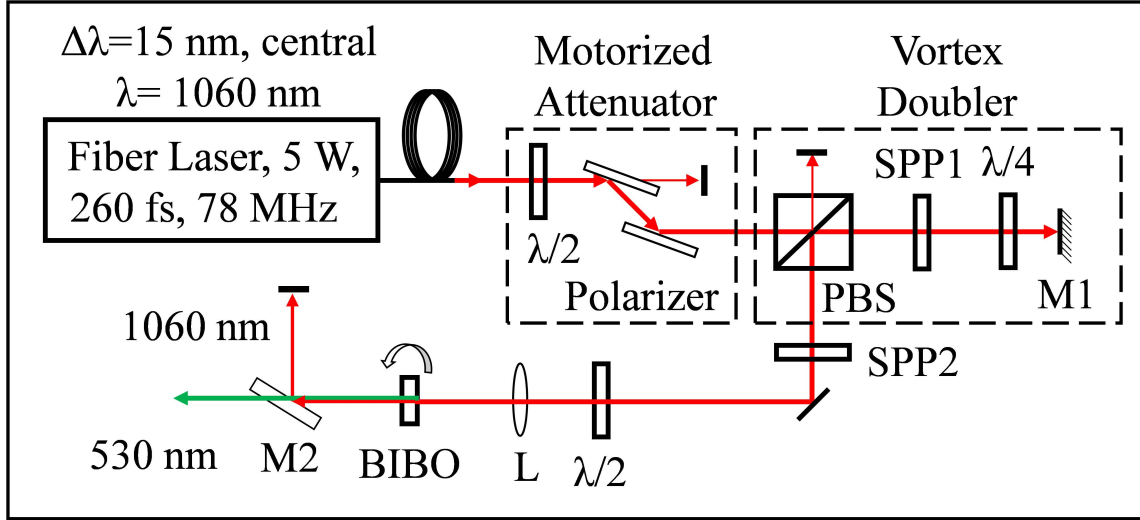


Figure 3.1.1: Schematic of the experimental setup for SHG. $\lambda/2$, halfwave plate; SPP1,2, SPPs; PBS, polarizing beam splitter cube; $\lambda/4$, quarter-wave plate; L, lens; M1,2, mirrors; BIBO, nonlinear crystal for frequency doubling.

phase plates, placed inside and outside the vortex-doubler we have generated optical vortices of topological charges $l_p = 1, 2, 3, 4, 5$, and 6. A 1.2 mm long and 4 mm \times 8 mm in aperture BIBO crystal cut for type-I ($e + e \rightarrow o$) SHG in optical yz -plane ($\varphi = 90^\circ$) with internal angle of $\theta = 168.5^\circ$ at normal incidence is used for collinear frequency doubling of vortices at 1064 nm. Crystal faces are antireflection-coated for both fundamental and second-harmonic (SH) wavelengths. Polarization of the fundamental beam is adjusted using a second $\lambda/2$ plate for perfect phase matching depending upon the orientation of the SHG crystal. A set of lenses of different focal lengths $f = 25, 50, 100, 150, 200$, and 300 mm is used to focus the fundamental beam at the center of the SHG crystal. The SHG beam is extracted from the fundamental using mirror, M2.

3.1.3 Results and discussion

We have recorded the intensity profile of the fundamental and corresponding SH beam using a CCD-based beam profiler (SP-620U, Ophir) with the results shown in Fig. 3.1.2. The first column (a)–(c) of Fig. 3.1.2 represents the intensity pattern of the fundamental beam, recorded before the focusing lens, L, with vortex orders $l_p = 1, 3$, and 6, respectively.

To confirm the vorticity and order of the fundamental beam, we interfered it with a plane wave at 1064 nm and recorded the interference pattern, as shown in the second column of Fig. 3.1.2. A close observation of the interference pattern of Figs. 3.1.2(d)–3.1.2(f) reveals the characteristic fork patterns corresponding to vortex orders $l_p = 1, 3,$ and $6,$ respectively, located at the center of the beam. Such observation clearly certifies the capability of the vortex-doubler setup in generating high-quality optical vortices even at higher values of topological charges. The third column [(g)–(i)] of Fig. 3.1.2 represents the intensity pattern of SH beams generated respectively from pump vortices $l_p = 1, 3,$ and 6 focused at the center of the BIBO crystal using a lens, $f = 100$ mm. Given the size of the dark core increases with order [30] and also evident from Figs. 3.1.2(g)–3.1.2(i), it is difficult to observe the characteristic fork pattern while interfering higher-order optical vortices with plane wave front. In addition, the interferometric technique requires the reference beam with the same spectral characteristics as that of the SH beam. To avoid such stringent requirements we used the tilted lens technique [47] to determine the order of the SH beams. The SH vortex beams of order l_{sh} after passing through a spherical lens of focal length 30 cm, tilted about the y (vertical) axis at an angle $\sim 6^\circ$, as shown in the fourth column of Fig. 3.1.2, split into $|l| + 1$ bright lobes. As evident from Figs. 3.1.2(j)–3.1.2(l), the SH beams possess vortex orders, $l_{sh} = 2, 6,$ and $12,$ respectively, twice the order of the pump vortices, confirming the conservation of OAM in SHG [48].

It is well known that the higher-order optical vortices normally decay into an array of unit charge vortices due to the perturbation, anisotropy, and also the walk-off effect arising from the birefringence of the nonlinear media. However, while doing vortex-vortex interferometry of SH vortices of orders 2, 4, and 6 we did not observe any such splitting in the SH vortices. This can be attributed to the low spatial walk-off ($\rho = 26.1$ mrad), use of small thickness (1.2 mm) of the BIBO crystal, and loose focusing. However, at tighter focusing using a lens of focal length, $f < 50$ mm, and use of a longer (5 mm long) BIBO crystal, we have observed splitting of the higher order SH vortices into a collection of smaller orders.

Recently, it has been reported [49] that the frequency doubling efficiency of optical vortices is independent of their topological charge. This can be true for “perfect vortices” [12], a new class of optical vortices whose beam diameter is independent of its topological

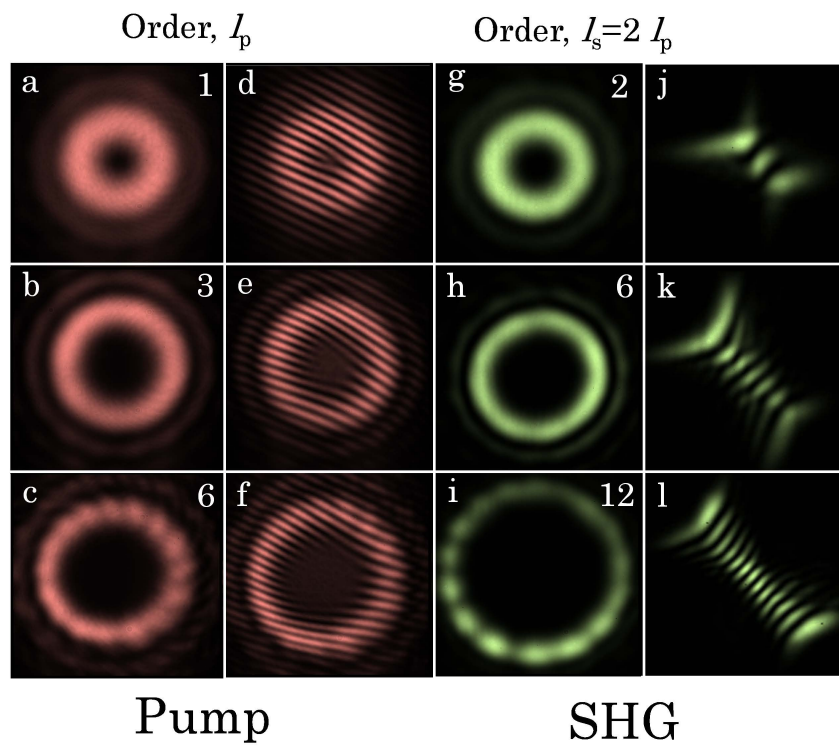


Figure 3.1.2: (a)–(c) Far-field intensity distribution of pump vortices and (d)–(f) corresponding interference pattern. (g)–(i) Intensity distribution of the generated SH beams, and (j)–(l) splitting of SH vortices into their characteristic lobes by tilted lens.

charge. However, in all practical purposes, the diameter of the optical vortices increases with their order [50]. Therefore, it is imperative to verify frequency-doubling characteristics of optical vortices of different topological charges. To understand the variation of SH power with vortex order, we write the field amplitude of a Gaussian embedded vortex beam with OAM order of l and average power of P at a distance z [4] as,

$$E_p^l = \sqrt{\frac{P}{\pi l! \epsilon_0 n_p c}} \frac{(r\sqrt{2})^l}{\left[w_0 \left(1 + i\frac{z}{Z_R}\right)\right]^{l+1}} \exp\left(-\frac{r^2}{w_0^2 \left(1 + i\frac{z}{Z_R}\right)}\right) \quad (3.1.1)$$

where n_p is the refractive index of the crystal, w_0 , is the pump beam waist radius with corresponding Rayleigh range of $Z_R = n_p \pi w_0^2 / \lambda_p$, and λ_p is the pump wavelength. Without loss of generality, if we consider $z = 0$ as the observation plane, the intensity of the vortex beam can be represented as

$$I_p^l = \frac{1}{\epsilon_0 n_p c \pi w_0^2} \frac{1}{l!} \frac{(r\sqrt{2})^{2l}}{[w_0]^{2l}} \exp\left(-\frac{2r^2}{w_0^2}\right) \quad (3.1.2)$$

Equation (3.1.2) indicates that the intensity of the vortex beam decreases asymptotically with the order of the vortex. As the frequency-doubling efficiency is proportional to the intensity of the pump beam [8], theoretically one expects an asymptotic decrease of vortex SH efficiency with order. For experimental verification of order dependent SH efficiency of the optical vortices, we have measured the vortex SH power for different orders of pump vortices, with results shown in Fig. 3.1.3. For this measurement we maintained constant pump power ($P = 3.5$ W) for all orders and focused at the center of the crystal using a lens, $f = 100$ mm. As evident from Fig. 3.1.3, the conversion efficiency decreases with the order of the vortices from a maximum conversion efficiency of 31.2% for $l_p = 0$, Gaussian beam, to as low as 1.44% for pump vortex order $l_p = 6$. Although Eq. (3.1.2) shows dependence of vortex intensity on various parameters, experimentally beam power and area are the two measurable parameters determining the beam intensity. In the experiment, the Gaussian beam power and radius before the SPP are constant. Therefore, the decrease in vortex beam intensity with order can only be attributed to the increase in vortex area with order.

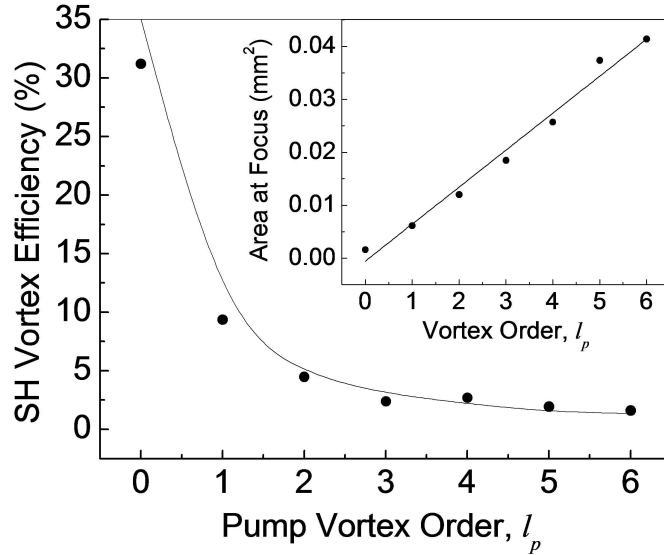


Figure 3.1.3: Variation of vortex SH efficiency with the order of the pump vortex. Solid line is the reciprocal of pump vortex area fitted to the SH efficiency. (Inset): Dependence of vortex area on its order, and linear fit (solid line).

We have measured the area of the vortex beam of different orders at the focus of the lens $f = 100$ mm, with the results shown in the inset of Fig. 3.1.3. The area of the vortex beam increases linearly with the order similar to Ref. [51]. While fitting, we observe a close agreement between vortex SH efficiency and reciprocal of pump vortex area (solid line of Fig. 3.1.3) for all orders. Therefore, the decrease of vortex SH efficiency with order is certainly associated to the decrease of pump vortex intensity with order. Such observation also justifies the order-independent SH vortex efficiency as reported in [49] for the “perfect” vortex, where area does not increase with order.

We also measured the focusing-dependent SH efficiency of the optical vortices. Keeping the input pump at constant power, $P = 3.5$ W, we have measured SH efficiency for $l_p = 0, 1, 2,$ and 3 while changing the beam area at the center of the SHG crystal using a set of lenses, $f = 25, 50, 100, 150, 200,$ and 300 mm. The results are shown in Fig. 3.1.4. Like Gaussian beam, $l_p = 0$, the SH efficiency of the vortices of all orders decreases with longer focal length lenses. Such behavior can be attributed to the decrease of vortex beam intensity due to the increase of beam area at loose focusing. At tighter focusing resulted from

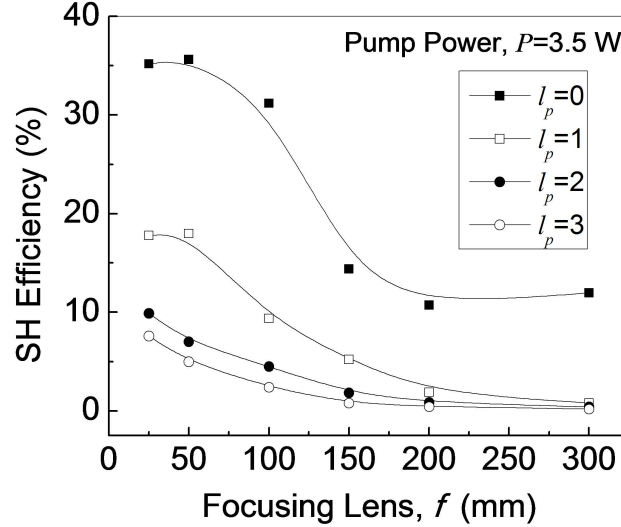


Figure 3.1.4: Focusing-dependent SH efficiency of Gaussian beam and vortex beams of different orders. Lines are guides to eyes.

small focal length lenses ($f = 25$ and 50 mm), the Gaussian beam shows signs of optimum conversion efficiency similar to Ref. [28]. However, optical vortices have increasing SH efficiency with tighter focusing without the sign of optimum focusing. This effect can be attributed to the fact that the increase of vortex area with order demands further tighter focusing to reach optimum focusing condition. Due to the unavailability of lenses of smaller focal length ($f < 25$ mm) in our lab and also the fact of disintegration of higher-order SH vortex beams into single charged vortices at very tight focusing, and longer crystal lengths, we could not reach the optimum focusing condition for vortices.

To characterize the power scalability of the SH vortex source, we measured the SH power and corresponding conversion efficiency up to the maximum available fiber laser power with the results shown in Fig. 3.1.5. We have used a 50 mm long focal length lens to focus the pump vortex of order $l_p = 1$ at the center of the crystal. As evident from Fig. 3.1.5, the vortex SH power and efficiency show quadratic and linear dependence, respectively, to the input vortex power. The maximum SH power is 900 mW at 4.6 W of pump power corresponding to maximum single-pass conversion efficiency as high as $\sim 19.5\%$. However, we do not observe any evidence of saturation effect in the conversion

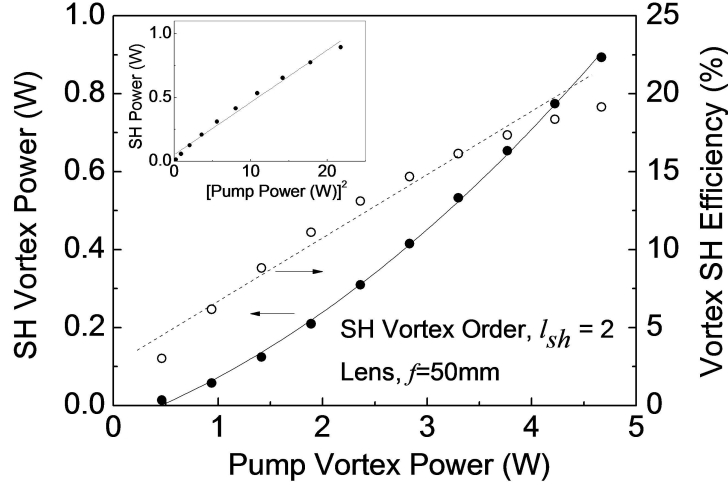


Figure 3.1.5: Variation of SH vortex power and efficiency as a function of the input vortex power. (Inset): Dependence of vortex SH power with the square of pump power. Lines are guide to eyes.

efficiency. The linear dependence of the SH power with square of the pump power (inset of Fig. 3.1.5) clearly indicates the possibility of further increase in SH power with the increase of pump power without any saturation.

We also observe experimentally the effect of vortex beam on angular phase-matching (acceptance) bandwidth of the frequency-doubling process. Using a 1.2 mm long BIBO crystal and focusing lens, $f = 50$ mm, we measured the angular phase-matching bandwidth of vortex ($l_p = 1$) and Gaussian beams, with the results shown in Fig. 3.1.6. As evident from Fig. 3.1.6, the vortex beam has a wider angular acceptance bandwidth ($\Delta\theta_l = 12.6$ mrad) than that of the Gaussian beam ($\Delta\theta_G = 8.6$ mrad). Such broadening in the angular acceptance bandwidth can be attributed to the departure of the beam intensity away from the center of the beam axis in the vortices. However, we did not observe substantial change in the angular acceptance bandwidth with the increasing order of the optical vortices. Under similar focusing, all SH vortex orders have temporal and spectral width around ~ 400 fs and 1.2 nm, respectively, similar to that of the Gaussian beam. Such observation clearly indicates that topological charge of the optical vortices has negligible or no effect in the temporal and spectral properties of the SHG beams.

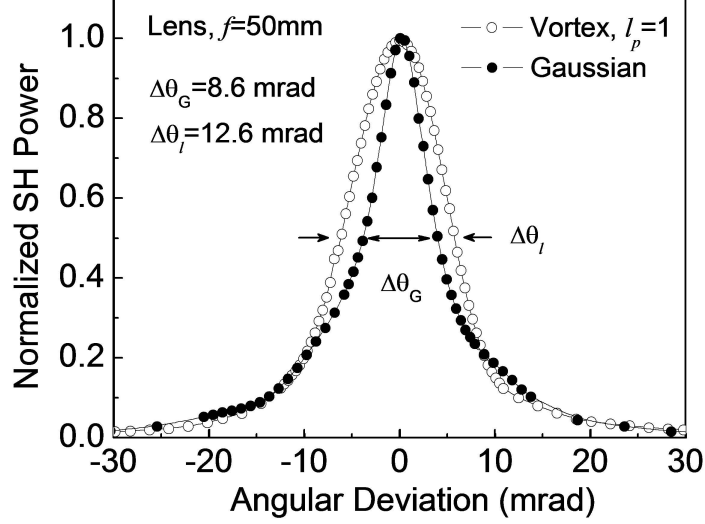


Figure 3.1.6: Angular phase-matching bandwidth of frequency doubling of Gaussian and vortex beams. Lines are guide to eyes.

In conclusion, we have demonstrated frequency doubling characteristics of high-power, ultrafast, optical vortex beams. We also demonstrated a new scheme to generate optical vortices of orders $l_{sh} = 1 - 6$ by using only two SPPs of phase winding 1 and 2. Using single pass SHG we have generated optical vortices up to 12th order with maximum vortex SH power of 900 mW at single-pass conversion efficiency as high as 19.5%. We observed the decrease of vortex SH efficiency with vortex order. Such effect is attributed to the increase of vortex area with order. Like Gaussian beams, vortices also have focusing-dependent SH efficiency. However, at higher orders the optimum focusing is realized at relatively tighter focusing. Additionally, we have also observed that the vortices have higher angular acceptance bandwidth than that of Gaussian beams.

3.2 Generation of optical vortices at 266 nm

3.2.1 Introduction

The optical vortices find variety of scientific, industrial, and medical applications [10, 11]. However, many such applications require vortex beams in the blue, ultraviolet (UV) and deep ultraviolet (DUV) wavelength regions. For example, optical vortices at shorter wavelengths improve the resolution in spectroscopy [52] and give multilateral increase in resolution below the diffraction barrier in fluorescence microscopy [52, 53, 54, 55]. Similarly, optical vortices in the blue-UV wavelength range [56] are essential in the field of quantum optics for entanglement in OAM states of photons [11].

Conventionally, generation of optical vortices rely on the phase modulation of Gaussian beam using SLMs [47] and SPPs [57]. Unfortunately, the low damage threshold of the liquid crystal based SLMs have restricted their use for wavelength above 400 nm. Additionally, the SLM are only useful for lower powers. While SPPs can handle very high laser powers, practical limitations in the fabrication technology have restricted the availability of SPPs to near-UV wavelengths and above. Alternative techniques such as forked shaped diffraction grating [58] and mode converters [59] suffer from common drawback of low output power, high losses and system complexity especially in the DUV wavelength range. Therefore, it is imperative to devise alternative route to generate high power and high order optical vortices in the DUV wavelength range.

Traditionally, DUV wavelengths are accessed through nonlinear frequency conversion such as second-harmonic generation (SHG) and fourth harmonic generation (FHG) of laser of visible and near-IR wavelengths. Therefore, nonlinear frequency conversion of optical vortices at visible and near-IR wavelength can be the most straight forward way for generation of optical vortices at DUV wavelengths. As the efficiency of the nonlinear process for a given laser is critically influenced by different crystal parameters such as effective nonlinear coefficient, spatial walk-off and phase-matching properties, the success in generating high power optical vortices at DUV depends on the selection of proper nonlinear crystal. It is interesting to note that, out of all the prominent nonlinear crystals for DUV generation, $\beta - BaB_2O_4$ (BBO) possess the highest nonlinear coefficient ($d_{eff} = 1.75\text{pm/V}$) with the

short wavelength transparency cut-off extending down to 180 nm making it an excellent material candidate [27].

3.2.2 Experiment

In this section of thesis we present the first experimental demonstration of vortex beams at 266 nm. Implementing a two stage SHG process starting from a picosecond Yb-fiber laser at 1064 nm in Gaussian beam profile we have generated vortex beams of order as high as 12 in DUV at 266 nm. In the first stage, the fundamental laser source at 1064 nm is frequency-doubled in a 30-mm-long LBO crystal producing green. The green beam in Gaussian profile is embedded with the azimuthal phase using SPPs and subsequently frequency doubled in a 10- mm-long BBO crystal to generate vortex beams in DUV wavelength. The generated DUV vortex is measured to have a maximum power of 383 mW centered at 266 nm with a spectral spread of 1.02 nm in the lowest order. Here we present the first experimental generation of vortex beam of order as high as 12 in DUV wavelength range. The schematic of the experimental setup for the generation of DUV vortex beam is shown in Fig. 3.2.1. A picosecond Yb-fiber laser (Fianium, FP1060-20), providing up to 20 W of average power of 20 ps pulses at 78 MHz repetition rate is used as the fundamental laser source. The laser has a spectral width of 1.4 nm centered at 1064 nm. The laser is operated at its full power to achieve its optimum output characteristics and the required output power was adjusted using an attenuator based on a half-wave plate ($\lambda/2$) and polarizing beam splitter cube (PBS). A 30-mm-long, $3 \times 4 \text{ mm}^2$ aperture LBO crystal (C1) is used for SHG of the fundamental laser beam. The SHG stage is similar to the one described previously in [27]. Focusing the fundamental laser beam into the LBO crystal with a measured beam radius of $34 \text{ }\mu\text{m}$ corresponding to a beam focusing parameter [1] of $\xi = 2.74$, we have generated 532 nm radiation as high as 8 W. The generated green beam is collimated using a lens, L2 of focal length 100 mm. A dichroic mirror (S1) separates green beam from the infrared. Using two spiral phase plates, SPP1 and SPP2 having phase winding 1 and 2 respectively, one can in principle generate optical vortices of order up to 3. However, using such two SPPs and a vortex doubler setup, consist of a polarizing beam-splitter cube (PBS2), quarter-wave plate ($\lambda/4$), a plane mirror (M) with high reflectance ($R > 99\%$) for

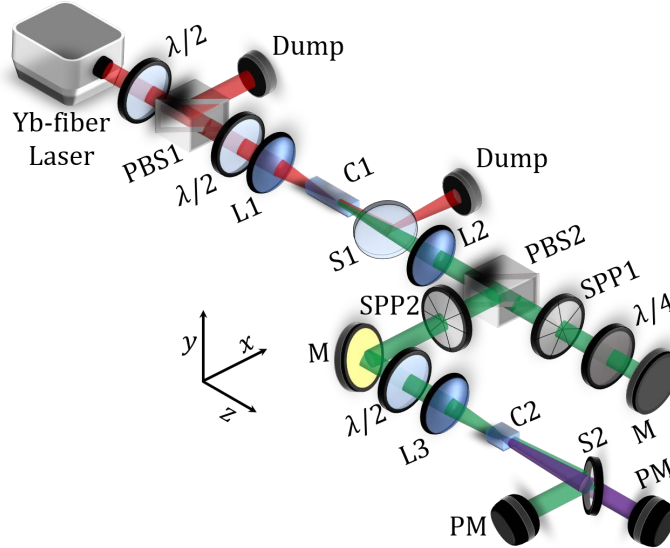


Figure 3.2.1: Schematics of the experimental setup for UV vortex beam. $\lambda/2$; half-wave plate, PBS; polarizing beam splitter cube, SPP1,2; SPPs, $\lambda/4$; quarter-wave plate, M; mirrors, C1-2; Nonlinear crystals for frequency conversion, S1-2; Dichroic mirrors; PM, Power meter.

green, we can generate green vortices up to order, $l = 6$. The working principle of the vortex doubler can be found in Sec.3.1.2. Lens, L3, focuses the green vortex beam into a 10-mm-long BBO crystal (C2) with $4 \times 5 \text{ mm}^2$ aperture for the SHG of green into DUV radiation. The crystal is cut ($\theta = 47.5^\circ, \phi = 90^\circ$) for type-I ($o + o \rightarrow e$) phase-matching of green into DUV. A half wave plate at 532 nm provides correct polarization of the input beam with respect to the crystal orientation for achieving optimum phase-matching. A dichroic mirror (S2) is used to extract DUV radiation from the undepleted green radiation.

3.2.3 Results and discussion

To verify the generation of optical vortices at DUV wavelength, we have recorded the intensity distribution of both the green and DUV beams using a CCD camera with the results shown in Fig. 3.2.2. First column (a)- (c) of Fig. 3.2.2 shows the intensity pattern of the green vortices of order $l = 1, 3$ and 6 respectively. However, to confirm the order of the vortices we have recorded the interference pattern of the vortices with Gaussian beam

resulting characteristic fork fringes of the vortices as shown in the second column. The interference pattern as shown in second column, (d)- (f) of Fig. 3.2.2, confirms the order of the green vortices to be, $l = 1, 3$ and 6 respectively. As the dark core size (low or no light region) of the vortices increases with its order, we observe faint fringes at the centre of the higher order vortices. Although, the green source can produce maximum output power of 8 W, use of vortex double setup and SPPs reduce the overall green power for DUV generation. To find the origin of such losses, we systematically examined loss contribution of all the components used in the double setup. Due to antireflection coating of all components, the overall reflection loss of the setup is negligibly small. However, when the SPPs are placed inside the vortex doubler we found substantial reduction in the output power of the green vortex beam. To put in perspective, for green beam of power ~ 7 W the vortex doubler containing both the SPPs produces green vortex beam of order $l = 6$ with power of ~ 6 W corresponding to a 15% loss. A careful observation reveals that the SPPs in addition to the phase modulation also modulates the polarization of the input beam. Such depolarization effect can be attributed to the manufacturing defect in the SPPs. Third column, (g)- (i) of Fig. 3.2.2 shows the intensity distribution of the DUV beams generated from the green vortices of order, $l = 1, 3$ and 6 respectively. Unlike green vortices generated using SPPs and also through nonlinear interaction [57], here the nonlinear generation of DUV vortices have asymmetric intensity distribution. Further the vortex quality deteriorates with order. Such asymmetry in the DUV vortices can be attributed to high spatial walk-off effect arising from the high birefringence ($\rho \sim 85.33$ mrad) and longer interaction length (10-mm) of the BBO crystal. One can in principle improve the vortex quality with the use of loose focusing, however, at the cost of low vortex power given that the parametric gain of the vortices are smaller than that of Gaussian beam and further reduces with the order of the vortices. On the other hand, use of alternative nonlinear crystal with improved birefringence property at such difficult wavelength range is beyond question. Due to unavailability of suitable reference beam at 266 nm, we could not record characteristic fork pattern of the DUV vortices. Alternatively, we have used tilted lens technique [47] where the vortex beam while passing through the titled lens splits into bright lobes. The number of bright lobes for vortex of order l is equal to $|l| + 1$. Fourth column (j)- (l) of Fig. 3.2.2 shows lobe structure of the DUV vortex after passing through the tilted lens. Counting the number of

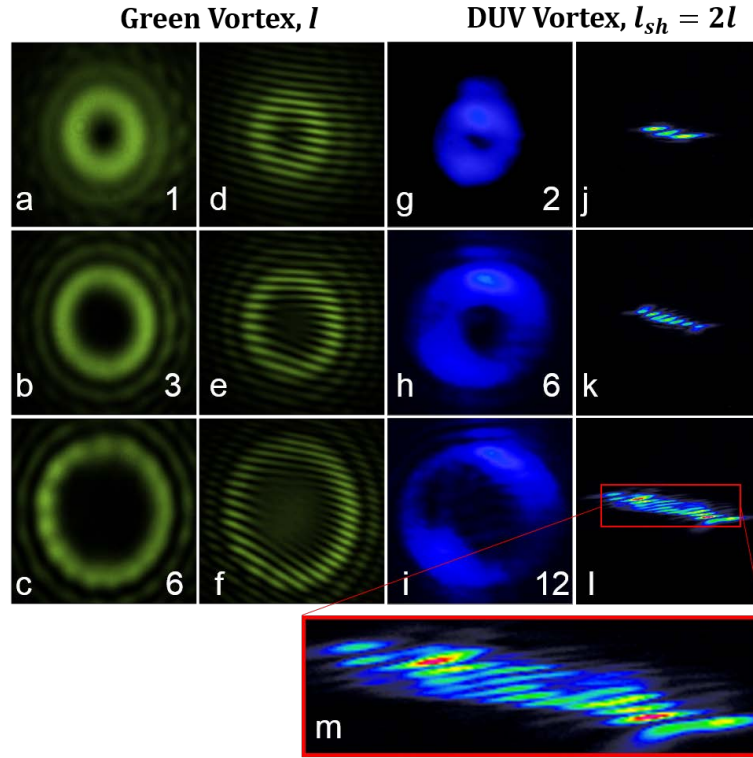


Figure 3.2.2: The intensity profile of the green vortex beam and UV. (a-c) Vortex beam of order 1, 3 and 6 generated using SPPs. (d-f) Corresponding interference pattern showing ‘fork pattern’. (g-i) Intensity profile of the generated UV vortex beam of order 2, 6 and 12 (j-l) corresponding images obtained after passing through tilted lens showing $|l_{sh} + 1|$ lobes.

bright lobes of Fig. 3.2.2(j)- (l), we can confirm the order of the DUV vortices to be 2, 6 and 12 respectively, double the order of the green vortices owing to the conservation of OAM in nonlinear process. Fig. 3.2.2 (m) shows the magnified image of the Fig. 3.2.2(l).

After confirmation of optical vortices at DUV wavelength, we have studied the variation of DUV vortex power as a function vortex order of the green beam with the results shown in Fig. 3.2.3. Focusing the green beam of constant power ~ 4.7 W at the centre of the BBO crystal using a lens of focal length, $f = 175$ mm, we recorded the DUV power while changing vortex order of the green beam from $l = 0$ (Gaussian beam) to $l = 5$. As evident from the Fig. 3.2.3, the DUV vortex power falls steeply with increase of vortex order of the green beam from the maximum DUV power of 600 mW available for Gaussian spatial

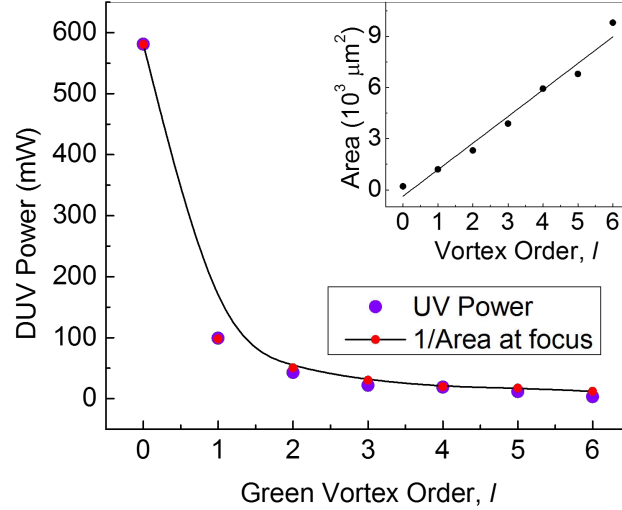


Figure 3.2.3: Variation of UV power with order of the input green vortex beam. (Inset) Area as a function of vortex order. Solid line for the guide to eyes.

distribution ($l = 0$). In our recent work [57] we have attributed the decrease of second-harmonic (SH) vortex power with the order of the fundamental vortices to the increase of vortex area with its order. To verify such findings [57] and also to get further insight of the decrease of DUV power with vortex order, we have measured the intensity profile of the green vortices of orders $l = 1 - 6$ at the focus of the lens L3. From these intensity profiles we have calculated the area of the green vortices at the centre of the crystal with the results shown in inset of Fig. 3.2.3. As expected, the area of the vortex beams increases linearly with its order. Therefore, for a constant power, the intensity of the green beam driving the SHG process decreases with the increase of vortex order, thus decreasing DUV power with the vortex order. To justify such observation, we further fitted the experimental data of DUV power (purple dots) in Fig. 3.2.3 with the reciprocal of the vortex area (red dots) for different orders. As evident from Fig. 3.2.3, for all orders, the DUV power exactly matches with the reciprocal area of the corresponding green vortex. Since the integer vortices used in the current study have discrete areas, and it is difficult to predict the area of the vortex (fractional) between any two integer vortices, in Fig. 3.2.3 we did not fit data points (DUV power) with solid line. However, we have added the solid line to guide eyes.

Given that the area of the vortex beam increases with its order, one can in principle think of using tighter focusing with the order to generate higher DUV power. However such a proposal necessarily need not give desired result because the divergence of the vortices of wavelength λ as represented by the formula, $d_l = w_o r_l / Z_R = \lambda r_l / \pi w_o$ [59] increases due to both vortex order and tight focusing influencing the effective interaction length of the nonlinear crystal. Here, d_l and r_l are the divergence and inner or outer radius of the vortex of order, l . $w_0 (= 2f/kw_g)$ [60] is the Gaussian beam waist at the focus of the lens of focal length, f . w_g is the beam waist radius of the Gaussian beam confining the vortices, k and Z_R the wave vector and Rayleigh range respectively. Therefore, for a given crystal and laser parameters, it is expected to have an optimum focusing condition producing highest SHG power for vortices of all orders. To ascertain the dependence of DUV power on focusing for different vortex orders, we have measured the DUV power while focusing the green beam of different orders with a set of lenses with the results shown in Fig. 3.2.4. Maintaining constant green power (~ 6.8 W), we focused the green vortices of order $l = 1, 2$ and 3 using a set of 5 lenses of focal lengths, $f = 500, 300, 200, 175, 100$ and 75 mm. As evident from Fig. 3.2.4, under loose focusing ($f = 500$ mm), the DUV vortex powers are measured to be 125, 24, 7 mW for input vortex of orders, $l = 1, 2$ and 3 respectively and increase with tighter focusing. In case of green vortex of order $l = 1$, the DUV power varies from 125 mW to 260 mW with tighter focusing using lenses of $f = 500$ mm to 75 mm with a maximum DUV power of 307 mW at $f = 175$ mm. With similar variation in the focal length of the lenses, the DUV power for green vortex of orders $l = 2$ and 3 varies up to 156 and 78 mW respectively with maximum power of 170 and 87 mW for $f = 100$ mm lens. Decrease of maximum DUV power with the order of the green vortex of constant power also confirms the increase of vortex area with order. As a results, the optimum focusing is achieved using lower focal length lens for higher order vortices. To compare the focusing dependent DUV power for optical vortices to that of the Gaussian beam, we have reproduce the results of Ref. [27] in the inset of Fig. 3.2.4. As evident from Fig. 3.2.4, the vortex beam of all orders have similar focusing dependent DUV power as that of Gaussian beam. Therefore, for a given length of nonlinear crystal, one can expect optimum focusing condition for different structured beams.

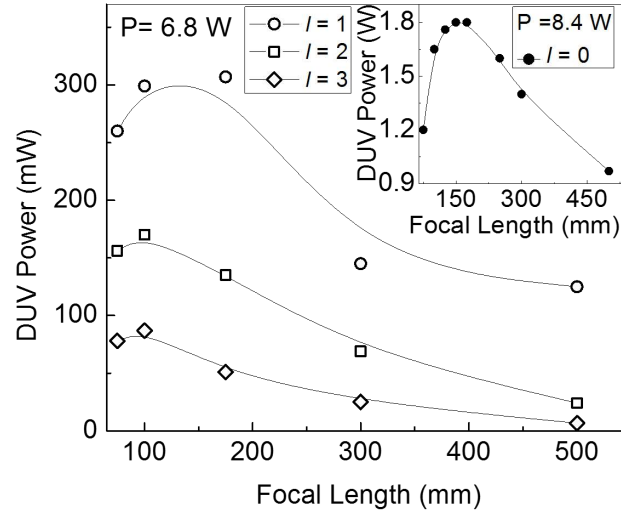


Figure 3.2.4: Dependence of DUV vortex power for green vortex of order $l = 1, 2$ and 3 on the focal length of the lens. (Inset) Gaussian DUV power variation as a function of focal length of the lens.

Knowing the optimum focusing condition we studied the power scaling properties of the DUV source. We focused the green vortex of order $l = 1$ to its optimum vortex size at the centre of the BBO crystal with lens of focal length $f = 175$ mm and measured the DUV power and single-pass green-to-DUV conversion efficiency with the green vortex power with the results shown in Fig. 3.2.5. As evident from Fig. 3.2.5, the DUV power (solid circles) and efficiency (open circle) increases quadratically (solid line) and linearly (dotted line) respectively with the increase of green vortex power resulting a maximum DUV power of 383 mW at green power of 7.39 W, and maximum single-pass green-to-DUV conversion efficiency of 5.2 %. In order to confirm the quadratic dependence of DUV power with the green power we plotted the DUV power with square of the green power in the inset of Fig. 3.2.5. As expected the DUV power increases linearly with the square of green power (see inset of Fig. 3.2.5) without any sign of saturation or roll-off effects clearly indicate the possibility of further enhancement in DUV power and efficiency with the increase of green power and nonlinear crystals with high nonlinear coefficient.

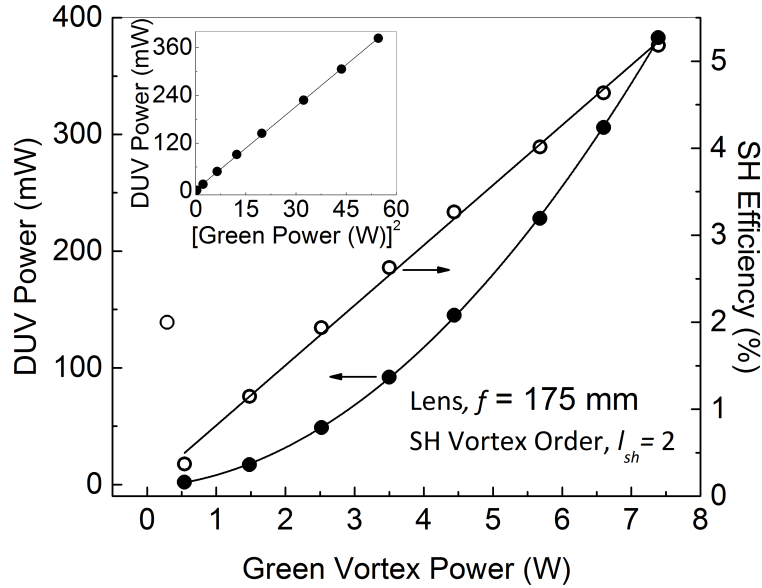


Figure 3.2.5: Variation of DUV power as a function of green vortex ($l = 1$) power. (Inset) Dependence of DUV power with the square of the green power. Lines are guide to eyes.

We also studied the effect of angular acceptance bandwidth of the BBO crystal on the vortex order for single-pass DUV vortex generation. The results are shown in Fig. 3.2.6. Using a lens of focal length, $f = 175$ mm at a constant green power of 1.2 W, we measured the DUV power while performing angular interrogation about the phase-matching plane. The BBO crystal is cut such that the exact phase-matching takes place for normal incidence. Therefore, the Gaussian fundamental beam produces maximum SH power at normal incidence and characteristic sinc^2 power distribution (black dots in Fig. 3.2.5) with the tilt of the crystal away from the normal incidence. The full-width at half maxima of the sinc^2 function is determined by the length, and dispersion of the crystal and also the spectral width of the laser. On contrary, as evident from Fig. 3.2.5, the vortex beams of all orders have low SH power at exact phase-matching (dotted line). The SH power initially increases with the tilt of the crystal, however, with further tilt of the crystal away from the normal incidence, the SH power decreases resulting a double-peaked SH power distribution. The separation between the double peak increases with the order of the fundamental vortex. To understand such effect we have recorded the intensity profile of the generated DUV vortex beam with the crystal tilt. For exact phase-matching (dashed line

in Fig. 3.2.6), the generated vortex beam have a symmetric intensity distribution, however, with the tilt of the crystal the DUV vortices show asymmetric structure with higher intensity in the tilt direction. At the crystal tilt corresponding to maximum DUV power, the vortex loose its characteristic doughnut structure resulting arched shaped intensity distribution with high intensity at the tilt direction. Flip in tilt direction also flips the position of this high intensity arch.

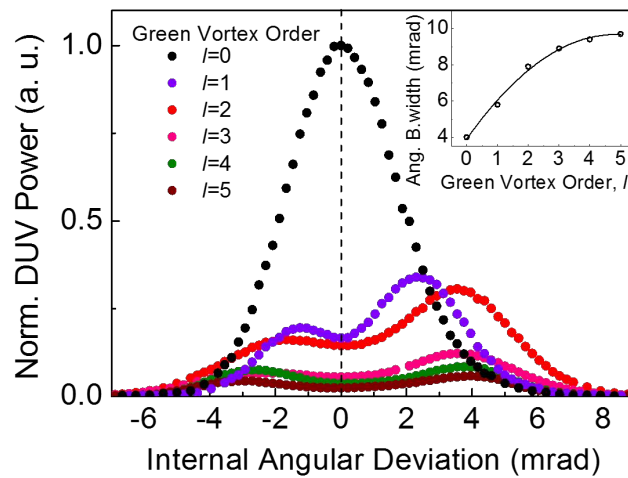


Figure 3.2.6: Dependence angular acceptance bandwidth of BBO crystal on the order of the input vortex. (Inset) Variation of angular acceptance bandwidth with order.

These observations can be explained as follows. Unlike Gaussian beam having maximum intensity at the centre of the beam, the maximum intensity of the doughnut shaped vortex beam appears at its annular rim. As a result, for focused vortex beam, different parts of the beam make different angles with the optic axis of the crystal. In addition, the vortices have higher divergence than that of Gaussian beam. Therefore, when the vortex beam is phase-matched keeping the crystal at its exact phase-matching angle, all parts of the vortex beams makes same angle with the optic axis of the crystal resulting a symmetric SH vortex beam. However, due to beam divergence, part of the intensity ring falls outside the phase-matching bandwidth of the crystal resulting lower DUV power. On the other hand, the increase in DUV power and asymmetry in the vortex beam can be attributed to the fact that with crystal tilt away from exact phase-matching, one part of the beam (at the tilt direction)

makes exact phase-matching and high conversion than the other side of the beam. However, further increase in the crystal tilt results lower DUV conversion as the beam drifts out of the phase-matching angle. The asymmetry in the power of the two lobes can be attributed to the spatial walk-off of the crystal. We have recorded the angular acceptance bandwidth of the BBO crystal with the order of the green vortex with the results shown in the inset of Fig. 3.2.6. As evident from the inset of Fig. 3.2.6, the angular phase-matching bandwidth of the 10-mm-long BBO crystal increases with the order of the green vortex from 4 mrad at $l = 0$ (Gaussian beam) to 8.9 mrad for $l = 3$. However, with further increase in vortex order, the phase-matching bandwidth remains almost constant. Such effect can be attributed to the increase in beam divergence with order of the vortex beam due to which the effective length of the crystal for the nonlinear interaction decreases, thereby increasing the angular acceptance bandwidth for higher orders. Such explanation also supports the decrease of DUV power with the order of the green vortices. The present study also proves that the angular phase-matching bandwidth depends on the spatial structure of the input beam. We studied the spectral characteristics of the generated UV vortex beam and its power stability. Using a CCD based spectrometer (resolution ~ 0.5 nm) we measured the spectral width of the DUV radiation to be ~ 1.02 nm centered at 266 nm. Under free running condition, the DUV source exhibits a power stability better than 1.2 % rms over 1.5 hours.

In conclusion, we have generated vortex beam of order as high as 12 in the DUV wavelength range with a maximum output power of 383 mW at a single-pass green to DUV efficiency of 5.2%. For a given laser and crystal parameters, the optical vortices of different orders have different optimum focusing condition providing maximum DUV power. We also experimentally observed the influence of the spatial structure of the fundamental beam on the angular phase-matching bandwidth of the nonlinear crystal. The angular acceptance bandwidth of the BBO crystal increases with the order of the fundamental vortex.

Chapter 4

Nonlinear generation of high power 'perfect' vortex beam

This chapter constitutes the following journal publications:

1. *Efficient nonlinear generation of high power, higher order, ultrafast “perfect” vortices in green,*
Apurv Chaitanya N, M. V. Jabir and G. K. Samanta,
Optics Letters 41, 1348 (2016)

4.1 Efficient nonlinear generation of high power, higher order, ultrafast “perfect” vortices in green

4.1.1 Introduction

Optical vortices, having phase singularities (phase dislocations) in the wave-front, carry vanishing intensity at the singular point. Due to the screw-like (helical) phase structure around the point of singularity, such beams carry OAM. The phase distribution of the optical vortices can be represented as $\exp(il\theta)$, with θ as azimuthal angle and the integer l , the

topological charge (order). Each photon of the beam carries OAM of $l\hbar$. Since the discovery of OAM associated with optical vortices [4], these beams have drawn a great deal of attention from various fields of science and technology including high resolution microscopy [41], quantum information [11], material processing [42] and particle micro-manipulation and lithography [10]. However, the major challenge through these applications is the need for sources of coherent radiation in vortex spatial profiles at different topological charges and wavelengths.

The optical vortices are typically generated by spatial phase modulation of Gaussian beams using different types of modulators including SLMs and SPPs. However, all of those modulators have its own advantages and disadvantages in terms of wavelength coverage, mode conversion efficiency, damage threshold and power handling capabilities and cost [57]. On the other hand, nonlinear frequency conversion techniques can be used to access high power/energy optical vortices at different wavelengths across the electromagnetic spectrum inaccessible to lasers. As such, frequency up-conversion of high power, ultrafast, optical vortices at $1.064 \mu\text{m}$ has given access to higher order optical vortices ($l = 12$) in the green at $0.532 \mu\text{m}$ [57]. Similarly, frequency downconversion in optical parametric oscillators has produced optical vortex beam of order, $l = 1$, with spectral tunability across $1 \mu\text{m}$ [61] and $2 \mu\text{m}$ [62]. So far, the nonlinear generation of vortex beams with high power/energy has been restricted to the vortices of lower orders [57]. In case of optical vortices, the beam area and divergence [60] increases linearly with the order of the vortices. As a result, the nonlinear parametric gain, which depends on the intensity of the driving fields and the overlapping integral of the interacting beams, and thus the conversion efficiency of the nonlinear processes decreases with the order of the vortices. Therefore, nonlinear generation of higher order optical vortices especially with high power/energy requires optical vortices with beam area and beam divergence independent to their orders. Fortunately, recent development in the field of structured beams provided a new class of optical vortex beams known as "perfect" vortex [63]. Unlike vortices, the "perfect" vortices have annular ring radius independent of its orders.

Typically, Fourier transformation of the Bessel-Gauss (BG) beam of different orders is used to generate "perfect" vortices [63]. However, the combination of SPP and axicon converting the Gaussian beam into Laguerre - Gaussian (LG) beams and BG beams of

different orders, as presented in here, can be considered as one of the simplest schemes for generating high power "perfect" vortices of different orders. The complex field amplitude of the experimentally realizable "perfect" vortex of order l at the back focal plane ($z = 0$) of the Fourier transforming lens may be represented in polar coordinates as [63]

$$E(\rho, \theta) = i^{l-1} \frac{w_g}{w_0} \exp\left(-\frac{(\rho - \rho_r)^2}{w_0^2}\right) \exp(il\theta) \quad (4.1.1)$$

Here, w_g is the waist radius of the Gaussian beam confining the vortex beam. $\rho_r = f \sin(n-1)\alpha$ is the radius of the "perfect" vortex ring, f is the focal length of the Fourier transforming lens, and n and α are respectively the refractive index and base angle of the axicon. w_o ($w_o = 2f/kw_g$), the Gaussian beam waist radius at the focus also corresponds to the annular width of the "perfect" vortex. $k = 2\pi/\lambda$ is the wave vector of the beam of wavelength λ in free space. Using Eqn. (4.1.1), we can write the intensity of the "perfect" vortex as,

$$I = \left(\frac{w_g}{w_0}\right)^2 \exp\left(-2\frac{(\rho - \rho_r)^2}{w_0^2}\right) \quad (4.1.2)$$

As evident from the Eqn. (4.1.2), the intensity of the "perfect" vortex is independent of its order. Therefore, one can expect the nonlinear frequency conversion efficiency of such "perfect" vortices to be independent of their orders [49]. Using such "perfect" vortices, here we present, the first experimental demonstration of nonlinear generation of "perfect" vortices of power > 1.2 W at green with conversion efficiency as high as 27 % and topological charge (order) as high as 12. We have also experimentally verified that at high power regime, the conversion efficiency of "perfect" vortices is independent to its order.

4.1.2 Experiment

The schematic of the experimental set up is shown in Fig.1. An ultrafast Yb-fiber laser at 1060 nm similar to Ref. [57] producing output in Gaussian (Fig. 4.1.1(a)) intensity distribution ($M^2 < 1.1$) is used as the pump source. The laser output has temporal and spectral width of 260 fs and 15 nm respectively at a repetition rate of 78 MHz. The input power to the nonlinear crystal is controlled using a half wave plate ($\lambda/2$) and polarizing beam splitter cube (PBS1). Using only two spiral phase plates, SPP1 and SPP2, of winding

numbers 1 and 2 respectively and a vortex – doubler [57] comprising of PBS2, quarter wave plate ($\lambda/4$) and a plane mirror (M) with high reflectance for 1060 nm, we have generated optical vortices of order $l_p = 1 - 6$. The intensity profile of the generated vortex beam ($l_p = 2$) is given in Fig. 4.1.1(b). The antireflection (AR) coated axicon of apex angle 178° , converts vortex beam (LG beam) into BG beam (see Fig. 4.1.1 (c)) of same order. A Plano-convex lens, L1, of focal length, $f_1 = 25$ mm Fourier transforms the BG beam into "perfect" vortices. The imaging system comprising two Plano-convex lenses L2 and L3 with focal lengths $f_2 = 200$ mm and $f_3 = 50$ mm respectively, images the "perfect" vortex (see Fig. 4.1.1(d)) at the centre of the nonlinear crystal to a measured beam radius of 166 mm. A 5-mm-long and 2×1 mm² in aperture, MgO-doped, periodically poled congruent LiNbO₃ (MgO:CLN) crystal (C) with linear chirped grating period of 6.61-6.91 μm is used for SHG of the pump vortex beam. The crystal has spectral acceptance bandwidth of 15 nm to cover entire pump spectrum and phase-matching temperature of 130°C to avoid any detrimental photorefractive effect. Both the faces of the crystal is AR coated for 530 and 1060 nm. The crystal is housed in an oven whose temperature can be varied up to 200°C in steps of 0.1°C . A $\lambda/2$ is placed before the axicon to adjust the polarization of the input beam to the nonlinear crystal. The dichroic mirror, S, separates the fundamental from the second harmonic.

4.1.3 Results and discussion

We have recorded the spatial intensity distribution of the pump beam and frequency-doubled green beam using a CCD based beam profiler (SP-620U, Ophir) at different position along the propagation direction with the results shown in Fig. 4.1.2. First column, (a)- (c) of Fig. 4.1.2 shows the intensity profile of the pump vortices of order, $l_p = 1, 3$ and 6 respectively measured before the axicon. As expected, the annular ring radius of the vortices in the first column increases with the order. The axicon converts the vortices (LG beams) into BG beams of same order, however, the BG beams maintain its structure over a distance, $z_{max} = w_{LG}/(n-1)\alpha$, where w_{LG} is the beam radius of the LG beam before the axicon and n and α are the refractive index and base angle of the axicon respectively. In our experiment, the z_{max} for input vortex order $l_p = 1$ is measured to be 16 cm. The size of

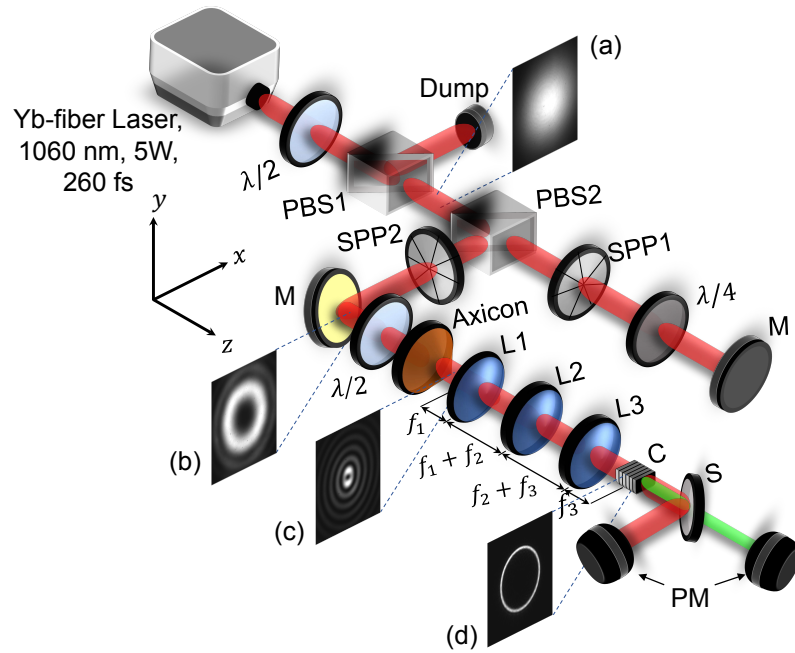


Figure 4.1.1: Schematic of the experimental setup for nonlinear generation of ultrafast "perfect" vortices. $\lambda/2$; half-wave plate, PBS1,2; polarizing beam splitter cube, SPP1,2; SPPs, $\lambda/4$; quarter-wave plate, L1-3; lens, M; mirrors, C; MgO:CLN crystal for frequency-doubling, S; Dichroic mirror; PM, Power meter. (a-d) Spatial intensity profile of the beams recorded at different positions along the propagation direction.

the BG beam of order 1, 3 and 6 as shown in second column of Fig. 4.1.2 (d)- (f) respectively, measured at a distance $z_{max}/2$ from the axicon, increases with the order of input LG beam. Depending upon the order of the input vortices, the Fourier transforming lens L1 is placed at a distance of 15.5 cm from the axicon produces "perfect" vortices at the Fourier plane. The third column, (g)- (i) of Fig. 4.1.2, shows the annular intensity distribution of the "perfect" vortices of orders $l_p = 1, 3$ and 6 respectively measured at the crystal plane. From the intensity profiles of third column, it is evident that the annular ring radius of the "perfect" vortices are independent to their order. Given the intensity distribution of the "perfect" vortices, it is difficult to use interferometric technique to determine its topological charge (order). Therefore, we used tilted-lens technique [47] where, the "perfect" vortex of order l while passing through the titled Plano-convex lens (tilted about y axis at an angle 6°) splits into $n = |l| + 1$ number of bright lobes at the focal plane of the lens. From the number of bright lobes as shown in fourth column, (j)- (l) of Fig. 4.1.2, it is evident that the pump "perfect" vortices have orders $l_p = 1, 3$ and 6 respectively. Fifth column, (m)- (o) of Fig. 4.1.2, represents the intensity distribution of the frequency-doubled "perfect" vortices recorded at the far field (distance > 2 m away from the crystal). Using tilted-lens technique we have confirmed the orders of the SH vortices as shown in the sixth column, (p)- (r) of Fig. 4.1.2, to be 2, 6 and 12 respectively, twice the order of the pump vortices. Such observation validates the angular momentum conservation in frequency-doubling process of "perfect" vortices. The independence of annular ring radius of the second-harmonic (SH) vortices shown in fifth column, on the orders of the pump vortices, proves nonlinear generation of "perfect" vortices at green wavelength. Unlike disintegration of higher order vortices in birefringent crystal [57], use of quasi-phase-matching enables generation of high quality "perfect" vortices (see fifth column of Fig. 4.1.2) even at higher orders.

We have measured the annular ring radius of the pump and SH vortices for all orders with the results shown in Fig. 4.1.3. The "perfect" vortices at fundamental wavelength is produced at the Fourier plane of the lens L1 with measured annular ring radius of $650 \mu\text{m}$. However, to avoid mechanical constrain in accessing these "perfect" vortices and also to tightly focus the "perfect" vortices for efficient nonlinear interaction, we have imaged the pump "perfect" vortices using lenses L2 and L3 in $2f_2 - 2f_3$ configuration (magnification factor of 0.25) at the crystal plane situated at a distance of 500 mm away from the Fourier

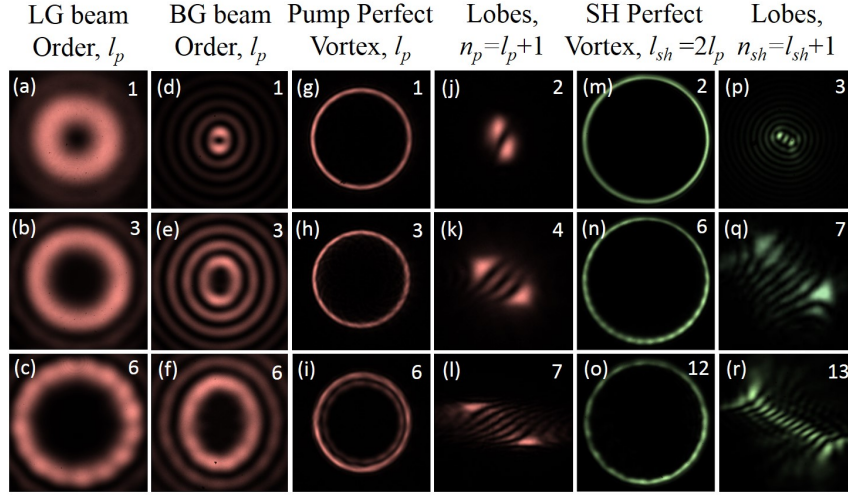


Figure 4.1.2: Spatial intensity distribution of the beams recorded at different positions along beam propagation. (a-c) normal vortex pump beams of orders 1, 3 and 6 recorded before the axicon, corresponding (d-f) Bessel-Gauss beam recorded at 13 cm after the axicon, and (g-i) "perfect" vortices at the Fourier plane of lens L1. (j-l) characteristic lobe structure of the pump "perfect" vortices. (m-o) far field intensity distribution of the SH "perfect" vortices of orders 2, 6 and 12 and (p-r) corresponding lobe structures.

plane of lens L1. As evident from the Fig. 4.1.3 (a), the pump "perfect" vortices have annular ring radius of $\rho_p' = 166 \pm 6$ mm for orders, $l_p = 1 - 6$. The error in the ring radius is comparable to the pixel size ($4.46 \mu\text{m}$) of the CCD camera used to record the vortices. Pumping the nonlinear crystal with the "perfect" vortices, the generated SH beam is imaged at the far field (> 2 m away from the crystal) using a lens of focal length $f = 750$ mm. The variation of annular ring radius of the SH vortices with its order is shown in Fig. 4.1.3(b). As evident from Fig. 4.1.3(b), the SH vortices have annular ring radius $r_{sh} = 420 \pm 12$ mm for the orders, $l_{sh} = 2 - 12$ confirming nonlinear generation of "perfect" vortices at green wavelength. The small variation in the radius of the SH vortices can be attributed mainly to the exact positioning of the CCD camera in the image plane.

From Eqn. (4.1.2) it is evident that the intensity of the "perfect" vortex is independent of its order. Therefore, the SH efficiency which is proportional to the intensity of the input beam should be constant with the order of the input vortices. To verify the order independent SH efficiency of the ultrafast, high power "perfect" vortices, we pumped the nonlinear crystal with "perfect" vortices of power 2.8 W and measured the SH power for

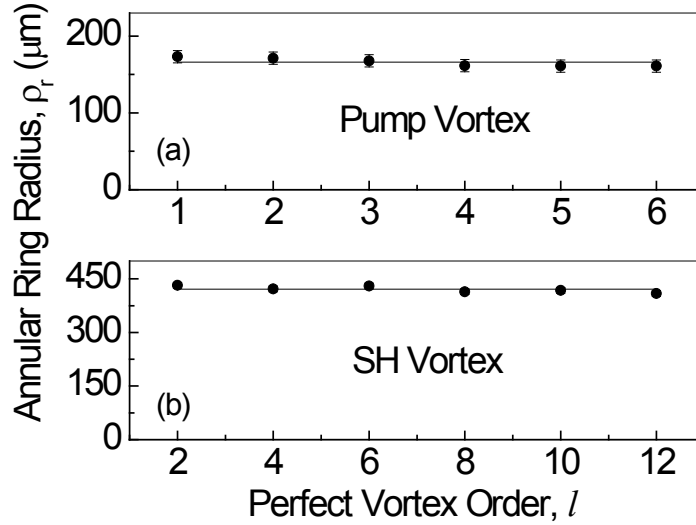


Figure 4.1.3: Variation in ring radius of the annular intensity distribution of "perfect" vortices with its order at (a) pump and (b) SH wavelengths. The solid lines are linear fit to the experimental data.

different vortex orders with the results shown in Fig. 4.1.4. Although the fiber laser can produce output power up to 5 W, due to losses in the vortex –doubler setup, the higher order vortices ($l_p > 3$) have maximum power of 2.8 W. As evident from Fig. 4.1.4, the "perfect" vortices have single-pass SH efficiency of 25% for all orders $l_p = 1$ to 6. We have also measured the variation of SH power with pump power of the "perfect" vortices of orders, $l_p = 1$ and 3 with the results shown in the inset of Fig. 4.1.4. For both orders, as evident from the inset of Fig. 4.1.4, the SH power increases linearly with the pump power at same slope efficiency, $\eta \sim 29.7\%$. The SH "perfect" vortices have maximum output power of 1.2 W for the pump power of 4.4 W resulting a maximum single-pass vortex frequency-doubling efficiency of 27%. This can be considered as the highest single-pass SHG efficiency of optical beam other than Gaussian beam. Unlike quadratic dependence of SH power to the pump powers, the linear increase of SH vortex power with the pump vortex power (see inset of Fig. 4.1.4), clearly indicates the saturation effect in the single-pass SH efficiency.

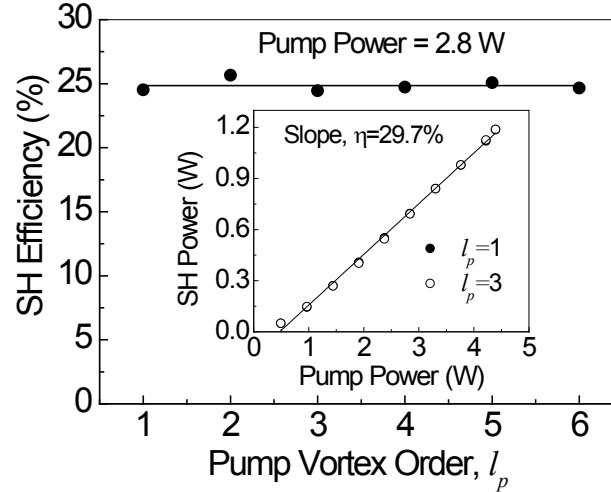


Figure 4.1.4: Dependence of vortex SH efficiency with the order of the pump vortex. (Inset) variation of SH vortex power with the pump vortex power for two different orders, $l_p = 1$ and 3. Lines are linear fit to the experimental data.

To get further insight of the saturation effect, we have investigated the power scaling characteristics of the green "perfect" vortex source. Using the pump vortex of order $l_p = 3$ with annular ring radius of $166 \mu\text{m}$, we have measured the SH power as a function of pump power. The results are shown in Fig. 4.1.5. As evident from Fig. 4.1.5, at lower pump power ($< 2.8 \text{ W}$), the SH power and efficiency show respectively quadratic and linearly dependence to the pump power. However, at pump power $> 2.8 \text{ W}$, the SH power increases linearly with the pump power and the SH conversion efficiency remains almost constant in the range of 25-27 % clearly indicating the saturation effect in the vortex SH process. The deviation of SH power from its linear dependence with the square of the pump power as shown in the inset of Fig. 4.1.5, confirms the saturation effect in the vortex SHG process. Such saturation effect can be attributed to the high nonlinear parametric gain arising from high nonlinear coefficient and long interaction of the MgO:CLN crystal, and also due to the high peak power of the ultrafast pump pulses. While one can expect higher SH vortex power ($> 1.2 \text{ W}$) for pump vortices of smaller annular ring radius and/or higher pump power $> 4.4 \text{ W}$, however, due to low damage threshold of the PPLN crystal [64], especially at the

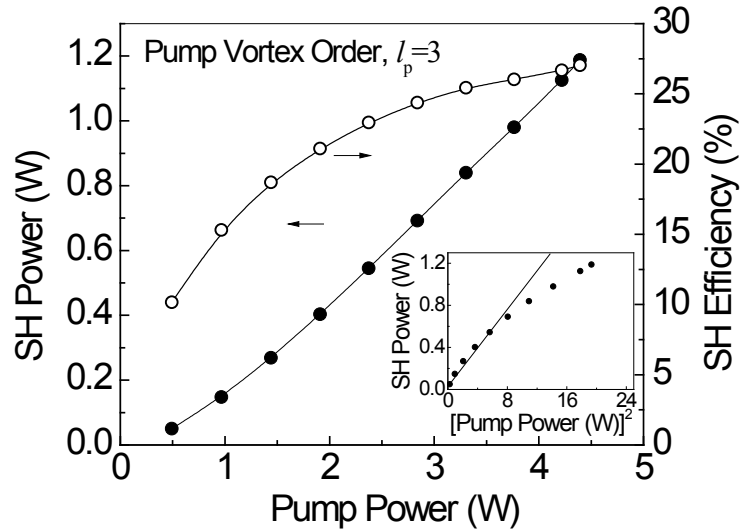


Figure 4.1.5: Variation of SH vortex power and efficiency as function of pump vortex power. (Inset) Dependence of SH power with the square of the pump power. Lines are guide to eyes.

green wavelengths, we have observed crystal damage for pump power beyond 4.4 W and pump vortex radius below $166 \mu\text{m}$.

To study the temperature dependent phase-matching characteristics of the MgO:CLN crystal, we pumped the crystal with "perfect" vortex ($l_p = 3$) of power 1 W and measured the SH power while adjusting the crystal temperature with the results shown in Fig. 4.1.6. As evident from Fig. 4.1.6, the SH power increases with the increase of crystal temperature from 50 to 200°C with highest SH power at $T = 142^\circ\text{C}$ and a measured temperature acceptance bandwidth (full-width at half-maxima, FWHM) of $\Delta T = 110^\circ\text{C}$. As a result, the power of the SH vortices is insensitive to the fluctuation in the ambient temperature and also the instability of the temperature oven used to maintain the crystal temperature. Using a CCD based spectrometer and an intensity auto-correlator we have measured the spectral and temporal width (FWHM) of the SH vortex of all orders to be 1.9 nm centered at 530 nm and 507 fs respectively resulting a time-bandwidth product of 1.02 . Similar to the Ref. [57], here we did not observe any variation in the spectral and temporal width of the SH vortices with the order.

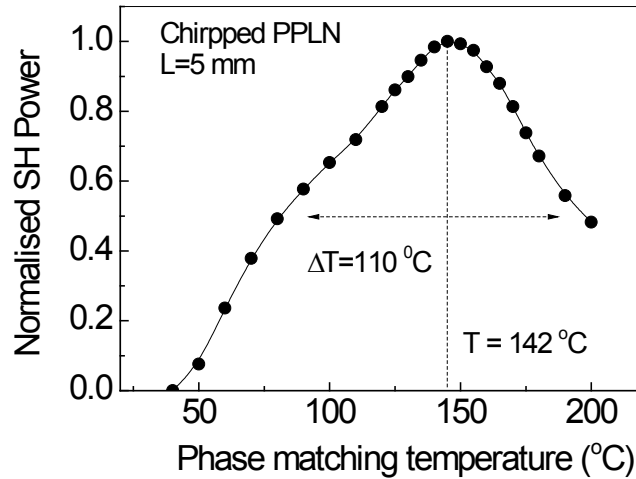


Figure 4.1.6: Dependence of SH power on crystal temperature while pumped with "perfect" vortex of order $l_p = 1$ for a 5 mm long Chirped PPLN.

In conclusion, we have experimentally demonstrated the efficient nonlinear generation of high power, higher order, ultrafast "perfect" vortices at the green with output power > 1.2 W and vortex order up to $l_{sh} = 12$ at single-pass conversion efficiency of 27%. This is the highest efficiency in the single-pass SHG of any structured beam. Similar scheme can be used to generate higher order, high efficient vortices at other wavelengths.

Chapter 5

Hollow Gaussian beam generation through nonlinear interaction of photons with orbital-angular-momentum

This chapter constitutes the following journal publications:

1. *Hollow Gaussian beam generation through nonlinear interaction of photons with orbital-angular-momentum*,
Apurv Chaitanya N, M. V. Jabir, J. Banerji and G. K. Samanta,
Scientific Reports (Under Revision).

5.1 Nonlinear generation of hollow Gaussian beam

Hollow Gaussian beams (HGB) [65, 5] are a special class of doughnut shaped beams that do not carry OAM. Such beams have wide range of applications in variety of fields including atom optics [66, 67, 68, 69], bio-photonics [70], atmospheric science [71, 72], and plasma physics [73, 74, 75]. Till date, these beams have been generated [76, 77, 78, 79, 80] using linear optical elements. Here, we show a new way of generating HGBs by three-wave mixing in a nonlinear crystal. Based on nonlinear interaction of photons having OAM and conservation of OAM in nonlinear processes, we experimentally generated ultrafast HGBs

of order as high as 6 and power >180 mW at 355 nm. This generic concept can be extended to any wavelength, timescales (continuous-wave and ultrafast) and any orders. We show, contrary to common belief [81], that the removal of azimuthal phase of vortices does not produce Gaussian beam. We also propose a new and only method to characterize the order of the HGBs.

The dark hollow beams (DHB) are identified with their characteristic doughnut intensity distribution, a dark center enclosed by a bright ring in the beam cross section. Like conventional DHBs such as optical vortices [4], higher order Bessel [82] and Mathieu [83] beams, HGBs also have doughnut intensity profile but do not carry any OAM. In addition to the vast applications ranging from atom optics to plasma physics [66, 67, 68, 69, 78, 71, 72, 73, 74, 75], HGBs have also attracted a great deal of scientific interest in understanding its propagation and transformation dynamics [5, 79, 84, 85]. Generation of HGBs have been realized using linear optical elements in different methods such as, spatial filtering [76], geometrical optics [77], fibers [78], spatial-light-modulator [79], and Laguerre-Gaussian (LG) beam transformation [80]. However, nonlinear generation process enables HGBs to have a new wavelength across electromagnetic spectrum and also to have high output power, higher order in all timescales as required for most of the applications [73, 74, 75].

The HGBs have similar functional form [5] as that of optical vortex beams except azimuthal phase term, $\exp(-il\theta)$, l is the topological charge or OAM mode of the vortex. Therefore, HGBs can be generated by removal of azimuthal phase term of the vortices [80]. Given that the nonlinear frequency conversion processes [9, 86, 28] satisfy OAM conservation [87, 57], one can in principle, remove the azimuthal phase terms of the generated beam through annihilation of OAM modes of the interacting beams in three wave-mixing process. As a proof of principle, here we report, for the first time to the best of our knowledge, nonlinear generation of HGBs. Based on sum frequency mixing of two OAM carrying ultrafast beams at 1064 nm and 532 nm having equal OAM orders but opposite helicity in a nonlinear medium, we have generated HGBs of order as high as 6 and output power as much as 180 mW at 355 nm. It's a generic concept and can be extended to any wavelength and time scale. In addition, by controlling the sign of the helicity of

OAM modes one can generate higher order optical vortices at desired wavelengths. We also propose a new and only method to characterize the order of the HGBs.

For theoretical understanding of nonlinear generation of HGBs we consider SFG of two pump vortex beams (denoted by $m = 1, 2$) with transverse electric field amplitude given as [4]

$$E_m(\rho, \phi) = \left(\frac{\rho}{w_G}\right)^{|l_m|} \exp\left(-\frac{\rho}{w_G}\right)^2 \exp(il_m\phi) \quad (5.1.1)$$

where, l_m is the order of the vortex and w_G is the waist radius of the Gaussian beam confining vortex beam. From the coupled wave equations of SFG process [9] under perfect-matching, the transverse electric field amplitude of the generated field can be represented in the form,

$$E_3(\rho, \phi) = \left(\frac{\rho}{w_0}\right)^{|l_1|+|l_2|} \exp\left(-\frac{\rho}{w_0}\right)^2 \exp(i(l_1 + l_2)\phi), \quad (5.1.2)$$

in special case, the pump beams having same OAM orders but opposite in helicity ($l_1 = -l_2 = l$, as schematically shown in Fig. 5.1.1a), the field amplitude of the generated beam (5.1.2) have the form of HGBs [5]

$$E = \left[\left(\frac{\rho}{w_o}\right)^2\right]^l \exp\left(-\frac{\rho}{w_o}\right)^2 \quad (5.1.3)$$

The electric field distribution of HGB is similar to that of vortex beams but without azimuthal-phase variation or OAM. The order of HGBs is same as the order, l of the pump vortices. This simple mathematical treatment clearly indicates the possibility of nonlinear generation of HGBs with desired orders and frequency across the electromagnetic spectrum.

The schematics of the experimental setup is shown in Fig. 5.1.1b (also see section 5.2). A Yb-fiber ultrafast laser with Gaussian intensity profile at 1064 nm is frequency-doubled into green at 532 nm [28]. Using spiral phase-plates (SPP) and vortex-doubler [57] both the unconverted beam at 1064 nm and green beam at 532 nm are transformed into vortices of order, l , up to ± 6 . The direction of phase variation (clock-wise or anti-clock wise) of SPP to the input beam determines the sign of its vortex. By careful choice of the beam direction

with respect to SPP we can make the pump beams at 1064 nm and 532 nm to carry vortices of same order but opposite signs. These beams while interacting in barium β -borate (BBO) crystal through sum-frequency-generation (SFG) process produce optical radiation at 355 nm. First column of Fig. 5.1.1c shows experimental intensity profile of the SFG beam for pump vortices of order $l = 1, 3, 6$. Like vortex beams [57], the newly generated SFG beams also carry dark core and the annular ring diameter increasing with the order. The theoretical intensity profiles (see 2nd column of Fig. 5.1.1c) obtained from the coupled amplitude equations of SFG process with the experimental parameters show a close agreement with the experiment. The striking similarity between the line intensity profiles (see Fig. 5.1.1d) of the SFG beams to that of the characteristic intensity line profile [5] of HGB indicates the possibility of generation of HGB through nonlinear process. However, the vortex beams also have intensity profiles similar to that of HGBs but carry OAM. Therefore, to confirm the generation of HGBs through nonlinear interaction, we verified the absence of OAM in SFG beam generated from pump beams having OAM using interferometric technique [88]. Each of the beams is passed through a balanced polarizing beam-splitter (PBS) cube based Mach-Zehnder interferometer (MZI) [88] with a dove prism in one of its arm and recoded the beam (see Fig. 5.1.2) after a polarizer (see methods). The first and second column of Fig. 5.1.2, show the ring lattice structure, a signature pattern of azimuthal phase variation, and corresponding number of lobes confirms the vortex order of both the pumps to be $l = 1, 3$ and 6. However, the absence of ring structure in the superposition state of SFG beams (see third column of Fig. 5.1.2), a clear indication of nonexistence of azimuthal phase variation and OAM, confirms nonlinear generation of HGBs. The annihilation of OAMs of the interacting pump beams in nonlinear processes results HGBs with zero OAM.

None of the existing techniques used to reveal the order of DHBs can be extended to determine the order of HGBs. Therefore, it is imperative to device new technique to determine the order of HGBs. The intensity distribution of the Fourier transformation (FT) of HGB of order, l , in polar co-ordinates (ρ, θ) have mathematical form [5]

$$\tilde{I}(\rho, \theta) = |\exp(-\rho^2) \mathcal{L}_l(\rho^2)|^2 \quad (5.1.4)$$

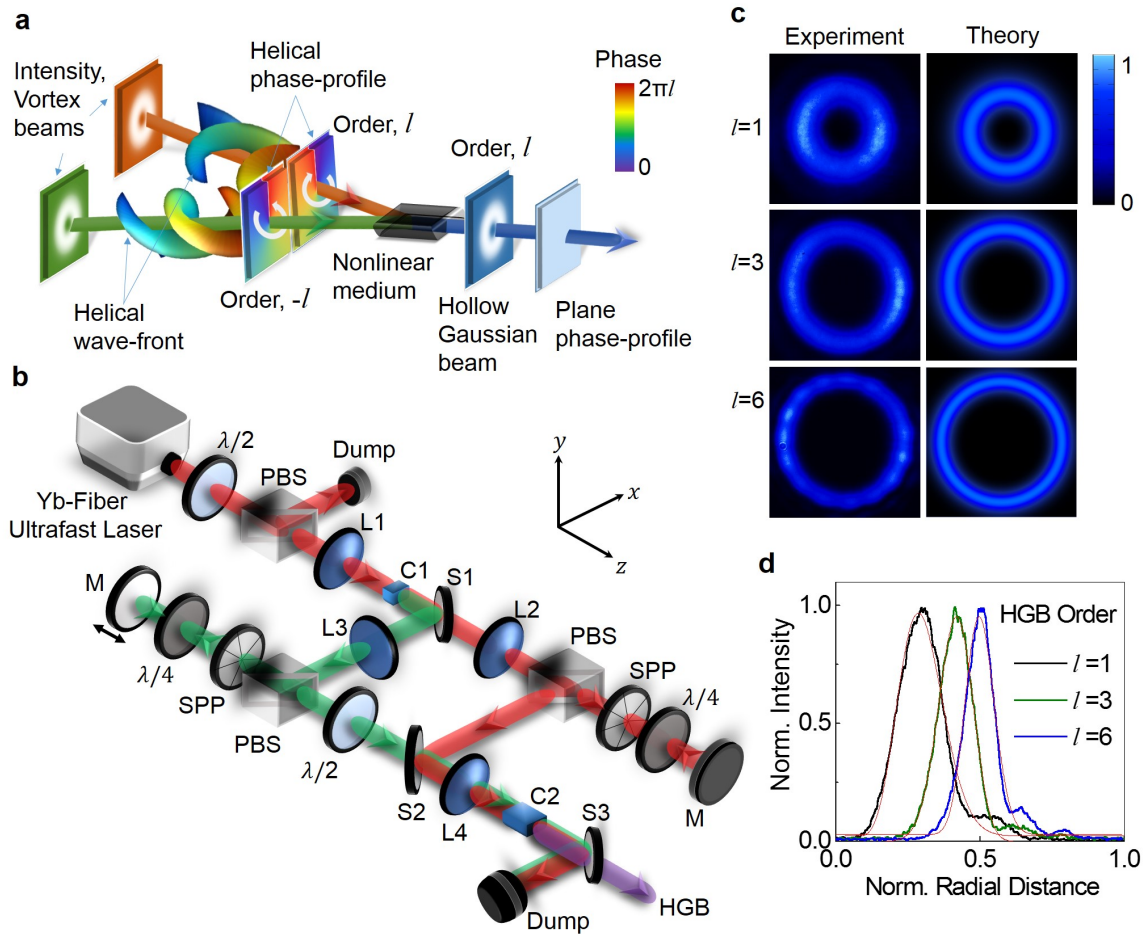


Figure 5.1.1: **Nonlinear generation of hollow Gaussian beam:** a, Pictorial representation of SFG of optical vortex beams of same OAM orders but opposite helicity producing HGBs. b, Schematics of the experimental setup. $\lambda/2$, Half-wave-plate; PBS, Polarizing beam splitter cube; L1-4, Lenses; C1-2, Nonlinear crystals for wavemixing; SPP, SPP; S1-3, Dichroic mirrors; $\lambda/4$, Quarter-wave plate. c, Experimental (first column) and theoretical (second column) images of the intensity profile of HGBs of order, $l = 1, 3$ and 6 (from top to bottom). d, Line intensity profile of the generated HGBs of order, $l = 1, 3$ and 6 .

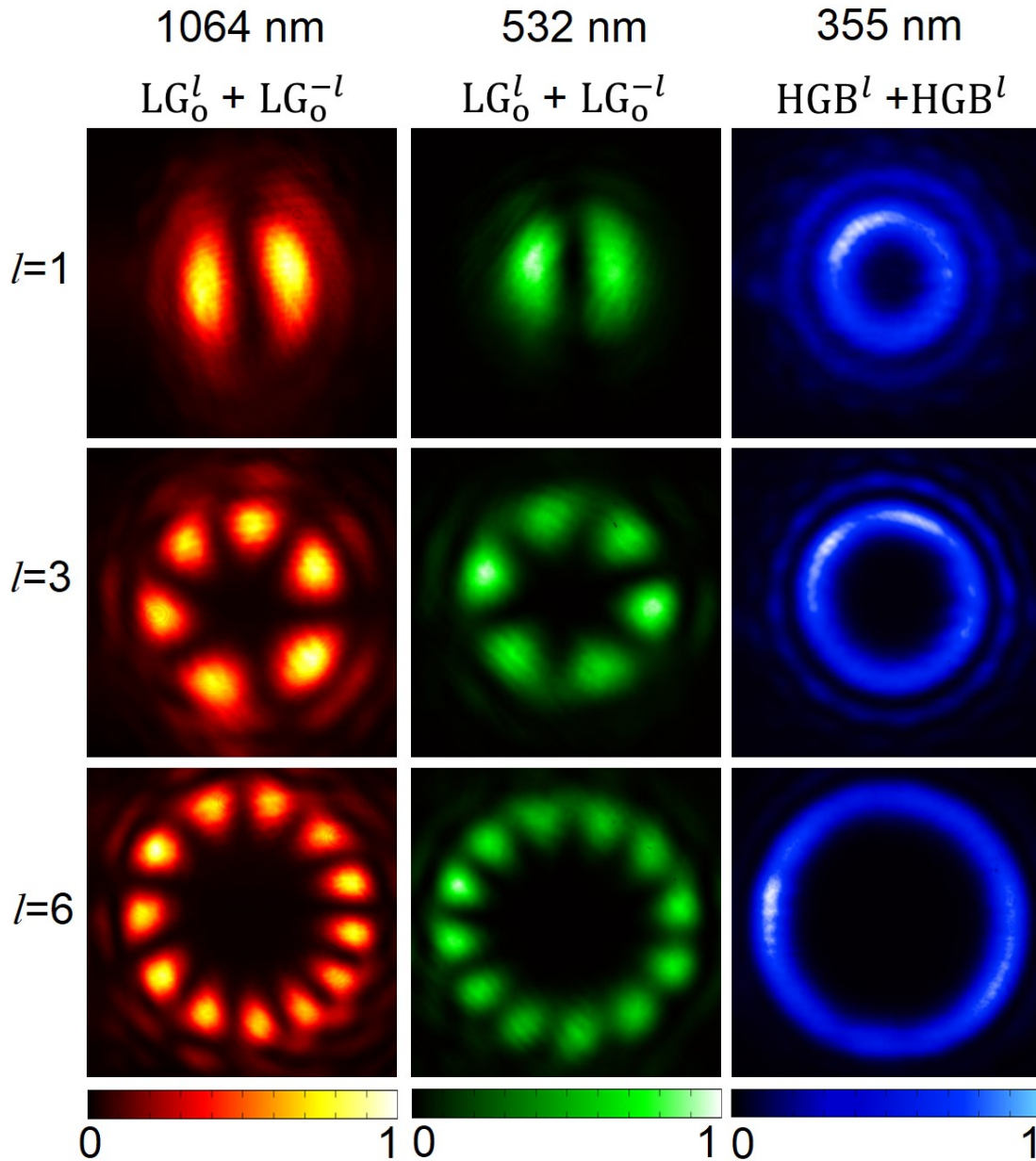


Figure 5.1.2: **Verification of OAM modes of the interacting beams in SFG process for the confirmation of hollow Gaussian beam generation.** Experimental ring lattice intensity pattern of diagonal projection of superposition state, $(|H, LG^l\rangle + |V, LG^{-l}\rangle)$ of pump beams at 1064 nm (first column) and 532 nm (second column) confirming the existence of OAM in both the pump beams with order of $l = 1, 3,$ and 6 (top to bottom). Third column shows interferogram for the SFG beam after passing through the same MZI, confirming nonexistence of azimuthal phase (OAM) and successful generation of HGBs of order $l = 1, 3,$ and 6 (top to bottom).

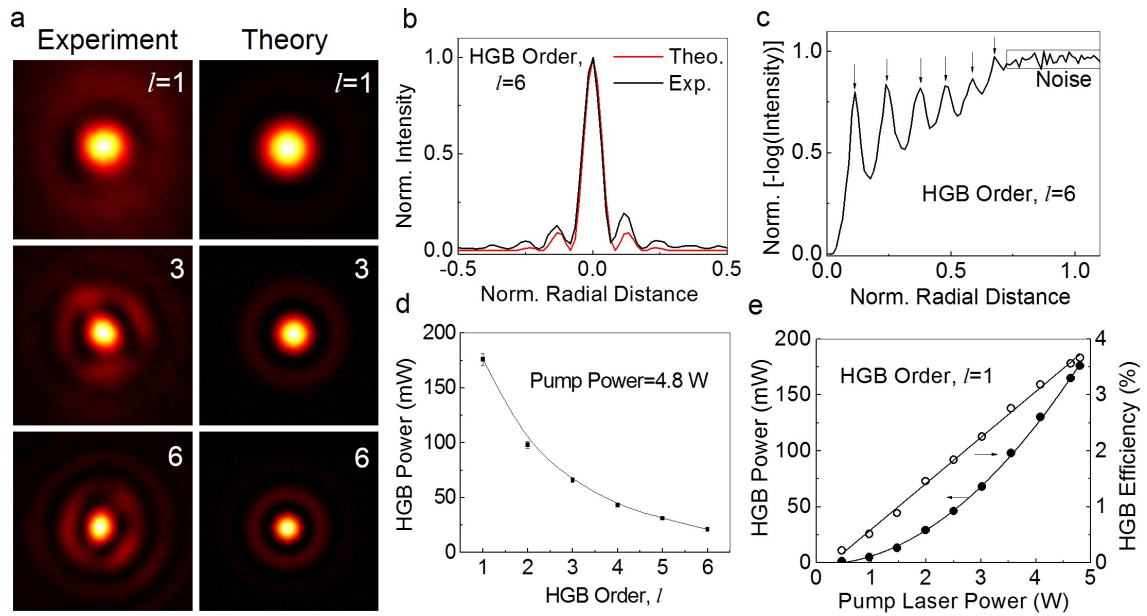


Figure 5.1.3: **Determination of order of HGBs and characterization of the nonlinear generation of HGBs generation.** a, Experimental (first column) and theoretical (second column) images of intensity profile of HGBs, of orders, $l = 1, 3$ and 6 (top to bottom) recorded at Fourier plane. b, Experimental (red line) and theoretical (black line) radial intensity distribution of HGB of order $l = 6$ at the Fourier plane. c, Normalized negative logarithmic radial intensity distribution of the HGB recorded at the Fourier plane reveals the order of HGB (here order is $l = 6$) d, Exponential decay in the output power of HGBs with its order. e, Quadratic (linear) dependence of HGB power (efficiency) to the input laser power.

Here, \mathcal{L} is the Laguerre polynomial with radial index, l . The intensity distribution of FT of HGB [see 5.1.4] of order l , is a Laguerre-Gaussian beam (radial index, $l \neq 0$ and azimuthal index, $p = 0$) modulated by a Gaussian envelope. Unlike intensity distribution of FT of vortex beam resulting vortex beam with a dark hole at the center, the intensity distribution of FT of HGBs produces maximum intensity point at the center ($\rho = 0$) followed by ripples corresponding to the order, l , of HGBs. Counting the number of ripples one can, in principle, determine the order of HGBs. In experiment we recorded the intensity distribution of the HGB of orders $l = 1, 3$ and 6 (first column of Fig. 5.1.3a) at Fourier plane of a lens of focal length $f = 150$ mm and found that the number of rings are increasing with the order, l . The theoretical images (second column of Fig. 5.1.3a) obtained from 5.1.4 using experimental parameters shows close agreement with the experimental images. For better understanding, we recorded the theoretical (red line) and experimental (black line) line profiles for FT of HGB of order $l = 6$ (Fig. 5.1.3b). However, it is difficult to appreciate the number of ripples present in the images in order to find the order of the HGBs. That is due to that fact that the exponential decay term present in the intensity distribution of FT of the HGB [see 5.1.4] falls steeply as compared to the Laguerre polynomial suppressing the characteristic ripple structures. For accurate determination of the order of HGBs we have changed intensity scale from linear to negative log-scale (see Fig. 5.1.3c) enhancing the visibility of the small details of intensity distribution of FT of HGBs. The HGB of order $l = 6$ have clear six peaks (arrows in Fig. 5.1.3c) confirming the reliability of our technique to determine the order of HGBs. We studied the variation of HGB output power with its order (Fig. 5.1.3d). For a fixed fundamental pump power (~ 4.8 W), we found that the HGB power decreases exponentially from ~ 180 mW to 21 mW with the increase of its order from $l=1$ to 6. Such drop in HGB power can be attributed to the decrease of nonlinear gain with the order of the pump vortex similar to the effect observed in nonlinear generation of vortex beams [57]. We also observed the power scaling effect in the nonlinear generation of HGB (Fig. 5.1.3e) of order $l = 1$. The output power (efficiency) of the HGB show quadratic (linear) dependence to laser power in SFG process [86] resulting maximum power of 180 mW with single-pass IR-UV conversion efficiency of 3.7%.

In conclusion, we have demonstrated, for the first time to the best of our knowledge, that annihilation of two optical vortices of same order with opposite sign in a nonlinear medium

produces a new class of dark core beam, known as HGB. We have generated HGBs of order as high as 6 and power as high as 180 mW at 355 nm. The nonlinear generation scheme can be used to generate HGB at any wavelength across the electromagnetic spectrum. We have also devised a new and only method to characterize the order of such HGBs.

5.2 Methods

Experimental setup: The schematic of the experimental setup for nonlinear generation of HGBs is shown in Fig. 5.1.1b. An ultrafast Yb- fiber laser of average power 5 W is used as the primary laser source. The laser produces femtosecond pulses in sech^2 shape with temporal width (full width at half-maxima, FWHM) of ~ 260 fs at a repetition rate of 78 MHz. The spectral width (FWHM) of the laser is measured to be ~ 15 nm centered at 1060 nm. Operating the laser at its highest power to access its optimum performance in terms of temporal width, a combination of half wave plate ($\lambda/2$) and a polarization beam splitter (PBS) cube is used to control the laser power to the nonlinear crystals. A lens, L1 of focal length, $f = 100$ mm is used to focus the beam at the center of a 1.2-mm-long BIBO (BiB_3O_6) crystal (C1) for SHG of Yb-fiber laser into green at 532 nm. The SHG stage is similar to the one used in our previous work [28]. The SHG stage produces 1.04 W of green power for fundamental power of 4.8 W in Gaussian beam profile. The dichroic mirror, S1 is used to extract green radiation from the fundamental wavelength. Lenses, L2 and L3 both of same focal length ($f = 100$ mm) collimate unconverted fundamental and generated green beams respectively. The green beam and unconverted fundamental beams are used as pump beams for SFG process. Using two spiral phase plates, SPP1 and SPP2 having spiral winding corresponding to vortex order of 1 and 2 respectively and a vortex-doubler setup [57] comprising of a PBS, quarter wave-plate ($\lambda/4$) and a high reflectance mirror, M, we separately transformed the green and unconverted fundamental radiation in Gaussian spatial profiles into optical vortices of order, $l = 1-6$. The working principle of the vortex-doubler can be found elsewhere [57]. The direction of phase variation (clock-wise or anti-clock wise) of SPP to the input beam determines the sign ($\pm l$) of its vortex. By careful choice of the beam direction with respect to SPP we can make both green and unconverted fundamental beams to carry vortices of same order but in same/opposite sign.

These two beams are recombined using a dichroic mirror, S2, and focused at the center of a 5-mm-long BiB_3O_6 (BIBO) crystal (C2) cut at $\theta = 137^\circ$ ($\phi = 90^\circ$) in yz optical plane for collinear type-I ($e + e \rightarrow o$) phase-matched SFG of 1064 nm and 532 nm at normal incidence. One of the mirrors, M, is placed on a translation stage for temporal overlapping of the interacting beams in the nonlinear crystal, C2. The dichroic mirror, S3 is used to extract the SFG beam at 355 nm from the unconverted beams at 1064 nm and 532 nm. The intensity profile of the beam is recorded using a CCD based beam profiler.

Confirmation of nonlinear generation of HGBs: The azimuthal phase variation of beams, a signature of OAM modes, is measured using an interferometric technique [88]. An optical beam having OAM (LG, Laguerre-Gaussian) mode of arbitrary order l polarized at 45° (diagonal) can be represented as, $|D, LG^l\rangle = \frac{1}{\sqrt{2}} (|H, LG^l\rangle + |V, LG^l\rangle)$, where $|H\rangle$ and $|V\rangle$ denotes the orthogonal polarisation states. If such a beam passes through balanced polarising beam splitter based Mach-Zehnder interferometer (MZI) [88] with a Dove prism in one of its arm, the extra reflection due to Dove prism transforms the input beam into new superposition state represented as $(|H, LG^l\rangle + |V, LG^{-l}\rangle)$. The diagonal projection of this state having the form $\frac{1}{\sqrt{2}} (|LG^l\rangle + |LG^l\rangle)$ results a ring lattice structure with $2l$ number of radial fringes or petals. Therefore, 2, 6 and 12 number of petals in first two columns of Fig. 5.1.2 confirms that both the pump beams at 1064 nm (first column of Fig. 5.1.2) and 532 nm (second column of Fig. 5.1.2) have OAM modes $l = 1, 3$ and 6. However, due to nonexistence of OAM mode in HGBs, the extra reflection due to Dove prism does not alter the output state from the input state, $(|H, HGB^l\rangle + |V, HGB^l\rangle)$. Here, hollow Gaussian beam mode of order, 1 is represented by $(|HGB^l\rangle)$. The diagonal projection of such state results output beam of the form $\frac{1}{\sqrt{2}} (|H, LG^l\rangle + |V, LG^l\rangle)$, the HGB itself (see third column of Fig. 5.1.2). Such observation proves the nonexistence of azimuthal phase and OAM and successful generation of HGBs of order up to 6.

Chapter 6

Generation of ultrafast tunable Airy beam

This chapter constitutes the following journal publications:

1. *Ultrafast Airy beam optical parametric oscillator*,
Apurv Chaitanya N, S. Chaitanya Kumar, A. Aadhi, G. K. Samanta, and M. Ebrahim-Zadeh
Scientific Reports 6, 30701 (2016).

6.1 Ultrafast Airy beam optical parametric oscillator

6.1.1 Introduction

Mathematical resemblance of paraxial wave equation to the free particle Schrödinger wave equation having Airy wave packet solution [89] enabled prediction [90] and demonstration [13] of optical beam having transverse intensity distribution described by the Airy function. Unlike other structured beams, Airy beam has peculiar characteristics such as beam shape invariance with propagation, propagation along curved trajectory in free space, and self-restoration of beam shape even after obstruction by small objects. Right after the first experimental demonstration [13], the Airy beam has attracted a great deal of attention for potential applications in diverse areas including optical routing [91], manipulation of

microscopic particles [92, 93], optically mediated particle clearing [94], and laser micromachining [95]. Additionally, propagation characteristics of the Airy beam in nonlinear [96, 97, 98, 99, 100, 101, 102] and turbulent medium [103] have been studied for the generation of curved plasma channel [98], supercontinuum and solitary wave [98, 99] and laser filamentation [101, 102]. Efforts have also been made to demonstrate Airy beam with electron waves [104], acoustic waves [105] and surface plasmon polaritons [106]. Many of the applications and studies such as laser micromachining of curve surfaces, laser filamentation, supercontinuum generation and curved plasma channel require high power, ultrafast Airy beams with different spectral and temporal parameters at different wavelengths across the electromagnetic spectrum. Conventionally, the Airy beam is generated through cubic phase modulation of laser beam in Gaussian intensity distribution and subsequent Fourier transformation [13]. However, none of the Airy beam generated so far have high energy, and wide wavelength tunability from a single system in the ultrafast regime. For high power Airy beam with wide wavelength tunability in cw [107], we have recently explored the intrinsic wavelength tunability and high intra-cavity power of a continuous-wave (cw) singly resonant optical parameter oscillator (SRO) [108]. Here, we present, for the first time, a new class of Airy beam source based on cubic phase modulation and subsequent Fourier transformation of intra-cavity resonant signal of an ultrafast SRO producing output pulses with temporal width (full width at half maxima, FWHM) of ~ 23 ps in 2-D Airy intensity distribution with power as much as 306 mW tunable across 1477-1727 nm.

6.1.2 Theory

The two-dimensional (2-D) intensity distribution of a finite energy Airy beam can be expressed in the form

$$I(s_m) = \prod_{(m=x,y)} \text{Abs} [\text{Ai}(s_m) \exp(a_m s_m)]^2 \quad (6.1.1)$$

Here, $\text{Ai}(s_m)$ is the Airy function [90], $s_x = x/x_0$ and $s_y = y/y_0$, are the normalized transverse coordinates along x and y axis respectively (see Fig. 6.1.1) and x_0, y_0 are the transverse scaling parameter (characteristic parameters) and a is the truncation parameters which determines the extent of Airy beam in 2-D plane (x - y plane). The parabolic trajectory of

the Airy beam, of wavelength λ , along x and y axis as the beam propagates along the z axis is determined by the characteristic parameters, x_0, y_0 and the launching angle, θ_x and θ_y , through the relation, $m_d = d_m z^2 + \theta_m z$, where $m = x, y$ and $d_m = \lambda^2 / 16\pi^2 m_0^3$. For the special case in which $x_0 = y_0$ (symmetric Airy beam) the transverse acceleration in the x - y plane can be expressed as [90]

$$\mathbf{d} = \frac{\sqrt{2}\lambda^2}{16\pi^2 x_0^3} \hat{\mathbf{e}}$$

where, $\hat{\mathbf{e}}$ is a unit vector on the $x - y$ plane along the direction of acceleration, which is determined by the relative orientation of the beam in the x - y plane. In this case, $x_0 = y_0$, the parabolic trajectory with respect to $\hat{\mathbf{e}}$ along the propagation is given by

$$e_d = d_z^2 + \theta_e z \quad (6.1.2)$$

where, θ_e is the angle the beam makes with respect to the unit vector $\hat{\mathbf{e}}$. To generate finite energy Airy beam, we modulated the phase and amplitude of the Gaussian beam using a cubic phase mask in the form of a binary diffraction grating with amplitude transmittance as [90]

$$h(x, y) = \frac{1}{2} h_o \left[\text{sgn} \left\{ \cos \left(\frac{2\pi x}{\Lambda} + c_o^3 (x^3 + y^3) / 3 \right) \right\} + 1 \right]$$

Here, h_o , is the ridge height of the grating with period Λ , defined by the ratio of the number of lines N , along the width L , of the grating in x direction. The constant, c_o represents the strength of cubic phase modulation in the transverse direction. The phase of the 1st order diffracted beam can be represented as, $\exp(i\phi(x, y)) = \exp(ic_o^3(x^3 + y^3)/3)$.

6.1.3 Experiment

The experimental setup used for the generation of ultrafast Airy beam SRO is schematically represented in Fig. 6.1.1(a). An ultrafast Yb-fiber laser (Fianium, FP1060-20) providing a maximum average power of 20 W with pulse width of 20 ps and repetition rate of 78 MHz is used as the pump for the Airy beam source. It has a spectral width of 1.4 nm centered at 1064 nm. The laser is operated at its full power and the input power to the SRO is controlled using an attenuator based on a half-wave-plate ($\lambda/2$) and a polarizing beam splitter cube.

A second $\lambda/2$ plate is used for manipulating the input polarization of the pump beam to the SRO. A lens, L1, of focal length $f = 175$ mm is used to focus the pump beam into the center of the 50-mm-long, 8.6-mm-wide and 1-mm-thick, multi grating MgO:PPLN crystal (C) which is used for the SRO operation. The crystal has 7 channels with grating period, from 28.5 to 31.5 μm with steps of 0.5 μm , and it's both faces are antireflection (AR) coated for 1400 nm to 2000 nm and at pump wavelength. The crystal is housed in an oven (not shown in figure) whose temperature can be varied from room temperature to 200°C in steps of 0.1°C. The SRO cavity is designed in a four mirrors ring cavity with two plano-concave mirrors (M1-2) of radius of curvature (ROC= 100 mm), plane mirror, M3 and a plane output coupler (OC). The cavity length is perfectly synchronized to the repetition rate of the pump laser. All mirrors, M1–3, are antireflection (AR)-coated for high transmission ($T > 90\%$) at 1064 nm for the pump, high transmission ($T > 80\%$) over 2200–4000 nm for the idler, and high reflectivity ($R > 99\%$) over 1300–1900 nm for the signal, ensuring SRO operation. The OC has a partial transmission, $T \sim 5\%$ over 1100–1630 nm. A custom designed cubic phase mask (CPM) in the form of binary grating is introduced inside the SRO cavity between mirror M3 and OC, to modulate amplitude and phase of the resonant Gaussian beam in the first order diffracted beam. The grating has $N = 100$ lines in $L = 2$ mm width resulting a carrier period of 20 μm . The ridge height h_o is optimized to have 0^{th} transmission $\sim 95\%$ at 1500 nm resulting $\sim 5\%$ coupling of the intra-cavity signal into Airy beam in first diffraction order. It is to be noted that the higher diffraction orders have negligibly small intensity. The CPM has cubic phase modulation strength estimated to be, $c_o = 5.77/\text{mm}$ [107]. The Fourier transforming lens, L2, of focal length, $f = 500$ mm is used for Fourier transforming this out coupled beam from the OPO for generating Airy beam.

6.1.4 Results and discussion

The output intensity profile at the focus of the Fourier transforming lens, recorded using a CCD based camera is shown in Fig. 6.1.1(d). The recorded intensity profile clearly confirms the generation of 2-dimensional (2-D) Airy intensity profile. The parameters x_0, y_0, a_x, a_y of the generated beam were determined by fitting the intensity profile with a

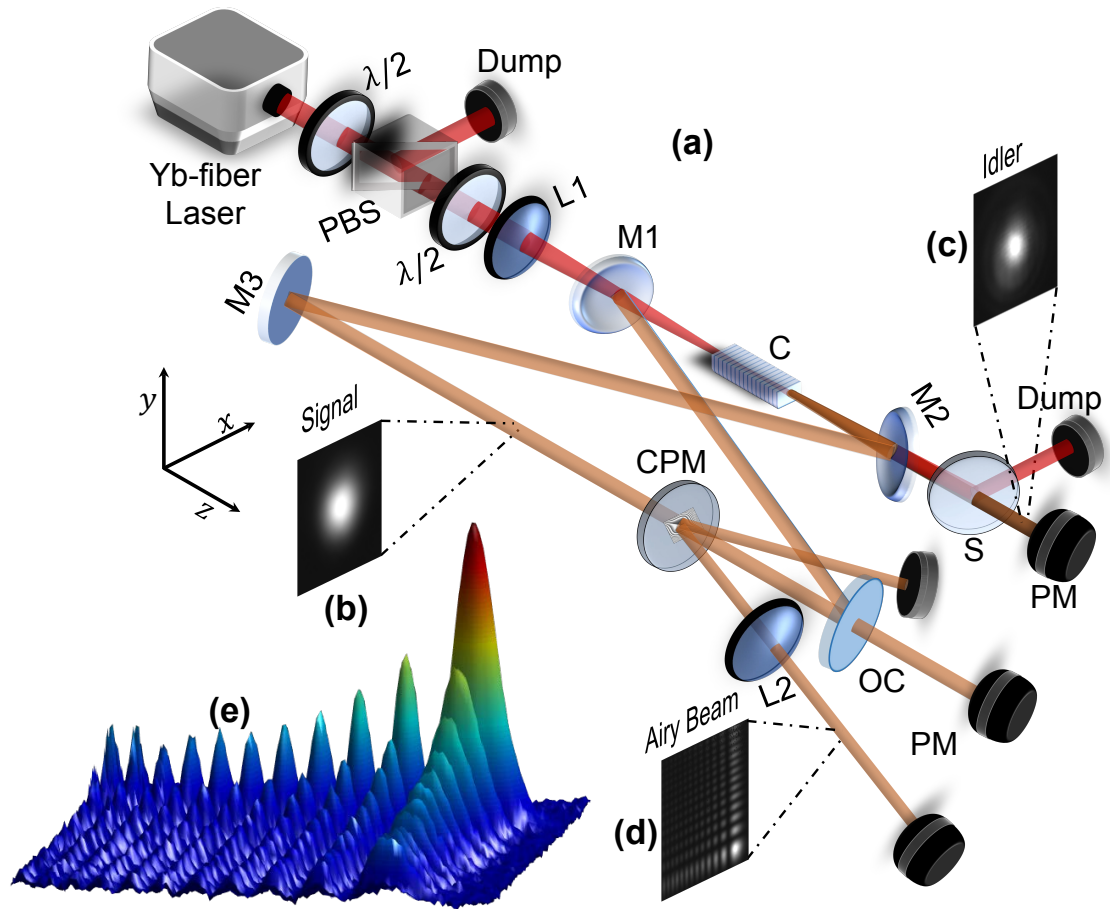


Figure 6.1.1: (a) Schematics of the experimental setup for the ultrafast Airy beam OPO. $\lambda/2$; half-wave plate, PBS; polarizing beam splitter cube, L1-2; Lenses, M1-3; mirrors, OC; output coupler, C; MgO:PPLN crystal, CPM; cubic phase mask, S; dichroic mirrors; PM, Power meter. Recorded intensity profile of (b) resonant signal, (c) idler and (d) Airy beam. (e) 3-D illustration of the Airy beam.

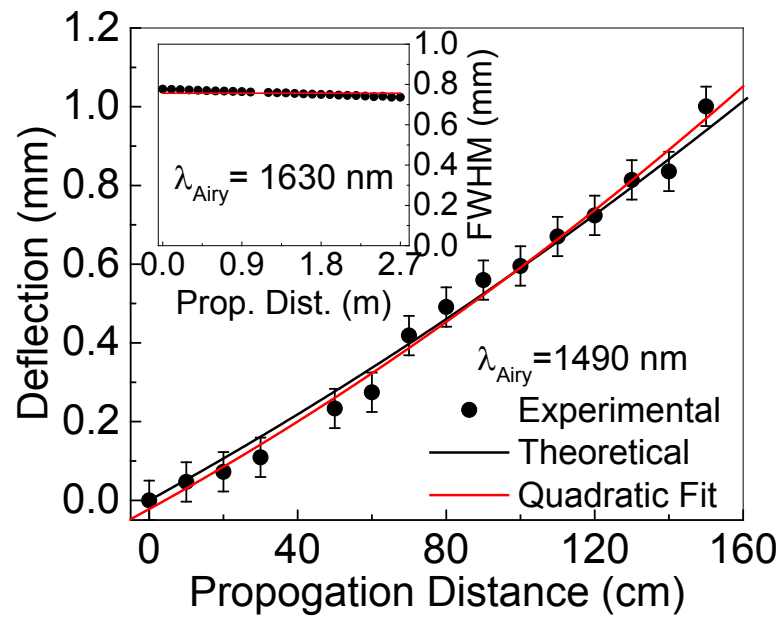


Figure 6.1.2: (a) Measurement of beam acceleration of the Airy beam OPO as a function of propagation distance. Solid line (black) represents theoretically predicted acceleration, (red) is the quadratic fit to the experimental data (dots). (Inset) Variation in the width (FWHM) of the central lobe of the Airy beam over propagation. Solid line (red) is linear fit to data (dots).

2-D Airy function as represented by Eq. 6.1.1. Although the intensity (see Fig. 6.1.1(d)) looks like Airy beam, however, to confirm the generation of Airy beam we have investigated its intriguing properties like acceleration, non-diffraction and self-healing. To study self-acceleration property of the generated beam at an arbitrary wavelength (say, $\lambda_{Airy} = 1490$ nm) across the tuning range of the SRO we recorded the intensity profile as a function of propagation distance and measured (dots) the position (central lobe) of the beam with the results shown in Fig. 6.1.2. As evident from Fig. 6.1.2, the beam deflects from its rectilinear path by a distance of 1 mm over a beam propagation distance of 1.5 m. Using the intensity profiles we measured the transverse scaling parameters, x_0 and y_0 to be ~ 0.65 mm, confirming the generation of symmetric Airy beam. Once the x_0 parameter of the beam is known, apart from an angular offset given by θ_e , the trajectory of the Airy beam can be predicted theoretically using Eq. 6.1.2. Fitting a second degree polynomial (solid red line) to the experimental data points in Fig. 6.1.2 the angular offset θ_e is estimated to be 0.5 mrad. For the given set of x_0 and θ_e the theoretically predicted transverse acceleration is given in Fig. 6.1.2 (solid black line). As evident from the figure, the experimentally observed acceleration is in close agreement with the theoretically predicted values. We also observed self-acceleration of the Airy beam across the tuning range with lower acceleration at longer wavelengths. This is attributed to the fact that the scaling parameters x_0 and y_0 of the Airy beam are linearly proportional to its wavelength [108]. To verify non-diffraction property of the Airy beam we measured the width (FWHM) of the central lobe of the beam at wavelength, $\lambda_{Airy} = 1630$ nm, along propagation over a distance of 2.7 m, with the results given in inset of Fig. 6.1.2. The width of the central lobes varies from 0.77 ± 0.05 mm at $z = 0$ to 0.73 ± 0.05 mm at $z = 2.7$ m. Such observation clearly shows that within the experimental error the beam remains diffraction free (propagation invariant) for > 2.7 m.

We also investigated the self-healing nature of the output beam of the Airy beam OPO at a signal wavelength of 1630 nm with the results shown in Fig. 6.1.3. At a distance, $z = 10$ mm from the focal point of the Fourier lens, L2, we blocked one of the lobes (circled region in Fig. 6.1.3 (a)) of the output beam using a knife edge and recorded intensity distribution of the beam along propagation distance in free space. As evident from Fig. 6.1.3 (b-d), the Airy beam has no second lobe along x - axis of Fig. 6.1.3(b) at $z = 10$ cm, however, at $z = 60$ cm, we can observe the beam intensity to re-appear in the blocked region with

a complete reproduction of the beam shape at propagation distance, $z = 120$ cm. These results clearly confirm the self-healing property of the generated beam. Fig. 6.1.3(e) shows the line profile of the Airy intensity along the propagation for better understanding of the self-healing nature.

After confirming the generation of the Airy beam from the OPO we characterized OPO for its output parameters. Using grating periods, $\Lambda = 29.5, 30, 30.5$ and $31 \mu\text{m}$ of the MgO:PPLN crystal and varying the phase-matching temperature (PMT) we tuned the wavelength of the Airy beam source continuously from 1477 nm to 1727 nm. In addition, the source provides idler radiation across 3805 nm to 2771 nm in Gaussian intensity distribution. The output power of the Airy beam across the entire tuning range while pumping with an input power ~ 10.5 W is given in Fig. 6.1.4. As evident from the figure, for $> 85\%$ of the entire tuning range the Airy beam signal is measured to have an output power > 150 mW. A maximum power of 306 mW was obtained for Airy beam signal at 1632 nm. The lower value of the Airy beam power can be attributed to the lower diffraction efficiency ($\sim 5\%$) of the CPM. Since the MgO:PPLN based OPOs in picosecond time scale are high gain system, to avoid possible crystal damage due to high intra-cavity power of the signal radiation at high pump powers, we used OC ($T \sim 5\%$) to out-couple resonant signal. As a result, the Airy beam source produces signal and idler radiation in Gaussian beam profiles with output power varying in the range of 0.6 to 2.5 W across the tuning range. Such high signal power in Gaussian beam profile suggest further increase of the Airy beam power with CPM grating of optimized diffraction efficiency.

To measure the power scaling property of the Airy beam source, we recorded the Airy beam power at wavelength $\lambda_{\text{Airy}} = 1632$ nm (crystal temperature, $T = 100^\circ\text{C}$ and crystal grating period, $\Lambda_C = 31 \mu\text{m}$) while varying the input pump power of the OPO. The results are shown in Fig. 6.1.5. As evident from the figure, the Airy beam power increases almost linearly with the input pump power with no signs of saturation. A maximum signal Airy beam power of 306 mW was recorded for an input pump power of 10.5 W. We also measured the power of out-coupled Gaussian signal ($\lambda_s = 1362$ nm) and corresponding idler ($\lambda_i = 3057$ nm) beams with the pump power with the result shown in inset of Fig. 6.1.5. The Gaussian signal (idler) is measured to have a maximum power of 1.35 W (1.54 W). The SRO has a threshold < 0.55 W and has a maximum pump depletion $\sim 60\%$.

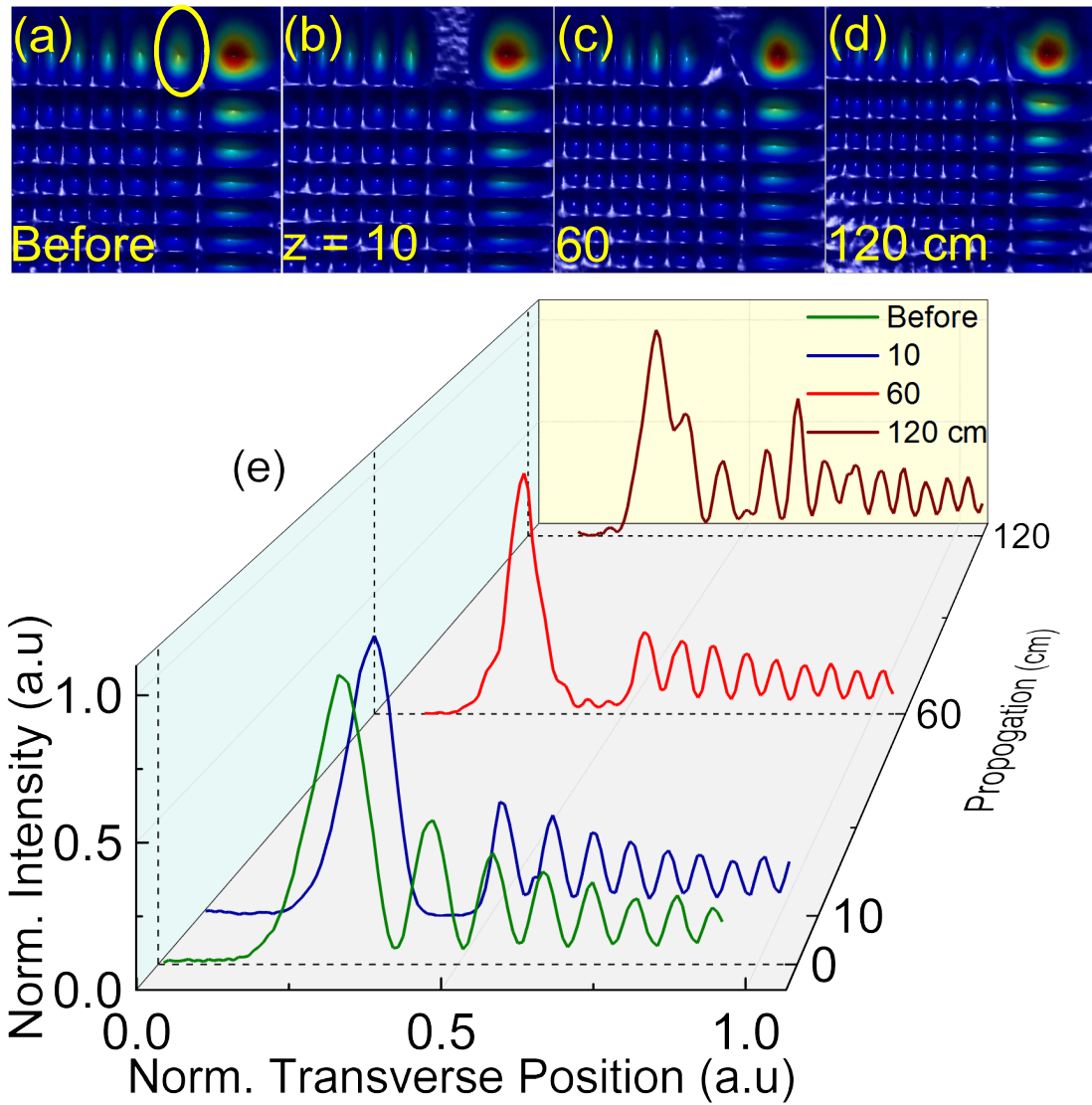


Figure 6.1.3: Verification of self-healing property of the output beam of the Airy beam OPO. The line profile of the beam at a distance $z = 10$ cm (blue line), $z = 60$ cm (red line), $z = 120$ cm (brown line) from the Fourier plane.

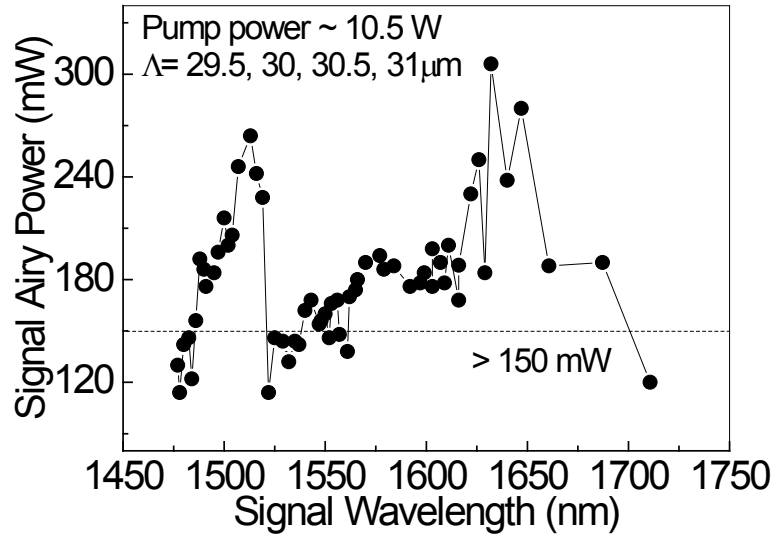


Figure 6.1.4: Variation of the Airy beam power across the tuning range. The source is pumped at 10.5 W.

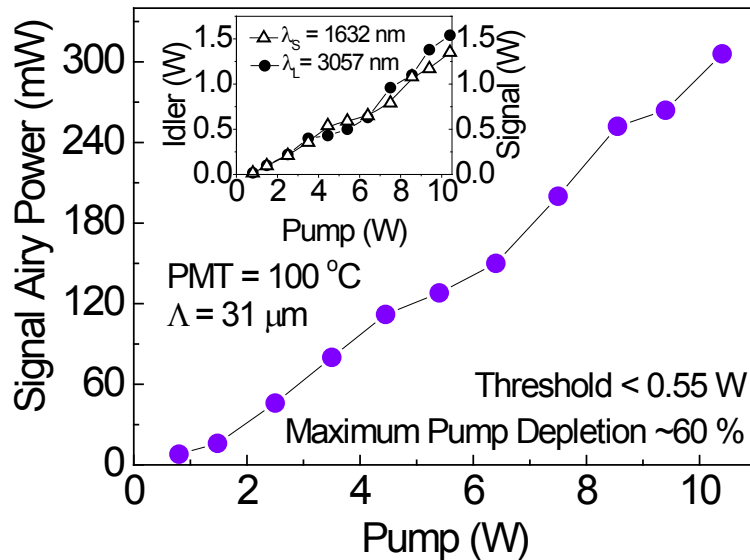


Figure 6.1.5: Variation of Airy beam ($\lambda_{\text{Airy}} = 1632\text{ nm}$) power as a function of the pump power. (Inset) Dependence of out-coupled signal ($\lambda_s = 1632\text{ nm}$) and corresponding idler ($\lambda_i = 3057\text{ nm}$) in Gaussian intensity distribution.

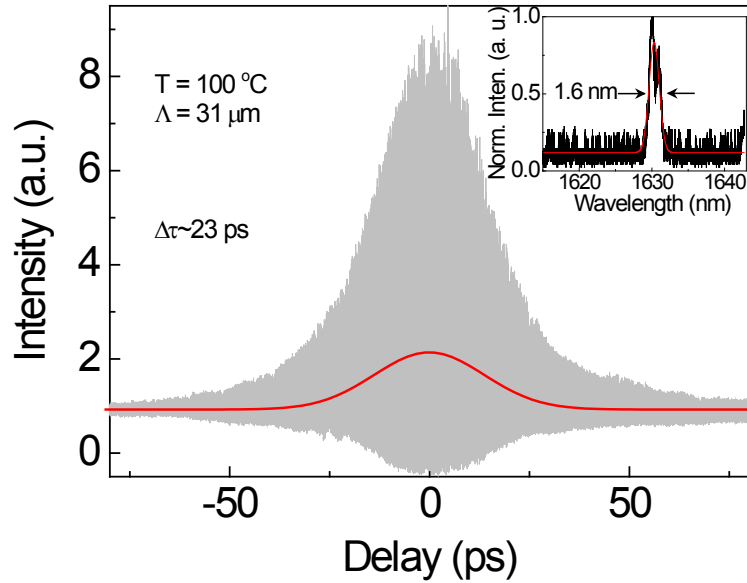


Figure 6.1.6: Interference autocorrelation trace of the signal airy beam and (Inset) corresponding spectral measurement.

We also measured the temporal and spectral width of the Airy beam with the result shown in Fig. 6.1.6. Operating the Airy beam source at 1632 nm, we measured the temporal width of the Airy beam pulses using a home-made interferometric autocorrelator, to be, $\Delta\tau \sim 23$ ps. Simultaneously we measured the spectral width (FWHM) of the Airy beam radiation (as shown in the inset of Fig. 6.1.6) to be $\Delta\lambda = 1.6$ nm centered at 1632 nm resulting a time-bandwidth product of $\Delta\tau\Delta\nu = 4.15$ far away from the transform limit.

In conclusion, we experimentally demonstrated the ultrafast Airy beam SRO. To confirm the generation of Airy beam, we have verified the characteristic properties of the beam in terms of self-acceleration, non-diffraction and self-healing. The Airy beam source produces maximum power of 300 mW across 1477-1727 nm. Using optimized diffraction efficiency of the cubic phase grating we can further increase the output power of the Airy beam. The source produces Gaussian signal (idler) beam of power as much as 1.35 W (1.54 W) for pump power of 10.5 W. The Airy beam source have output pulses of temporal and spectral width of the Airy beam $\Delta\tau \sim 23$ ps and $\Delta\lambda = 1.6$ nm respectively.

Chapter 7

Conclusion and scope for future work

7.1 Conclusion

In this thesis, we have presented the study of nonlinear interaction of structured beams of various temporal and spectral domains. Other than Gaussian beams we have demonstrated vortex beam, hollow Gaussian beam and Airy beam spanning from 266 nm to mid IR wavelengths, from ps to fs regime with high repetition rate and with high power suitable for applications in various fields.

In Chapter 1, we have covered the basics of nonlinear optics which were extensively used throughout my Ph. D. work with special emphasis on second order nonlinear processes. It covers mostly the basics of second order nonlinear processes. We have also included a brief introduction to the structured beams in that chapter. Chapter 2, our experimental study of frequency-doubling of high-average-power femtosecond pulses from an ultrafast Yb-fiber laser at 1064 nm into the green using thick nonlinear crystals with different temporal and spatial walk-off parameters is presented. Using single-pass SHG in BBO and BIBO, we have investigated the effect of focusing on the SH efficiency and found the optimum focusing conditions for the 5-mm-long BBO and BIBO, respectively, in the presence of spatial and temporal walk-off. These results are in good agreement with the theoretical calculations performed using the practical values. Under optimum focusing conditions, we were able to generate respectively up to 2.25 and 2.05 W of green output from BIBO and BBO in single-pass configuration for a maximum available fundamental

power of ~ 5 W at 78 MHz pulse repetition rate. We also investigated the effect of focusing on the SH power and efficiency saturation. Spectral and temporal characterization of the generated SH pulses have been performed and the variation of output spectral bandwidth and pulse duration as function of the focusing parameter, ξ , has been studied. Moreover, the angular acceptance bandwidth of both the crystals for SHG into the green has been measured under various focusing conditions and their dependence on the effective interaction length resulting from the spatial and temporal walk-off has been analyzed. This comparative study provides a systematic analysis for the attainment of optimum SH performance with regard to output power, spectrum, pulse duration, and beam quality of the generated green beam in the presence of limiting factors of spatial and temporal walk-off in thick BBO and BIBO crystals for single-pass SHG of the state-of-the art femtosecond Yb-fiber lasers. An important overall conclusion of that study is that the performance of the SHG process is far more strongly dictated by spatial walk-off than temporal walk-off.

Chapter 3, addresses frequency doubling characteristics of high-power, ultrafast, optical vortex beams. We also demonstrated a new scheme to generate optical vortices of orders $l_{sh} = 1 - 6$ by using only two SPPs of phase winding 1 and 2. Using single pass SHG, we have generated optical vortices up to 12th order with maximum vortex SH power of 900 mW (383 mW) at single-pass conversion efficiency as high as 19.5% (5.2 %) in green (DUV). We observed the decrease of vortex SH efficiency with vortex order. Such effect is attributed to the increase of vortex area with order. Like Gaussian beams, vortices also have focusing-dependent SH efficiency. However, at higher orders the optimum focusing is realized at relatively tighter focusing. Additionally, we have also observed that the vortices have higher angular acceptance bandwidth than that of Gaussian beams. In case of DUV vortex generation, we also experimentally observed the influence of spatial structure of the fundamental beam on the angular phase-matching bandwidth of the nonlinear crystal.

Chapter 4, describes the experimental demonstration of efficient nonlinear generation of high power, higher order, ultrafast "perfect" vortices at the green with output power > 1.2 W and vortex order up to $l_{sh} = 12$ at single-pass conversion efficiency of 27%. This is the highest efficiency in the single-pass SHG of any structured beam. Chapter 5, addresses the nonlinear interaction of photons having OAMs of equal magnitude but in opposite sign. We have experimentally demonstrated that the resultant field will be a hollow Gaussian

beam with no OAM. Finally in Chapter 6, we experimentally demonstrated the ultrafast Airy beam SRO OPO. To confirm the generation of Airy beam, we have showed that the beam possesses the characteristic properties of self-acceleration, non-diffraction and self-healing. The Airy beam source produces maximum power of 300 mW across 1477-1727 nm. Using optimized diffraction efficiency of the cubic phase grating we can further increase the output power of the Airy beam. The source produces Gaussian signal (idler) beam of power as much as 1.35 W (1.54 W) for pump power of 10.5 W. The Airy beam source have output pulses of temporal and spectral width of the Airy beam $\Delta\tau \sim 23$ ps and $\Delta\lambda = 1.6$ nm respectively.

7.2 Scope for future work

Nonlinear optics have been predominantly based on Gaussian beam interaction. We have, through this work, extended the domain of nonlinear optics towards a relatively unexplored domain- nonlinear interaction of structured beams. We have studied vortex beams, hollow Gaussian beams, "perfect" vortex beam and Airy beams. However, there are a lot of other structured beams whose nonlinear interaction is little known or not explored explicitly. There is always scope of studying such beams in future. In the present study, spectral domains achieved are limited to DUV to mid IR, however extending the generation of such beams in THz regimes and other difficult wavelengths are always challenging and worth a thorough investigation. We have demonstrated the generation of structured beams in ultra fast regimes where, the nonlinear gain is sufficiently high due to high peak power of ultrafast lasers. Using new crystals with high nonlinearity we would like to extend the study towards CW regimes in future. On the other hand, it would be also very much interesting to study the higher harmonic generation of structured beams using high energy ultra fast laser. Hence the field is still open with lot of unexplored topics which require further understanding of the nonlinear interaction, propagation dynamics and competing effects of structured beam generation.

Bibliography

- [1] G. D. Boyd and D. A. Kleinman, “Parametric interaction of focused Gaussian light beams,” *J. Appl. Phys.* **39**, 3597–3639 (1968).
- [2] H. Wang and A. M. Weiner, “Efficiency of Short-Pulse Type-I Second-Harmonic Generation With Simultaneous Spatial Walk-Off, Temporal Walk-Off, and Pump Depletion,” *IEEE J. Quant.* **39**, 1600–1618 (2003).
- [3] S. Saitiel, K. Koynov, B. Agate, and W. Sibbett, “Second-harmonic generation with focused beams under conditions of large group-velocity mismatch,” *J. Opt. Soc B* **21**, 591–598 (2004).
- [4] L. Allen, M. W. Beijersbergen, R. J. C. Spreeuw, and J. P. Woerdman, “Orbital angular momentum of light and the transformation of Laguerre-Gaussian laser modes,” *Phys. Rev. A* **45**, 8185–8189 (1992).
- [5] Y. Cai, X. Lu, and Q. Lin, “Hollow Gaussian beams and their propagation properties,” *Opt. Lett.* **28**, 1084–1086 (2003).
- [6] P. A. Franken, A. E. Hill, C. W. Peters, and G. Weinreich, “Generation of Optical Harmonics,” *Phys. Rev. Lett.* **7**, 118–119 (1961).
- [7] D. J. Griffiths and R. College, *Introduction to electrodynamics* (prentice Hall, 1999).
- [8] R. W. Boyd, *Nonlinear Optics* (Academic Press, 2008).
- [9] R. L. Sutherland, *Handbook of nonlinear optics* (CRC press, 2003).

- [10] T. F. Scott, B. A. Kowalski, A. C. Sullivan, C. N. Bowman, and R. R. McLeod, “Two-Color Single-Photon Photoinitiation and Photoinhibition for Subdiffraction Photolithography,” *Science* **324**, 913–917 (2009).
- [11] A. Mair, A. Vaziri, G. Weihs, and A. Zeilinger, “Entanglement of the orbital angular momentum states of photons.” *Nature* **412**, 313–6 (2001).
- [12] A. S. Ostrovsky, C. Rickenstorff-Parrao, and V. Arrizón, “Generation of the "perfect" optical vortex using a liquid-crystal spatial light modulator.” *Opt. Lett.* **38**, 534–6 (2013).
- [13] G. A. Siviloglou, J. Broky, A. Dogariu, and D. N. Christodoulides, “Observation of accelerating Airy beams.” *Phys. Rev. Lett.* **99**, 213 901 (2007).
- [14] N. Dudovich, D. Oron, and Y. Silberberg, “Single-pulse coherently controlled non-linear Raman spectroscopy and microscopy.” *Nature* **418**, 512–514 (2002).
- [15] T. Ideguchi, a. Poisson, G. Guelachvili, T. W. Hänsch, and N. Picqué, “Adaptive dual-comb spectroscopy in the green region.” *Opt. Lett.* **37**, 4847–9 (2012).
- [16] J. J. Chang, B. E. Warner, E. P. Dragon, and M. W. Martinez, “Precision micromachining with pulsed green lasers,” *J. Laser Appl.* **10**, 285 (1998).
- [17] K. Sugioka and Y. Cheng, “Ultrafast lasers-reliable tools for advanced materials processing,” *Light: Science & Applications* **3**, e149 (2014).
- [18] S. K. Chaitanya and M. Ebrahim-Zadeh, “Fiber-laser-based green-pumped picosecond MgO:sPPLT optical parametric oscillator.” *Opt. Lett.* **38**, 5349–52 (2013).
- [19] G. K. Samanta, S. C. Kumar, a. Aadhi, and M. Ebrahim-Zadeh, “Yb-fiber-laser-pumped, high-repetition-rate picosecond optical parametric oscillator tunable in the ultraviolet.” *Opt. Express* **22**, 11 476–87 (2014).
- [20] M. Ebrahimzadeh, “Mid-infrared ultrafast and continuous-wave optical parametric oscillators,” in *Solid-state mid-infrared laser sources* (Springer, 2003), pp. 184–224.

- [21] M. Ebrahim-Zadeh and S. Chaitanya Kumar, "Yb-Fiber-Laser-Pumped Ultrafast Frequency Conversion Sources From the Mid-Infrared to the Ultraviolet," *IEEE J. Sel. Top. Quantum Electron.* **20**, 624–642 (2014).
- [22] S. K. Chaitanya and M. Ebrahim-Zadeh, "High-power, fiber-pumped, picosecond green source based on BiB_3O_6 ," *Laser Phys.* **24**, 025 401 (2014).
- [23] G. K. Samanta, S. C. Kumar, M. Mathew, C. Canalias, V. Pasiskevicius, F. Laurell, and M. Ebrahim-Zadeh, "High-power, continuous-wave, second-harmonic generation at 532 nm in periodically poled KTiOPO_4 ," *Opt. Lett.* **33**, 2955–2957 (2008).
- [24] M. Ebrahim-Zadeh, "Efficient Ultrafast Frequency Conversion Sources for the Visible and Ultraviolet Based on BiB_3O_6 ," *IEEE J. Sel. Top. Quantum Electron.* **13**, 679–691 (2007).
- [25] G. K. Samanta and M. Kumar, S Chaitanya, Ebrahim-Zadeh, "Stable, 9.6 W, continuous-wave, single-frequency, fiber-based green source at 532 nm," *Opt. Lett.* **34**, 1561–1563 (2009).
- [26] G. K. Samanta, S. C. Kumar, K. Devi, and M. Ebrahim-Zadeh, "Multicrystal, continuous-wave, single-pass second-harmonic generation with 56% efficiency." *Opt. Lett.* **35**, 3513–3515 (2010).
- [27] S. Kumar, J. Casals, J. Wei, and M. Ebrahim-Zadeh, "High-power, high-repetition-rate performance characteristics of $\beta\text{-BaB}_2\text{O}_4$ for single-pass picosecond ultraviolet generation at 266 nm," *Opt. Express* (2015).
- [28] N. Apurv Chaitanya, A. Aadhi, R. P. Singh, and G. K. Samanta, "Type-I frequency-doubling characteristics of high-power, ultrafast fiber laser in thick BIBO crystal." *Opt. Lett.* **39**, 5419–22 (2014).
- [29] A. M. Weiner, A. M. Kan'an, and D. E. Leaird, "High-efficiency blue generation by frequency doubling of femtosecond pulses in a thick nonlinear crystal." *Opt. Lett.* **23**, 1441–3 (1998).

- [30] S. K. Chaitanya, G. K. Samanta, K. Devi, and M. Ebrahim-Zadeh, “High-efficiency, multicrystal, single-pass, continuous-wave second harmonic generation.” *Opt. Express* **19**, 11 152–11 169 (2011).
- [31] M. Bauer, “Femtosecond ultraviolet photoelectron spectroscopy of ultra-fast surface processes,” *J. Phys. D. Appl. Phys.* **38**, R253–R267 (2005).
- [32] T. A. Klar and S. W. Hell, “Subdiffraction resolution in far-field fluorescence microscopy,” *Opt. Lett.* **24**, 954 (1999).
- [33] J. Yin, J.-G. Ren, H. Lu, Y. Cao, H.-L. Yong, Y.-P. Wu, C. Liu, S.-K. Liao, F. Zhou, Y. Jiang, X.-D. Cai, P. Xu, G.-S. Pan, J.-J. Jia, Y.-M. Huang, H. Yin, J.-Y. Wang, Y.-A. Chen, C.-Z. Peng, and J.-W. Pan, “Quantum teleportation and entanglement distribution over 100-kilometre free-space channels,” *Nature* **488**, 185–188 (2012).
- [34] Y. X. Fan, R. C. Eckardt, R. L. Byer, J. Nolting, and R. Wallenstein, “Visible BaB2O4 optical parametric oscillator pumped at 355 nm by a single-axial-mode pulsed source,” *Appl. Phys. Lett.* **53**, 2014 (1988).
- [35] X. Yan, Q. Liu, H. Chen, X. Fu, M. Gong, and D. Wang, “35.1 W all-solid-state 355 nm ultraviolet laser,” *Laser Phys. Lett.* **7**, 563–568 (2010).
- [36] J. Ringling, O. Kittelmann, F. Noack, G. Korn, and J. A. Squier, “Tunable femtosecond pulses in the near vacuum ultraviolet generated by frequency conversion of amplified Ti:sapphire laser pulses,” *Opt. Lett.* **18**, 2035 (1993).
- [37] I. Ricciardi, M. De Rosa, A. Rocco, P. Ferraro, A. Vannucci, P. Spano, and P. De Natale, “Sum-frequency generation of cw ultraviolet radiation in periodically poled LiTaO₃,” *Opt. Lett.* **34**, 1348 (2009).
- [38] C. Gu, M. Hu, J. Fan, Y. Song, B. Liu, L. Chai, C. Wang, and D. T. Reid, “High power tunable femtosecond ultraviolet laser source based on an Yb-fiber-laser pumped optical parametric oscillator.” *Opt. Express* **23**, 6181–6 (2015).
- [39] S. Zhu, “Quasi-Phase-Matched Third-Harmonic Generation in a Quasi-Periodic Optical Superlattice,” *Science* **278**, 843–846 (1997).

- [40] A. V. Smith, “How to use SNLO nonlinear optics software to select nonlinear crystals and model their performance,” *Proc. SPIE* **4972**, 50–57 (2003).
- [41] D. G. Grier, “A revolution in optical manipulation.” *Nature* **424**, 810–6 (2003).
- [42] C. Hnatovsky, V. G. Shvedov, W. Krolikowski, and A. V. Rode, “Materials processing with a tightly focused femtosecond laser vortex pulse.” *Opt. Lett.* **35**, 3417–9 (2010).
- [43] G. Gariepy, J. Leach, K. T. Kim, T. J. Hammond, E. Frumker, R. W. Boyd, and P. B. Corkum, “Creating high-harmonic beams with controlled orbital angular momentum.” *Phys. Rev. Lett.* **113**, 153 901 (2014).
- [44] A. Kumar, J. Banerji, and R. P. Singh, “Intensity correlation properties of high-order optical vortices passing through a rotating ground-glass plate.” *Opt. Lett.* **35**, 3841–3 (2010).
- [45] G. Ruffato, M. Massari, and F. Romanato, “Generation of high-order Laguerre-Gaussian modes by means of spiral phase plates.” *Opt. Lett.* **39**, 5094–7 (2014).
- [46] A. Aadhi, N. Apurv Chaitanya, R. P. Singh, and G. K. Samanta, “High-power, continuous-wave, solid-state, single-frequency, tunable source for the ultraviolet.” *Opt. Lett.* **39**, 3410–3 (2014).
- [47] P. Vaity, J. Banerji, and R. Singh, “Measuring the topological charge of an optical vortex by using a tilted convex lens,” *Phys. Lett. A* **377**, 1154–1156 (2013).
- [48] S.-M. Li, L.-J. Kong, Z.-C. Ren, Y. Li, C. Tu, and H.-T. Wang, “Managing orbital angular momentum in second-harmonic generation,” *Phys. Rev. A* **88**, 035 801 (2013).
- [49] T. Roger, J. J. F. Heitz, E. M. Wright, and D. Faccio, “Non-collinear interaction of photons with orbital angular momentum.” *Sci. Rep.* **3**, 3491 (2013).
- [50] J. E. Curtis and D. G. Grier, “Structure of optical vortices.” *Phys. Rev. Lett.* **90**, 133 901 (2003).

- [51] S. G. Reddy, S. Prabhakar, A. Kumar, J. Banerji, and R. P. Singh, “Higher order optical vortices and formation of speckles.” *Opt. Lett.* **39**, 4364–7 (2014).
- [52] M. van Veenendaal and I. McNulty, “Prediction of strong dichroism induced by x rays carrying orbital momentum.” *Phys. Rev. Lett.* **98**, 157 401 (2007).
- [53] A. Sakdinawat and Y. Liu, “Soft-x-ray microscopy using spiral zone plates,” *Opt. Lett.* **32**, 2635 (2007).
- [54] K. A. Nugent, “Coherent methods in the X-ray sciences,” *Adv. Phys.* **59**, 1–99 (2010).
- [55] G. Donnert, J. Keller, R. Medda, M. A. Andrei, S. O. Rizzoli, R. Luhrmann, R. Jahn, C. Eggeling, and S. W. Hell, “Macromolecular-scale resolution in biological fluorescence microscopy,” *Proc. Natl. Acad. Sci.* **103**, 11 440–11 445 (2006).
- [56] S. Prabhakar, S. Gangi Reddy, A. Aadhi, A. Kumar, P. Chithrabhanu, G. Samanta, and R. Singh, “Spatial distribution of spontaneous parametric down-converted photons for higher order optical vortices,” *Opt. Commun.* **326**, 64–69 (2014).
- [57] N. Apurv Chaitanya, A. Aadhi, M. V. Jabir, and G. K. Samanta, “Frequency-doubling characteristics of high-power, ultrafast vortex beams,” *Opt. Lett.* **40**, 2614 (2015).
- [58] V. Bazhenov, M. Soskin, and M. Vasnetsov, “Screw Dislocations in Light Wavefronts,” *J. Mod. Opt.* **39**, 985–990 (1992).
- [59] M. Beijersbergen, L. Allen, H. van der Veen, and J. Woerdman, “Astigmatic laser mode converters and transfer of orbital angular momentum,” *Opt. Commun.* **96**, 123–132 (1993).
- [60] S. G. Reddy, C. Permangatt, S. Prabhakar, A. Anwar, J. Banerji, and R. P. Singh, “Divergence of optical vortex beams,” *Appl. Opt.* **54**, 6690 (2015).
- [61] A. Abulikemu, T. Yusufu, R. Mamuti, K. Miyamoto, and T. Omatsu, “Widely-tunable vortex output from a singly resonant optical parametric oscillator,” *Opt. Express* **23**, 18 338 (2015).

- [62] T. Yusufu, Y. Tokizane, M. Yamada, K. Miyamoto, and T. Omatsu, “Tunable 2- μm optical vortex parametric oscillator,” *Opt. Express* **20**, 23 666 (2012).
- [63] P. Vaity and L. Rusch, “Perfect vortex beam: Fourier transformation of a Bessel beam,” *Opt. Lett.* **40**, 597 (2015).
- [64] T. Volk and M. Wöhlecke, *Lithium Niobate: Defects, Photorefraction and Ferroelectric Switching* (Springer Science & Business Media, 2008).
- [65] S. Pleasants, “Beam shaping: Hollow Gaussian beams,” *Nat. Photonics* **8**, 423–423 (2014).
- [66] Z. Wang, Q. Lin, and Y. Wang, “Control of atomic rotation by elliptical hollow beam carrying zero angular momentum,” *Opt. Commun.* **240**, 357–362 (2004).
- [67] T. Kuga, Y. Torii, N. Shiokawa, T. Hirano, Y. Shimizu, and H. Sasada, “Novel optical trap of atoms with a doughnut beam,” *Phys. Rev. Lett.* **78**, 4713 (1997).
- [68] H. Ito, K. Sakaki, W. Jhe, and M. Ohtsu, “Atomic funnel with evanescent light,” *Phys. Rev. A* **56**, 712 (1997).
- [69] J. Yin, Y. Zhu, W. Jhe, and Z. Wang, “Atom guiding and cooling in a dark hollow laser beam,” *Phys. Rev. A* **58**, 509 (1998).
- [70] C.-L. Zhao, L.-G. Wang, and X.-H. Lu, “Radiation forces on a dielectric sphere produced by highly focused hollow Gaussian beams,” *Phys. Lett. A* **363**, 502–506 (2007).
- [71] Y. Cai, H. T. Eyyuboğlu, and Y. Baykal, “Scintillation of astigmatic dark hollow beams in weak atmospheric turbulence,” *J. Opt. Soc A* **25**, 1497–1503 (2008).
- [72] L. C. Andrews, R. L. Phillips, and C. Y. Hopen, *Laser beam scintillation with applications*, Vol. 99 (SPIE press, 2001).
- [73] Z. Feng, W. Li, C. Yu, X. Liu, J. Liu, and L. Fu, “Extended laser filamentation in air generated by femtosecond annular Gaussian beams,” *Phys. Rev. A* **91**, 033 839 (2015).

- [74] G. Purohit, P. Rawat, and R. Gauniyal, “Second harmonic generation by self-focusing of intense hollow Gaussian laser beam in collisionless plasma,” *Phys. Plasmas* **23**, 013 103 (2016).
- [75] A. Sharma, S. Misra, S. Mishra, and I. Kourakis, “Dynamics of dark hollow Gaussian laser pulses in relativistic plasma,” *Phys. Rev. E* **87**, 063 111 (2013).
- [76] Z. Liu, H. Zhao, J. Liu, J. Lin, M. A. Ahmad, and S. Liu, “Generation of hollow Gaussian beams by spatial filtering,” *Opt. Lett.* **32**, 2076–2078 (2007).
- [77] I. Manek, Y. B. Ovchinnikov, and R. Grimm, “Generation of a hollow laser beam for atom trapping using an axicon,” *Opt. Commun.* **147**, 67–70 (1998).
- [78] C. Zhao, Y. Cai, F. Wang, X. Lu, and Y. Wang, “Generation of a high-quality partially coherent dark hollow beam with a multimode fiber,” *Opt. Lett.* **33**, 1389–1391 (2008).
- [79] Y. Nie, H. Ma, X. Li, W. Hu, and J. Yang, “Generation of dark hollow femtosecond pulsed beam by phase-only liquid crystal spatial light modulator,” *Appl. Opt.* **50**, 4174–4179 (2011).
- [80] C. Wei, X. Lu, G. Wu, F. Wang, and Y. Cai, “A new method for generating a hollow Gaussian beam,” *Appl. Phys. B* **115**, 55–60 (2014).
- [81] J. Sun, J. Zeng, X. Wang, A. N. Cartwright, and N. M. Litchinitser, “Concealing with structured light,” *Sci. Rep.* **4** (2014).
- [82] J. Arlt and K. Dholakia, “Generation of high-order Bessel beams by use of an axicon,” *Opt. Commun.* **177**, 297–301 (2000).
- [83] J. C. Gutiérrez-Vega, M. Iturbe-Castillo, and S. Chávez-Cerda, “Alternative formulation for invariant optical fields: Mathieu beams,” *Opt. Lett.* **25**, 1493–1495 (2000).
- [84] Y. Cai and S. He, “Propagation of hollow Gaussian beams through apertured paraxial optical systems,” *J. Opt. Soc A* **23**, 1410–1418 (2006).

- [85] A. A. Alkelly, H. Al-Nadary, and I. A. Alhijry, “The intensity distribution of hollow Gaussian beams focused by a lens with spherical aberration,” *Opt. Commun.* **284**, 322–329 (2011).
- [86] N. Apurv Chaitanya, A. Aadhi, M. V. Jabir, and G. K. Samanta, “High-power, high-repetition-rate, Yb-fiber laser based femtosecond source at 355 nm,” *Opt. Lett.* **40**, 4269–4272 (2015).
- [87] D. Caetano, M. Almeida, P. S. Ribeiro, J. Huguenin, B. C. dos Santos, and A. Houry, “Conservation of orbital angular momentum in stimulated down-conversion,” *Phys. Rev. A* **66**, 041 801 (2002).
- [88] J. Leach, M. J. Padgett, S. M. Barnett, S. Franke-Arnold, and J. Courtial, “Measuring the orbital angular momentum of a single photon,” *Phys. Rev. Lett.* **88**, 257 901 (2002).
- [89] M. V. Berry, “Nonspreading wave packets,” *Am. J. Phys.* **47**, 264 (1979).
- [90] G. A. Siviloglou and D. N. Christodoulides, “Accelerating finite energy Airy beams,” *Opt. Lett.* **32**, 979–981 (2007).
- [91] P. Rose, F. Diebel, M. Boguslawski, and C. Denz, “Airy beam induced optical routing,” *Appl. Phys. Lett.* **102** (2013).
- [92] J. Baumgartl, M. Mazilu, and K. Dholakia, “Optically mediated particle clearing using Airy wavepackets,” *Nat. Photonics* **2**, 675–678 (2008).
- [93] P. Zhang, J. Prakash, Z. Zhang, M. S. Mills, N. K. Efremidis, D. N. Christodoulides, and Z. Chen, “Trapping and guiding microparticles with morphing autofocusing Airy beams,” *Opt. Lett.* **36**, 2883–2885 (2011).
- [94] T. Vettenburg, H. I. C. Dalgarno, J. Nylk, C. Coll-Lladó, D. E. K. Ferrier, F. J. Gunn-Moore, and K. Dholakia, “Light-sheet microscopy using an Airy beam,” *Nat. Methods* **11**, 541–4 (2014).

- [95] A. Mathis, F. Courvoisier, L. Froehly, L. Furfaro, M. Jacquot, P. A. Lacourt, and J. M. Dudley, “Micromachining along a curve: Femtosecond laser micromachining of curved profiles in diamond and silicon using accelerating beams,” *Appl. Phys. Lett.* **101** (2012).
- [96] S. Jia, J. Lee, J. W. Fleischer, G. A. Siviloglou, and D. N. Christodoulides, “Diffusion-trapped airy beams in photorefractive media,” *Phys. Rev. Lett.* **104** (2010).
- [97] R. P. Chen, C. F. Yin, X. X. Chu, and H. Wang, “Effect of Kerr nonlinearity on an Airy beam,” *Phys. Rev. A* **82** (2010).
- [98] P. Polynkin, M. Kolesik, J. V. Moloney, G. A. Siviloglou, and D. N. Christodoulides, “Curved Plasma Channel Generation Using Ultraintense Airy Beams,” *Science* **324**, 229–232 (2009).
- [99] P. Polynkin, M. Kolesik, and J. Moloney, “Filamentation of Femtosecond Laser Airy Beams in Water,” *Phys. Rev. Lett.* **103** (2009).
- [100] A. Lotti, D. Faccio, A. Couairon, D. G. Papazoglou, P. Panagiotopoulos, D. Abdollahpour, and S. Tzortzakis, “Stationary nonlinear Airy beams,” *Phys. Rev. A* **84** (2011).
- [101] I. Kaminer, M. Segev, and D. N. Christodoulides, “Self-accelerating self-trapped optical beams,” *Phys. Rev. Lett.* **106** (2011).
- [102] P. Panagiotopoulos, D. Abdollahpour, A. Lotti, A. Couairon, D. Faccio, D. G. Papazoglou, and S. Tzortzakis, “Nonlinear propagation dynamics of finite-energy Airy beams,” *Phys. Rev. A* **86** (2012).
- [103] X. Chu, “Evolution of an Airy beam in turbulence.” *Opt. Lett.* **36**, 2701–3 (2011).
- [104] N. Voloch-Bloch, Y. Lereah, Y. Lilach, A. Gover, and A. Arie, “Generation of electron Airy beams.” *Nature* **494**, 331–335 (2013).

- [105] P. Zhang, T. Li, J. Zhu, X. Zhu, S. Yang, Y. Wang, X. Yin, and X. Zhang, “Generation of acoustic self-bending and bottle beams by phase engineering.” *Nat. Commun.* **5**, 4316 (2014).
- [106] A. Salandrino and D. N. Christodoulides, “Airy plasmon: a nondiffracting surface wave.” *Opt. Lett.* **35**, 2082–2084 (2010).
- [107] Aadhi, N. Apurv Chaitanya, M. V. Jabir, Vairy, R. P. Singh, and G. K. Samanta, “Airy beam optical parametric oscillator.” *Sci. Rep.* (2016).
- [108] M. Ebrahim-Zadeh, S. C. Kumar, A. Esteban-Martin, and G. K. Samanta, “Breakthroughs in photonics 2012: Breakthroughs in optical parametric oscillators,” *IEEE Photonics J.* **5** (2013).